Summer 2016

Emergence of Collective Light Scattering in Atomic 87Rb Samples

Kasie Jean Kemp
Old Dominion University

EMERGENCE OF COLLECTIVE LIGHT SCATTERING IN ATOMIC ^{87}RB SAMPLES

by

Kasie Jean Kemp
B.S. May 2010, Bridgewater College
M.S. May 2012, Old Dominion University

A Dissertation Submitted to the Faculty of
Old Dominion University in Partial Fulfillment of the
Requirements for the Degree of

DOCTOR OF PHILOSOPHY

PHYSICS

OLD DOMINION UNIVERSITY
August 2016

Approved by:

Mark D. Havey (Director)

Jozef Dudek (Member)

Sebastian Kuhn (Member)

Steven Pascal (Member)

Toza Popovic (Member)

ABSTRACT

EMERGENCE OF COLLECTIVE LIGHT SCATTERING IN ATOMIC ^{87}RB SAMPLES

Kasie Jean Kemp
Old Dominion University, 2016
Director: Dr. Mark D. Havey

Over the past half century, atomic ensembles have been used to create sensors, clocks, and quantum information systems. As these devices become more compact, and as the number of atoms increases to improve the sensitivity for detection, the atomic samples are increasing in density and optical depth. As such, the spectroscopic properties of the atomic media are modified due to interactions among the particles in the ensemble. We report investigation of near-resonance light scattering from a cold atomic sample of ^{87}Rb. Initially prepared in a magneto-optical trap, the atoms are loaded into a far-off-resonance optical dipole trap (FORT) in which the ensemble has a temperature near 100 μK and initial Gaussian radii of $\sim$3 μm and $\sim$280 μm in the transverse and longitudinal directions, respectively. With atomic densities in the range of 10^{10} - 10^{13} atoms/cm^3, measurements are made on the $F = 2 \rightarrow F' = 3$ nearly closed hyperfine transition. The experimental geometry consists of projecting a near-resonance collimated laser beam onto the entire volume of the FORT and detecting the diffusely scattered light. The measured scattered light intensity as a function of detuning, atomic number, and sample size suggests that collective light scattering depends on the optical depth of the system.

This thesis is dedicated to my family.

ACKNOWLEDGEMENTS

This has been one of the longest journeys in my life so far, and it would not have been possible without a multitude of people. Obviously, I thank Dr. Mark Havey for advising me through this arduous process. My lab mate, Stetson Roof, has struggled through sleepless data runs, troubleshooted broken equipment that has obviously been taken over by evil lab elves, and has been an altogether invaluable friend. I have garnered a great deal of support from the faculty and staff at ODU. I appreciate Dr. Sukenik for performing as a step-advisor and department chair, helping in every way possible. I want to thank Drs. Gail Dodge and Lepsha Vuskovic for opening their homes for dinners, as well as mentoring and supporting the women in the physics department. The support staff (Annette Guzman-Smith, Delicia Malin, Lisa Okun, and Justin Mason) have gone above and beyond and I appreciate their efforts.

My family has been amazingly supportive during this process. Thank you, Mom and Frankie, for being my biggest fans and never doubting me. I want to thank everyone in my very large and extended family for standing behind me and supporting me. Most importantly of all, I would like to thank my wife, Marie. I am grateful that you have stuck with me through a tumultuous 6 years of graduate school. I cannot imagine going through this without you. I look forward to many more years to come full of excitement and love without graduate school in the way. Thank you to my in-laws as well for the care and support. I have a great network of friends and family who deserve to be acknowledged here, but the rest will have to be thanked in person.

OPTICAL ELEMENT KEY

Most of the optical elements depicted in this thesis are shown below.

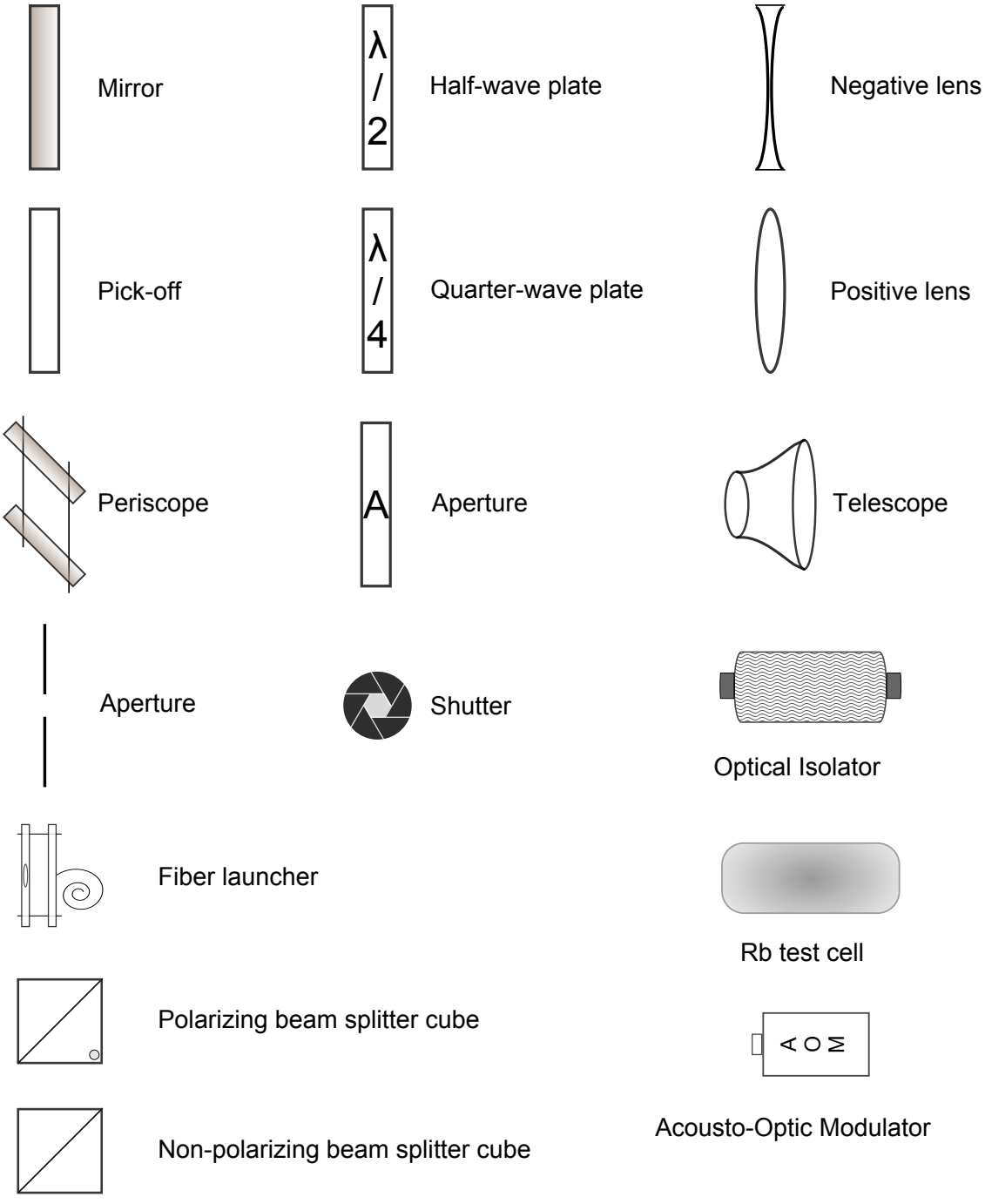

TABLE OF CONTENTS

Page

LIST OF TABLES

LIST OF FIGURES

CHAPTER 1

INTRODUCTION

In the past century, developments in experimental and theoretical physics have contributed to the progression of modern technology. Among other advancements, the study of the interactions between light and matter has led to the development of atomic clocks [1–3] and sensors, such as magnetometers and gyroscopes [4–8]. These developments have led to the proposal of creating a gravitational wave detector using an optical lattice atomic clock [9, 10]. Additionally, with the advent of quantum information and computing, atoms are also being used as storage devices and logic gates [11, 12]. Whether the atoms are in hot vapor cells [13], or confined to a cold atomic sample - perhaps trapped on a chip [14] or contained in an optical fiber [15] - spectroscopy of the various ensembles is utilized to obtain precise and stable measurements.

The study of light-matter interactions can scale from a single photon with a single atom [16], up to higher intensities or increasingly larger samples [17–21]. The light scattering properties for a single atom include a resonant frequency, cross section, excited state lifetime, and the associated resonance width. In general, increasing the number of atoms N will not modify these properties; the measured fluorescence will increase by a factor of N, and the scattering rates will remain constant. For low density, optically thin samples, the light scattering process for below-saturation intensities can be described as the sum of the ensembles' constituent scatterers.

Within an atomic sample, aggregate matter can behave differently than the sum of its individual components. For atomic samples with higher optical depth and density, and with a correspondingly lower average interatomic spacing r, the ensemble scatters light collectively as a bulk medium. The scattering rate and resonance widths are no longer constant, but depend on the macroscopic properties of the sample. Additionally, the spatial distribution of the atoms can lead to resonant energy shifts in absorption and emission of light [22–24].

Collective scattering, in which the total scattering can be described similar to that of a macroscopic object rather than the sum of individual microscopic objects, occurs over a broad range of conditions. Here it is important to distinguish between the two scattering regimes. For this thesis, we have defined collective scattering as the process in which the scattered field depends on the properties of the sample, rather than that of its individual

constituents. Cooperative scattering is a coherent process in which the atoms interact to modify their scattering properties [25]. This can happen when atoms are close enough together to interact, such as in the dipole-dipole interaction [26]. If the excitation of the sample is coherent and created in such a way that all of the atoms are in phase together, then cooperative scattering may take place as in the case of timed Dicke states [19, 27–29]. Additionally, the Collective Lamb Shift [23, 30–33] is a cooperative process in which virtual photons are exchanged, leading to a shift in the resonant energy levels. Superradiance and subradiance, in which the atoms decay cooperatively at a rate faster or slower than the natural lifetime, may also occur. These mechanisms are strongly dependent upon the macroscopic properties of the sample. Recent work has observed the effects of sample size, shape, density, and optical depth [18, 21, 24, 26, 34–46] on the spectroscopic properties of the medium.

One example of the experimental observation of the N dependence of collective scattering is the suppression of light scattering from ^{87}Rb atoms within a sample with dimensions near the wavelength of excitation [26]. The atoms act cooperatively to scatter when they interact through the dipole-dipole potential, which depends on the interatomic separation r between two dipoles and their respective polarizations. As r reduces and approaches the wavelength of the associated transition, the collective radiative decay rate of the excited state can be increased. This leads to an associated resonance broadening. Both the resonant width of the transition and the intensity of the scattered light show a scaling with the number of atoms N in the sample. Additionally, a shift in the resonant frequency occurs that scales linearly with N.

Another example of collective scattering has shown a dependence on the optical depth b of a sample. In a spherical magneto optical trap (MOT), it has been found that the spontaneous decay rate is modified by b. As the cold atomic sample expands, the optical depth increases due to the increase in the radius of the sample, and collective modes of the sample lead to atoms that can decay from a subradiant state (stay excited for longer periods of time) [19] or superradiant state (decay faster than the natural decay rate) [47]. Likewise, in a forward transmission experiment using ^{88}Sr, the detuning needed for maximum transmission of light scales linearly with b.

The emergence of new phenomena when transitioning from microscopic to bulk media has been of general interest to the scientific community for decades [48]. The introduction of more constituents in an ensemble can induce overall properties that can not be reduced to the sum of the individuals'; the mechanisms behind the emergent properties derive from

the global dynamics of the system. From the formation of columnar joints at the Giant's Causeway [49], to superconductivity [50], the emergence of new and interesting phenomena can be seen on a multitude of scales.

The goal of this thesis is to study the effects of sample properties on the transition from microscopic to macroscopic scattering. Through this transition, the emergence of the effects of multiple scattering are observed. We create samples with a wide range of properties in order to cover the large phase space associated with collective scattering. The effects of the number of atoms, sample geometry, and detuning of the optical excitation from a resonant transition will be shown. On resonance, the emergence of collective scattering depends on both the number of atoms and their distribution in space; the sample behaves as a macroscopic object that can be described by the optical depth of the system. By having control of the number of atoms and the physical size of the sample, we are able to dynamically observe the effects of density and optical depth. While much of the experimental setup is similar to [26], the number of atoms is much higher and the samples are physically larger. Thus the interatomic separation is greater and we are not quite in the dipole-dipole scattering regime.

Because we will be studying the emergence of collective light scattering, it is important to first understand scattering from a single atom. Thus, this thesis will begin with a description of a two level atom, and the near-resonance scattering cross section, resonance width, and lifetime of the excited state are derived. Diffusion of light through an ensemble of atoms is described, and a random walk model is developed to depict this scattering process.

Following the introduction to light scattering, the methods for creating and characterizing the atomic samples are outlined. Lasers are utilized to cool and trap atomic ^{87}Rb first in a magneto optical trap (MOT), and then transferred into a far off resonance optical dipole trap (FORT). The MOT and FORT are characterized with numerous methods to accurately measure the number of atoms, temperature, and spatial size of each sample.

Finally, the experimental setup and methods are described. A low intensity probe laser beam, much larger than the size of the sample, excites atoms near the nearly closed $5s^2S_{1/2}, F = 2 \rightarrow 5s^2P_{3/2}, F' = 3$ transition. The scattered light is collected off-axis from the initial excitation direction. The sample properties are modified to study the dependence of on-resonant scattering on the number of atoms and the spatial size of the sample. Additionally, the probe laser is tuned about resonance to observe near-resonance scattering for an expanding sample. The results of the experiments are shown and compared with the results of the random walk model.

CHAPTER 2

LIGHT SCATTERING INTRODUCTION

In this chapter, numerous methods are explored to derive spectroscopic properties of a single atom. While these approaches will be simplified to that of an atom with two levels (a ground state $|0\rangle$ and a sole excited state $|1\rangle$,) they are also applicable to systems in which there are multiple excited states. While there is an abundance of literature available on the two level atom, including probably nearly every thesis in cold atomic physics, a selection of the various approaches will also be described below. Loudon's *The Quantum Theory of Light* [51] and Metcalf's *Laser Cooling and Trapping* [52] are both helpful resources for further information.

2.1 SCHRÖDINGER'S EQUATION

Consider an atom described by a set of orthonormal basis states denoted by $|n\rangle$, $\langle m|n\rangle = \delta_{mn}$. Applying the Hamiltonian H_0 to the state $|n\rangle$, we can find the associated energy $E_n = \hbar\,\omega_n$:

$$H_0|n\rangle = E_n|n\rangle. \tag{1}$$

Introducing a small time dependent potential $V(t)$ to the atom can cause a change in the state of the system. Substituting the total Hamiltonian $H = H_0 + V(t)$ into Schrödinger's equation yields

$$\left(H_0 + V(t)\right)|\Psi\rangle = i\hbar\frac{\partial}{\partial t}|\Psi\rangle \tag{2}$$

with solutions of the form

$$|\Psi\rangle = \sum_{k=0}^{\infty} a_k(t)e^{-i\omega_k t}|k\rangle. \tag{3}$$

Substitution of Eq. 3 into Eq. 2 gives

$$\left(H_0 + V(t)\right)|\Psi\rangle = i\hbar\sum_{k=0}^{\infty}\left(\dot{a}_k(t)e^{-i\omega_k t} - i\omega_k a_k(t)e^{-i\omega_k t}\right)|k\rangle. \tag{4}$$

Multiplying by $\langle n|$ and applying orthonormality reveals that the rate of change of the probability amplitude for a state is

$$\dot{a}_n(t) = \frac{1}{i\hbar}\sum_{k=0}^{\infty} a_k(t)e^{-i(\omega_k-\omega_n)t}\langle n|V(t)|k\rangle. \tag{5}$$

For experiments with narrow-band lasers tuned close to a resonance and energy levels that are well separated in frequency space, the atoms can be described to first order as having only two levels: the ground state $|0\rangle$ and excited state $|1\rangle$ with a frequency difference $\omega_{10} = \omega_1 - \omega_0$. Using a two-level atom model, Eq. 5 reduces to a system of two equations [51].

$$\dot{a}_0(t) = \frac{1}{i\hbar}a_1(t)e^{-i\omega_{10}t}\langle 0|V(t)|1\rangle \tag{6}$$

$$\dot{a}_1(t) = \frac{1}{i\hbar}a_0(t)e^{i\omega_{10}t}\langle 1|V(t)|0\rangle. \tag{7}$$

Note that only the off-diagonal terms remain, as the potential to drive electric dipole transitions

$$V = -q\overrightarrow{E}\cdot\overrightarrow{r} \tag{8}$$

is spatially odd. Here $q = -e$ is the charge of an electron and $\overrightarrow{r}$ describes the atom's electron coordinates. The applied electric field $\overrightarrow{E}$ is oscillating in time with a frequency ω and has a given polarization $\hat{\epsilon}$:

$$\overrightarrow{E} = E_0\cos(\omega t)\,\hat{\epsilon}, \tag{9}$$

$$V = eE_0\cos(\omega t)\,\hat{\epsilon}\cdot\overrightarrow{r}. \tag{10}$$

For an atom initially in the ground state that is weakly excited with the potential described by Eq. 10, ground and excited state coefficients have the following conditions: $a_0(0) = 1, a_1(t) \approx 0, a_0(t) \approx 1$. Substituting Eq. 10 into Eq. 7 and integrating over time from 0 to t yields

$$a_1(t) = \frac{1}{2i\hbar}\langle 1|eE_0\hat{\epsilon}\cdot\overrightarrow{r}|0\rangle\left(\frac{e^{i(\omega+\omega_{10})t}-1}{i(\omega+\omega_{10})} + \frac{e^{-i(\omega-\omega_{10})t}-1}{-i(\omega-\omega_{10})}\right) \tag{11}$$

Because the excitation frequency ω is near the bare resonance ω_{10}, the rotating wave approximation (RWA) is applied. This removes the high frequency components $\omega + \omega_{10}$ from the solution, while the terms with the detuning from resonance $\delta = \omega - \omega_{10}$ remain. Applying

the RWA simplifies the probability amplitude $a_1(t)$ to

$$a_1(t) = \frac{1}{2i\hbar}\langle 1|eE_0\hat{\epsilon}\cdot\overrightarrow{r}|0\rangle e^{-i\delta t/2}\sin(\delta t/2)\frac{1}{\delta} \tag{12}$$

and the probability of an atom to be in the excited state as a function of time $P_1(t) = |a_1(t)|^2$ is

$$P_1(t) = |\Omega_{10}|^2\frac{\sin^2(\delta t/2)}{\delta^2}. \tag{13}$$

Here we have introduced the Rabi frequency [51]

$$\Omega_{nm} = \frac{1}{\hbar}\langle m|eE_0\hat{\epsilon}\cdot\overrightarrow{r}|n\rangle \tag{14}$$

which signifies how well the driving field couples with the atom and depends on the intensity of the field, as well as the orientation of the polarization with the atom. While Eq. 13 predicts that the atom will oscillate in time between the ground and excited state, this is an incomplete model, as it does not allow for the spontaneous emission of a photon. This is a form of loss and does not appear within the framework of the Schrödinger equation. To more fully describe the system, other approaches must be taken.

2.2 RATE EQUATIONS

Rate equations are a valuable tool in predicting energy level populations within an ensemble. Using a phenomenological approach, the decay rates from each state to another can be used to create coupled rate equations [53]. These equations can be solved to describe the time evolution of the system. We begin by treating N two-level atoms with N_0 atoms in the ground state $|0\rangle$ with a degeneracy of g_0 and N_1 atoms in the sole exited state $|1\rangle$ with a degeneracy of g_1. The energy difference between the two discrete levels is

$$\hbar\omega_{10} = E_1 - E_0. \tag{15}$$

It is assumed that an atom can exist only in these two states, so $N_0 + N_1 = N$. An atom that is initially in the ground state can be driven to the excited state with an absorption probability rate of $B_{01}\overline{W}$, where $\overline{W}$ is the energy density of the excitation source with a bandwidth of δw. In the case of excitation by a narrowband laser with intensity I, this energy density is $\overline{W} = I/c$, where c is the speed of light. Once an atom is in the excited state $|1\rangle$, there are two mechanisms which will allow for the atom to return to the ground

state. Stimulated emission of a photon occurs at a rate $B_{10}\overline{W}$, and spontanous emission of a photon occurs at a rate γ. Note that the notation used here is for consistency throughout the various methods. Historically, B_{01} and B_{10} are known respectively as Einstein's B coefficients B_{12} and B_{21} for transitions involving a ground state $|1\rangle$ and excited state $|2\rangle$. Additionally, γ is known as Einstein's A coefficient A_{21}. The lifetime of the excited state

$$\tau = 1/\gamma \tag{16}$$

is the average time it takes for an atom in the excited state to spontaneously decay to the ground state.

The rate of change of the number of atoms in $|1\rangle$ is

$$\dot{N}_1(t) = -\gamma N_1 + B_{01}\overline{W}N_0 - B_{10}\overline{W}N_1 \tag{17}$$

and for the ground state

$$\dot{N}_0(t) = -\dot{N}_1(t). \tag{18}$$

In the steady state regime, the occupation of each level is constant. Setting Eq. 17 equal to 0, the excited state population is

$$\frac{N_1}{N} = \frac{B_{01}\overline{W}}{\gamma + B_{10}\overline{W} + B_{01}\overline{W}}. \tag{19}$$

This excited state probability can be compared to that found in Eq. 13 with the relation $\overline{P_1} = B_{01}\langle\overline{W}\rangle t$ to find the decay rate γ of the excited state. The average probability over time to be in the excited state is

$$\overline{P_1} = \overline{|\langle 1|\hat{\epsilon}\cdot\overrightarrow{r}|0\rangle|^2}\frac{q^2\pi\overline{W}}{\epsilon_0\hbar^2}t. \tag{20}$$

Taking the ensemble average over all angles between the orientations of the atoms and polarization of light,

$$\overline{|\langle 1|\hat{\epsilon}\cdot\overrightarrow{r}|0\rangle|^2} = \overline{\cos^2\theta}|\langle 1|r|0\rangle|^2 = \frac{1}{3}|\langle 1|r|0\rangle|^2. \tag{21}$$

Using the relations between the Einstein coefficients

$$g_0 B_{01} = g_1 B_{10}, \gamma = \frac{\hbar\omega_{10}^3}{\pi^2 c^3}B_{10} \tag{22}$$

and comparison of Eqs. 19 and 20, we find that the decay rate for a two-level degenerate atom is

$$\gamma = \frac{1}{3}\frac{g_0}{g_1}\frac{q^2}{\pi\epsilon_0\hbar}\frac{\omega_{10}^3}{c^3}|\langle 1|r|0\rangle|^2. \tag{23}$$

2.3 OPTICAL BLOCH EQUATIONS

While the rate equation method is able to describe state probabilities for an atomic ensemble, it does not allow for coherence effects and does not provide state amplitudes. In this section, we will use a density matrix approach to describe the atomic state amplitudes. The time-dependent Schrödinger equation using this formalism is

$$i\hbar\dot{\rho} = [H, \rho] \tag{24}$$

with the density matrix ρ for a two level atom in a pure state given by

$$\rho = \begin{pmatrix} \rho_{11} & \rho_{10} \\ \rho_{01} & \rho_{00} \end{pmatrix} = \begin{pmatrix} a_1 a_1^* & a_1 a_0^* \\ a_0 a_1^* & a_0 a_0^* \end{pmatrix}. \tag{25}$$

In general, the rate of change of the density matrix elements is

$$\dot{\rho}_{ij} = \dot{a}_i a_j^* + a_i \dot{a}_j^*, \tag{26}$$

with the time derivatives of the coefficients being the same as those in Eqs. 6 and 7. However, the rate of change must include spontaneous emission, so Eq. 26 must be modified [51]:

$$i\hbar\dot{\rho} = [H, \rho] - \dot{\rho}_{sp}, \tag{27}$$

where the relaxation matrix is given by

$$\dot{\rho}_{sp} = \gamma \begin{pmatrix} -\rho_{11} & \frac{1}{2}\rho_{10} \\ \frac{1}{2}\rho_{10} & \rho_{11} \end{pmatrix}. \tag{28}$$

Using these equations and the notation $\tilde{\rho}_{01} = \rho_{01}e^{-i\delta t}$, $\tilde{\rho}_{10} = \rho_{10}e^{i\delta t}$, $\delta = \omega - \omega_{10}$, the Optical Bloch Equations in the RWA are

$$\dot{\rho}_{00} = \gamma\rho_{11} + \frac{i}{2}\left(\Omega^*\tilde{\rho}_{10} - \Omega\tilde{\rho}_{01}\right) \tag{29}$$

$$\dot{\rho}_{11} = -\gamma\rho_{11} + \frac{i}{2}\left(\Omega\tilde{\rho}_{01} - \Omega^*\tilde{\rho}_{10}\right) \tag{30}$$

$$\dot{\tilde{\rho}}_{01} = -\left(\frac{\gamma}{2} + i\delta\right)\tilde{\rho}_{01} + \frac{i}{2}\Omega^*\left(\rho_{11} - \rho_{00}\right) \tag{31}$$

$$\dot{\tilde{\rho}}_{10} = -\left(\frac{\gamma}{2} - i\delta\right)\tilde{\rho}_{10} + \frac{i}{2}\Omega\left(\rho_{00} - \rho_{11}\right) \tag{32}$$

The Rabi frequency Ω is the same as that given in Eq. 15.

We are interested in what happens in the steady state regime, when the derivatives are all set equal to 0. Using the conservation of probability ($\rho_{00} + \rho_{11} = 1$) and the fact that $\rho_{10} = \rho_{01}^*$, we find that

$$\rho_{10} = \frac{i\Omega}{2(\gamma/2 - i\delta)(1+s)} \tag{33}$$

for the saturation parameter s given by

$$s = \frac{s_0}{1 + \left(\frac{2\delta}{\gamma}\right)^2} \tag{34}$$

with the on-resonance saturation parameter $s_0 = 2|\Omega|^2/\gamma^2$. For low saturation saturation parameters ($s << 1$), the excited state probability is found to be

$$\rho_{11} = \frac{s_0/2}{1 + s_0 + \left(\frac{2\delta}{\gamma}\right)^2}. \tag{35}$$

2.4 ELECTRIC FIELD PROPAGATION

So far, we have only been concerned with the dynamics associated with the state of the atom or atoms within an ensemble. However, much can be learned from the excitation field itself. We begin with an electromagnetic plane wave of frequency ω and complex polarization $\hat{\epsilon}$ propagating through a dielectric medium [54]. The electric field with amplitude E_0 is defined by

$$\overrightarrow{E} = E_0 e^{-i(\omega t - \overrightarrow{k}\cdot\overrightarrow{r})}\hat{\epsilon}. \tag{36}$$

The wave vector $\overrightarrow{k} = k\hat{k}$ travels in the direction of propagation $\hat{k}$ with a magnitude $k = \frac{\omega}{c}n$, where n is the complex index of refraction for the dielectric medium. Using

$$n = n_r + in_i, \tag{37}$$

Eq. 36 becomes

$$\overrightarrow{E} = E_0 e^{-i(\omega t - \frac{\omega n_r}{c}\hat{k}\cdot\overrightarrow{r})} e^{-\frac{\omega n_i}{c}\hat{k}\cdot\overrightarrow{r}}\hat{\epsilon}. \tag{38}$$

There are two components of the electric field. The real part of the index of refraction appears in the phase, while the intensity through the medium is determined by the imaginary part of the index of refraction. This becomes more apparent if we calculate the intensity of the electric field, which is equivalent to the time-averaged Poynting vector $\langle S \rangle$. Given that

$$\overrightarrow{S} = \frac{1}{\mu_0}\overrightarrow{E} \times \overrightarrow{B} \tag{39}$$

and

$$\overrightarrow{B} = \frac{1}{c}\hat{k} \times \overrightarrow{E}, \tag{40}$$

averaging over time yields that the intensity $I(z)$ of the field propagating in the z direction is

$$I(z) = \frac{E_0^2}{2\mu_0 c} e^{-\frac{2\omega n_i}{c}z}. \tag{41}$$

As the wave propagates through the medium, its intensity is attenuated exponentially with distance. The attenuation coefficient for the medium is given as

$$\kappa = \frac{2\omega}{c} n_i \tag{42}$$

and the peak intensity $I_0 = \frac{E_0^2}{2\mu_0 c}$ such that

$$I(z) = I_0 e^{-\kappa z}. \tag{43}$$

In general, the index of refraction of a material is dependent upon its permittivity ϵ and permeability μ:

$$n^2 = \frac{\epsilon}{\epsilon_0}\frac{\mu}{\mu_0}. \tag{44}$$

Because ^{87}Rb has a single valence electron, the atoms are paramagnetic and $\mu \approx \mu_0$. In addition, the permittivity is related to the susceptibility χ by $\epsilon = \epsilon_0(1+\chi)$. For a dispersive material, the real (χ_r) and imaginary (χ_i) parts of the frequency-dependent susceptibility $\chi(\omega) = \chi_r(\omega) + i\chi_i(\omega)$ are connected through the Kramers-Kronig relations, a pair of Hilbert transforms in in the form of principal value integrals [55].

$$\chi_r(\omega) = \frac{2}{\pi} PV \left[\int_0^\infty \frac{s\chi_i(s)}{s^2 - \omega^2} ds \right] \tag{45}$$

$$\chi_i(\omega) = \frac{2}{\pi} PV \left[\int_0^\infty \frac{\omega \chi_r(s)}{\omega^2 - s^2} ds \right] \tag{46}$$

We can find a relationship between χ and n:

$$\chi_i = 2n_i \tag{47}$$

$$\chi_r = 2(n_r - 1). \tag{48}$$

The susceptibility is related to the polarizability of the ensemble as given by

$$\overrightarrow{P} = \frac{\epsilon_0 E_0}{2} \left(\chi(\omega) e^{-i\omega t} + \chi(-\omega) e^{i\omega t} \right) \overrightarrow{\epsilon}. \tag{49}$$

Given an ensemble with a density n_0, the polarizability is proportional to the average dipole moment $\langle \overrightarrow{d} \rangle$ for a single atom:

$$\overrightarrow{P} = n_0 \langle \overrightarrow{d} \rangle = n_0 \langle \Psi(t) | q\hat{\epsilon} \cdot \overrightarrow{r} | \Psi(t) \rangle. \tag{50}$$

Using Eqns. 3 and 11 and comparing Eqns. 49 and 50 yields

$$\chi(\omega) = \frac{1}{3} \frac{n_0 q^2}{\epsilon \hbar} |\langle 1|r|0\rangle|^2 \frac{1}{\omega_{10} - \omega - i\gamma/2}. \tag{51}$$

Thus, the imaginary part of the susceptibility is

$$\chi_i = \frac{1}{3} \frac{n_0 q^2}{\epsilon_0 \hbar} |\langle 1|r|0\rangle|^2 \frac{\gamma/2}{\delta^2 + (\gamma/2)^2} \tag{52}$$

and the real part, which leads to dispersion in the phase velocity of the wave is

$$\chi_r = \frac{1}{3} \frac{n_0 q^2}{\epsilon_0 \hbar} |\langle 1|r|0\rangle|^2 \frac{-\delta}{\delta^2 + (\gamma/2)^2}. \tag{53}$$

Finally, the cross-section σ for light scattering from an individual atom with ground state F and excited state F' to remove energy from the plane wave is $\sigma = \frac{\kappa}{n_0}$. Substituting Eqn. 52 in Eqn. 42, and noting that $\lambda = 2\pi c/\omega$, gives the total cross-section

$$\sigma = \frac{2F' + 1}{2F + 1} \frac{\lambda^2}{2\pi} \frac{1}{1 + (2\delta/\gamma)^2}. \tag{54}$$

The attenuation of the intensity of the plane wave due to propagation through the entire

medium follows Beer's Law (also known as the Beer–Lambert–Bouguer law.) The final intensity I_T is reduced from the initial intensity I_0 due to the optical depth b of the system:

$$I_T = I_0 e^{-b}. \tag{55}$$

The unitless optical depth b is dependent on multiple factors of the medium, which include density, the length of the sample, and the atomic cross section σ. For any given sample, b is given by

$$b = \int_{-\infty}^{\infty} \sigma n(z) dz \tag{56}$$

where $n(z)$ is the number density in the direction of propagation z.

2.5 DIFFUSION AND RANDOM WALKS

As photons propagate through a medium, they undergo a multitude of scatterings. This results in the light being scattered randomly in any direction, as depicted in Fig. 1. According to the Ewald-Oseen theorem, the total scattered electric field $\overrightarrow{E_T}$ is the superposition of the incident field $\overrightarrow{E_0}$ and the field radiated from dipoles in the medium $\overrightarrow{E_S}$

$$\overrightarrow{E_T} = \overrightarrow{E_0} + \overrightarrow{E_S}. \tag{57}$$

The scattered field in the medium is

$$\overrightarrow{E_S}(z) = -\overrightarrow{E_0} e^{i\kappa z} + \frac{2}{n(\omega)+1} \overrightarrow{E_0} e^{in(\omega)\kappa z} \tag{58}$$

which has a component that exactly cancels with the incident field [56]. Thus, the intensity appears to be attenuated in the forward direction.

For a diffusely scattering medium, in which the scatterers are randomly distributed and not situated in a lattice, the fluorescence that is observed off-axis from the original excitation can be considered incoherent [57]. This is due to spatial averaging of the phase dependence of the scattered light. The photon distribution in space at any time is given by $\Phi = \Phi(\overrightarrow{r} t)$, and can be solved using the diffusion equation

$$\frac{\partial \Phi}{\partial t} = \overrightarrow{\nabla} \cdot \left(D(\overrightarrow{r}) \overrightarrow{\nabla} \Phi \right). \tag{59}$$

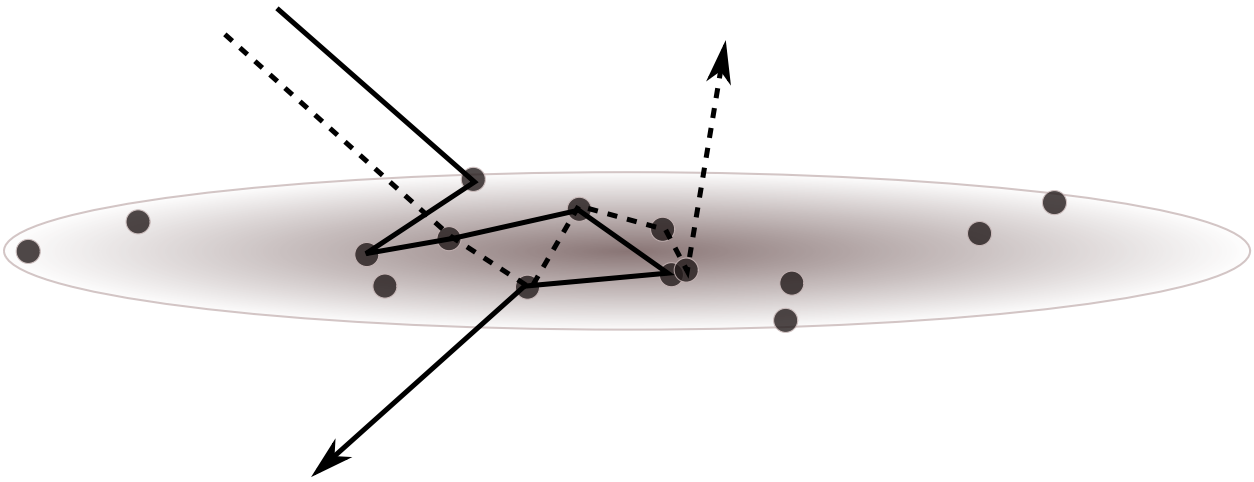

FIG. 1: As photons travel through an atomic sample, their paths (indicated by the arrows) are randomized as they scatter off atoms (circles).

Here $D(\overrightarrow{r})$ is the density dependent diffusion coefficient [58], [59]. For a photon initially located at $\overrightarrow{r_0}$ at $t = 0$ within an infinite, isotropic, homogeneous sample, the three dimensional solution of the diffusion equation yields

$$\Phi = \frac{1}{(4\pi Dt)^{3/2}} e^{-|\overrightarrow{r}-\overrightarrow{r_0}|^2/(4Dt)} \tag{60}$$

and the diffusion coefficient is

$$D = \frac{l v_E}{3}. \tag{61}$$

Here we have introduced the mean free path l of the sample, which is the average distance a photon will travel between scattering events. The rate at which the energy is transported through the sample is v_E. Given a sample density n and atomic cross-section σ, the mean free path is

$$l = \frac{1}{n\sigma}. \tag{62}$$

In reality, the atomic sample used in the experiment is not isotropic, but has a bi-Gaussian density distribution. In order to simulate this diffusive process, a discretized random walk can be used [57]. Averaging over many random walks of photons through the medium will replicate the diffusion model. The solution will not account for the phases of individual photons, which contribute to coherent backscattering and attenuation in the forward direction, so this model should only be used to observe off-axis scattering.

2.5.1 A 3D RANDOM WALK MODEL

A 3D random walk model has been developed to describe the spatial distribution of the scattered light from an atomic sample, the results of which will be compared to the experimental results. Due to computational power constraints, a maximum of 10,000 atoms are used. Keeping the number of atoms in the simulation constant, the relative length scales are then modified to reproduce the same density as that found in the experiment. The simulation distance d_{sim} scales with the experimental distance d_{exp} as

$$d_{sim} = d_{exp}\left(10^4/N\right)^{1/3}, \tag{63}$$

where N is the number of atoms in the experiment.

Each atom a_i can be described by its center of mass position $\overrightarrow{r_i}$. The distribution of N atoms can be described by a three dimensional bi-Gaussian density distribution

$$n(\overrightarrow{r}) = n_0 e^{-r_\perp^2/(2r_0^2) - z^2/(2z_0^2)}, \tag{64}$$

$r_\perp^2 = x^2 + y^2$, with radii r_0 and z_0 and peak density n_0,

$$n_0 = \frac{N}{(2\pi)^{3/2} r_0^2 z_0}. \tag{65}$$

The physical radius R of each atom is found from the cross-section

$$\sigma = \pi R^2. \tag{66}$$

The cross-section for the $F = 2 \rightarrow F' = 3$ transition is used. Using Eq. 54, the radius is

$$R = \left(\frac{2F'+1}{2F+1}\frac{\lambda^2}{2\pi^2}\frac{1}{1+(2\delta/\gamma)^2}\right)^{1/2}. \tag{67}$$

Therefore, R is greatest on resonance and the atoms effectively become smaller as the detuning δ becomes greater.

An atom outside of the sample is given a position $\overrightarrow{r_0}$ chosen from a uniform random distribution to mimic the constant intensity of the probe over the distribution of atoms. This first atom is forced to decay in the direction $\hat{k}$ of the probe. The position of the photon $\overrightarrow{p}$ over time is $\overrightarrow{p} = \overrightarrow{r_0} + vt\hat{k}$. The closest distance between each atom and the photon's

path is

$$d_i = \frac{|(\overrightarrow{r_i} - \overrightarrow{r_0}) \times (\overrightarrow{r_i} - \overrightarrow{p})|}{|\overrightarrow{p} - \overrightarrow{r_0}|}. \tag{68}$$

The closest atom a_j to a_0 that has $d_j \leq R$ will scatter the photon. At that point the photon will scatter into a random direction $\hat{k}_j$ with uniform probability and will be described by the vector $\overrightarrow{r_j} + \hat{k}_j$. This scattering process will continue until the photon does not scatter from any of the atoms in the sample. The final position of the photon is found from propagating the last decay path out to a distance of $10z_0$ from the center of the sample. A sample of the Mathematica program written to model a three dimensional random walk of a photon in an atomic sample with the same geometries and characteristics as the samples in the diffuse scattering experiment is shown in Appendix A.

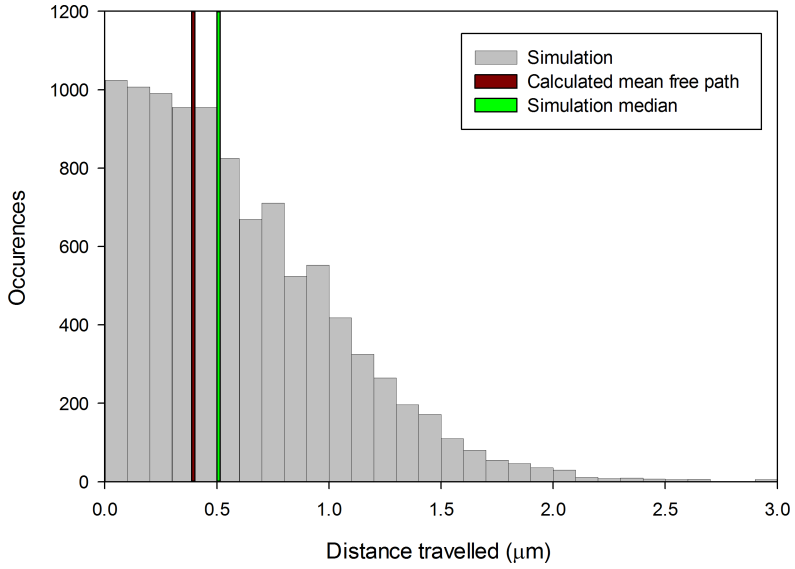

FIG. 2: This histogram shows the distribution of distances a photon - initially positioned at the center of the sample - travels to the first scattering event. The theoretical mean free path l_0 is 395 nm, while the median of this distribution gives $l = 508$ nm.

One critical test to make sure this model fairly describes the atomic system is to check the path length of the photons. For a sample with a relatively low density n_0, in which dipole-dipole interactions are negligent, the mean free path l_0 for a photon initially at the center of the sample should be

$$l_0 = \frac{1}{n_0 \sigma}. \tag{69}$$

As shown in Fig. 2, the simulation agrees fairly well with theory in approximating the mean free path. While the photon travels through the sample, the mean free path l is actually

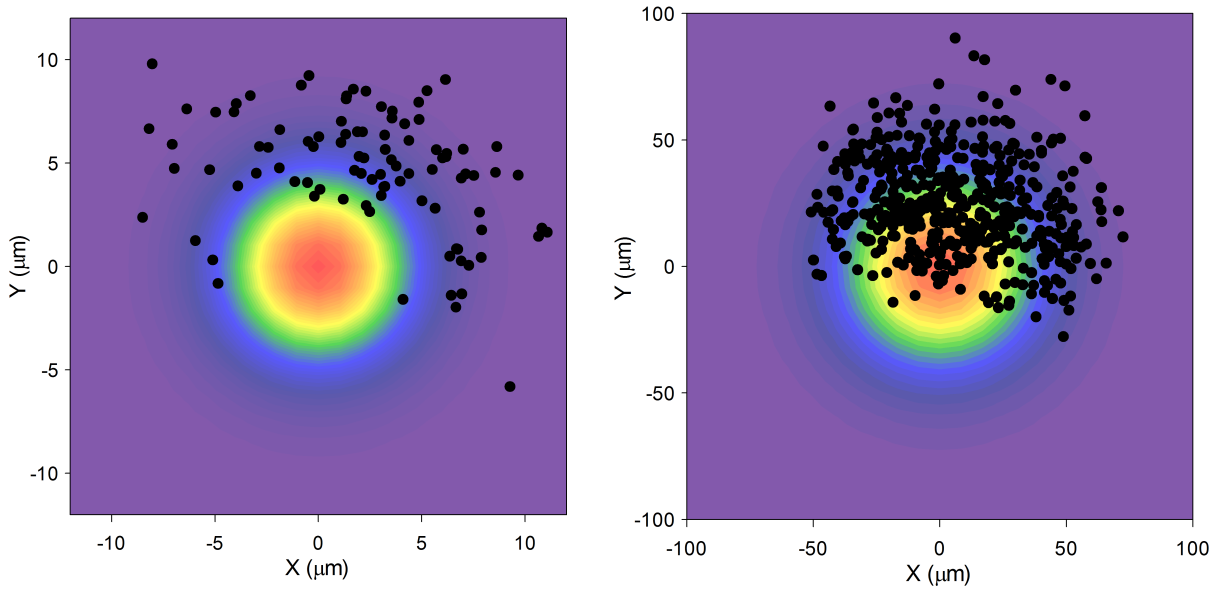

(a) 18.7 atoms/μm^3

(b) 0.25 atoms/μm^3

FIG. 3: The radial position ($r_\perp^2 = x^2 + y^2$) of the first atom to scatter each photon is shown in black, overlapping a contour plot that indicates the density of the atomic sample. a) At a peak density of 18.7 atoms/μm^3, we see that initial scattering takes place near the effective surface of the sample. b) At a density of 0.25 atoms/μm^3, we see that the photons are able to penetrate into the sample before scattering.

position dependent:

$$l\left(\overrightarrow{r}\right) = \frac{1}{n\left(\overrightarrow{r}\right)\sigma}. \tag{70}$$

The reduction in density with distance contributes to the increase in the mean free path.

By recording the position of the first atom that scatters each photon, we can see how the light is able to penetrate further into the sample when the sample expands and the density is low. As shown in Fig. 3, the initial photons are unable to penetrate the atomic sample with a peak density of 18.7 atoms/μm^3. This means that most of the signal is from surface scattering. However, once the sample expands and the peak density is reduced to 0.25 atoms/μm^3, the photons are able to travel far into the sample before scattering. Notice as well that the number of photons scattered is increased drastically as the physical size of the sample increases.

More information can be learned from recording the number of times an individual photon is scattered within the sample. An example of these results for both a low and high density (large and small volume) can be found in Fig. 4. We see that with smaller sample radii, the

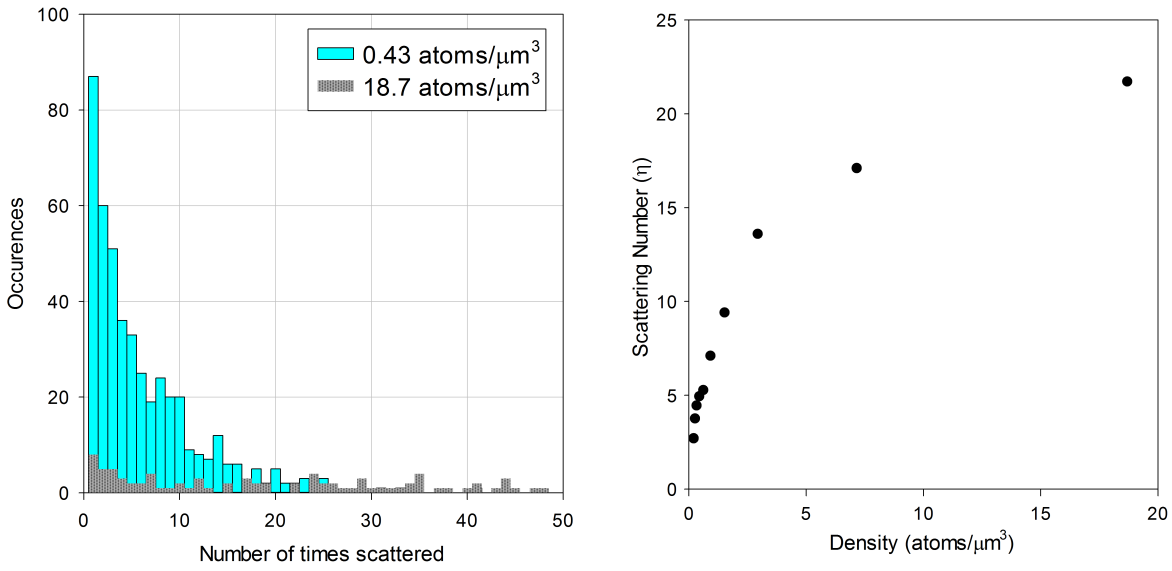

(a) (b)

FIG. 4: a)The distribution of the number of times an individual photon is scattered within the sample is shown for 780,000 atoms but two different volumes corresponding to densities of 18.7 atoms/μm^3 and 0.43 atoms/μm^3. b)As a sample expands, the scattering number η is reduced, such that photons transition from multiple scattering to single scattering events.

total number of photons scattered is reduced due to the reduction of the physical size of the sample, but the photons that are scattered undergo multiple scattering. Conversely, with physically large sample, a large percentage of photons are only scattered a few times.

Fitting the number of occurrences O as a function of the number of scatterings N to a decaying exponential

$$O = O_0 e^{-N/\eta} \tag{71}$$

we can define a scattering number η that corresponds to the number of times a single photon is scattered. Likewise, the total number of photons scattered, and the number of single scattering photons, is shown in Fig. 5. These figures show that for high density samples the number of scattered photons is reduced, but they undergo multiple scattering; for samples with larger volumes, the number of scattered photons is increased, and they are able to penetrate the sample more, but they do not rescatter as frequently.

By recording the final position of all of the photons, the spatial scattering distribution is found. The number of atoms, radii of the sample, and detuning of the probe beam are

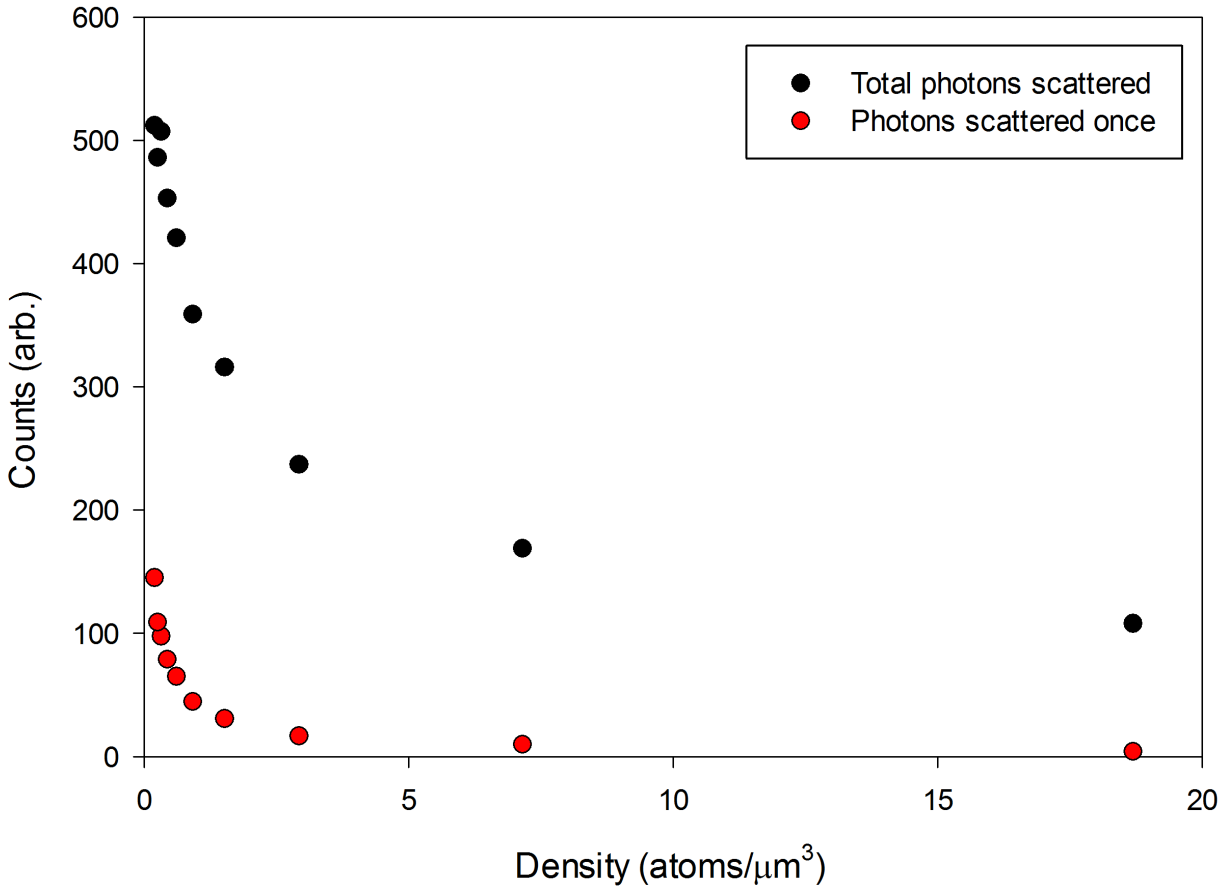

FIG. 5: The total number of scattered photons increases as the sample expands and the density is reduced. At higher densities (lower volumes), photons are more likely to undergo multiple scattering.

changed to study their effects on the scattering distribution and to compare with experimental results. As stated before, this model does not include the phase of the scattered light, but only contains information on the final position. As such, this would not be an accurate model for forwards or backwards scattering, but is suitable for diffuse scattering.

CHAPTER 3

EXPERIMENTAL SETUP

This chapter begins with the optical and electronic setups required to create the cold atomic ^{87}Rb sample. After the sample is created, numerous characterization techniques are used to fully quantify the sample parameters. Finally, a description of the experimental setup to observe diffuse scattering is given at the end of this chapter.

3.1 RUBIDIUM

Rubidium is an alkali metal with two main isotopes (^{85}Rb and ^{87}Rb). It is a convenient element to work with in cold atomic physics, as narrow-band laser diodes (with wavelengths near the ground state resonance transitions) are both economic and readily available. Additionally, rubidium's spectroscopic properties are well understood due to the similarities to the hydrogen atom, since there is only one valence electron. A Grotrian diagram showing many of the lowest electronic energy levels of rubidium is shown in FIG. 6.

The relevant transitions for this experiment, shown in FIG. 7, are from the ground state $5s^2S_{1/2}$ to the first excited state $5s^2P_{3/2}$, which is known as the D2 line. The essential properties of ^{87}Rb are shown in Table 1, along with the $5^2S_{1/2} \rightarrow 5^2P_{3/2}$ transition optical properties. Due to coupling between the nuclear spin **I** with the total electronic angular

Atomic Number	Z	37
Atomic Mass	m	1.443160648(72) $\times 10^{-25}$ kg
Nuclear Spin	I	3/2
Ionization Limit	E_I	4.17712706(10) eV
Lifetime	τ	26.2348(77) ns
Decay rate	γ	$2\pi \times 6.0666(18)$ MHz
Saturation Intensity (circular light polarization)	I_s	1.66933(35) mW/cm^2
Total cross section (isotropic light polarization)	σ_0	1.356456704271(31) $\times 10^{-9}$ cm^2

TABLE 1: Properties of atomic ^{87}Rb and the $5^2S_{1/2} \rightarrow 5^2P_{3/2}$ transition optical properties [61]

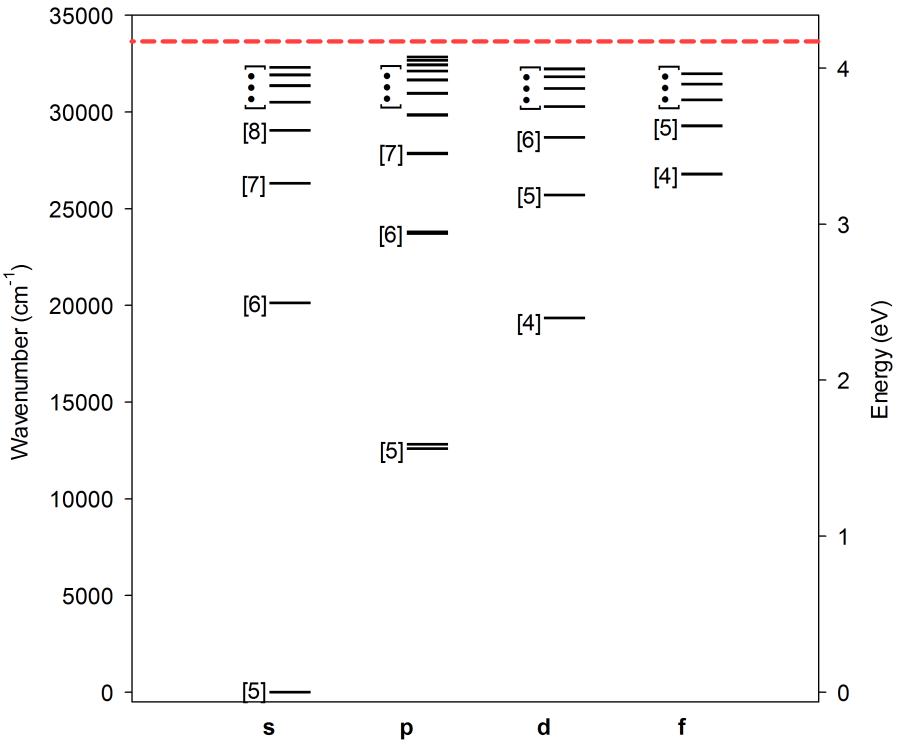

FIG. 6: This Grotrian diagram shows the lowest energy levels of rubidium, with wavenumbers given by [60]. The ground state configuration is $5s^2S_{1/2}$, and the ionization energy, indicated by the red dashed line, is 4.18 eV. $[n]$ indicates the nth level, and the ellipses indicate a progression of n towards higher excited states nearing the continuum. The letters s, p, d, and f indicate states with electronic orbital angular momentum L = 0, 1, 2, and 3 respectively.

momentum $\mathbf{J}$, $\mathbf{J} = \mathbf{L} + \mathbf{S}$, the energy levels are split into what are known as hyperfine levels. The total angular momentum is thus

$$\mathbf{F} = \mathbf{I} + \mathbf{J}, \tag{72}$$

and the magnitude F is an integer in the range

$$|J - I| \leq F \leq J + I. \tag{73}$$

The Hamiltonion is

$$H_{hfs} = A_{hfs}\mathbf{I}\cdot\mathbf{J} + B_{hfs}\frac{3(\mathbf{I}\cdot\mathbf{J})^2 + \frac{3}{2}(\mathbf{I}\cdot\mathbf{J}) - I(I+1)J(J+1)}{2I(2I-1)J(2J-1)}, \tag{74}$$

Magnetic Dipole Constant - $5s^2S_{1/2}$	A_{hfs}	3417.341 MHz
Magnetic Dipole Constant - $5s^2P_{3/2}$	A_{hfs}	84.845 MHz
Electric Quadrupole Constant - $5s^2P_{3/2}$	B_{hfs}	12.52 MHz

TABLE 2: The relevant magnetic dipole and electric quadrupole constants contribute to the energy splittings due to hyperfine interactions [52].

which results in hyperfine energy splittings

$$\Delta E_{hfs} = \frac{1}{2}A_{hfs}K + B_{hfs}\frac{\frac{3}{2}K(K+1) - 2I(I+1)J(J+1)}{4I(2I-1)J(2J-1)} \tag{75}$$

where

$$K = F(F+1) - I(I+1) - J(J+1) \tag{76}$$

The magnetic dipole constants A_{hfs} for the ground and excited states, and the excited state electric quadrupole constant B_{hfs}, have been experimentally measured and are listed in Table 2 [52, 53, 61]. The same type of selection rules for dipole transitions from the ground to the excited state still apply. Namely, the change in the total angular momentum must be zero or 1:

$$\Delta F = 0, \pm 1. \tag{77}$$

Additionally, the change in the magnetic quantum number m_F depends on the polarization of the excitation. For linearly polarized light, $\Delta m_F = 0$, while for light of $\sigma\pm$ polarization, $\Delta m_F = \pm 1$.

By using a narrow-band continuous wave (CW) laser, we can drive transitions with great precision. The laser used to probe the $F = 2 \rightarrow F' = 3$ transition has a bandwidth of $\sim$ 1 MHz, much less than the hyperfine splittings shown in FIG. 7. As such, when the probe is tuned near resonance, the ^{87}Rb atoms can be considered to a good approximation as only having two levels. The other hyperfine levels are far enough away that there is little spectroscopic contribution to the scattering process.

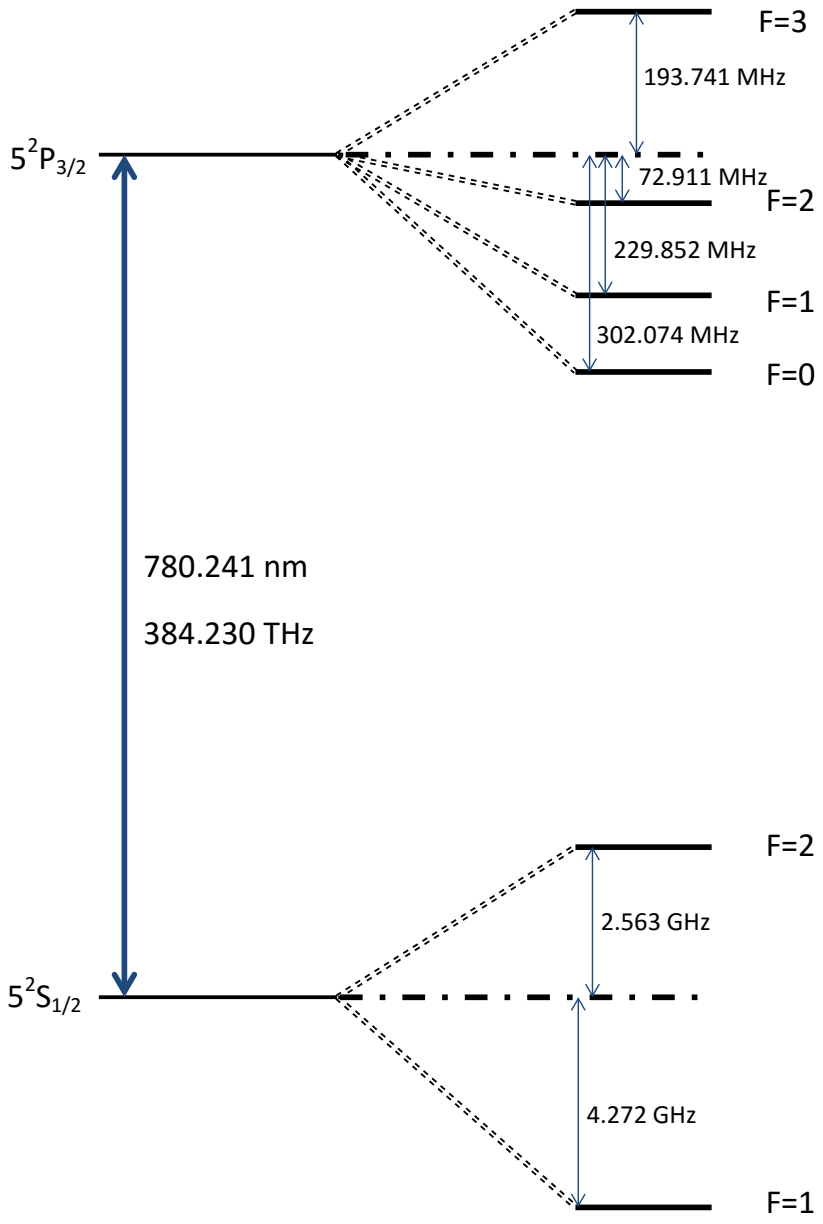

FIG. 7: The hyperfine structure for the relevant transitions for this experiment is shown (not to scale.) The ground level hyperfine splitting is 6.8 GHz, while the excited levels span nearly 500 MHz.(Values from [61])

3.2 LASERS

Lasers are truly the workhorse of cold atomic physics. Since the 1980's, the techniques and resources for using laser diodes has greatly improved [62]. They have been critical in cooling and trapping atoms; from creating an optical molasses [63], to cooling atoms below the Doppler limit [64,65], lasers have been at the forefront of experimental progress in atomic physics. In this section, the various types of lasers utilized for this experiment are outlined. Additionally, the optical arrangements and techniques for locking and manipulating the lasers' properties are described. For this thesis, a combination of extended cavity diode lasers (ECDLs), a distributed feedback laser (DFB), and a fiber laser are used to create and probe the sample. We utilize two locking techniques - Doppler free saturated absorption and injection locking- to stabilize the ECDLs and DFB.

3.2.1 EXTENDED CAVITY DIODE LASER (ECDL)

A free-running diode laser may lase at a wavelength far from the desired wavelength. By placing a diffraction grating in the laser beam's path and diffracting the first order back into the diode, a cavity is created. The optical feedback from the grating allows the diode to be tuned over a range of frequencies. Because the grating is outside of the physical structure of the diode as shown in FIG. 8, this setup is known as an extended cavity diode laser (ECDL). This specific setup is known as the Littrow configuration. While ECDLs are historically known as being finicky [62], they produce laser beams that have narrow linewidths (on the order of 1 MHz), and can be stable over the course of an experimental run.

While commercially available as a package, the ECDLs in this experiment are home-built. We use a diode purchased from ThorLabs (# DL7140-201S) capable of emitting 70 mW of power. The construction of the laser enclosure and the mounts to hold the components in place was chiefly performed by a previous graduate student [41]. There are three main ways to control the wavelength/frequency of the ECDL: current, temperature, and diffraction grating angle. A home-built current controller supplies power to the diode and is tuned so the laser is close to the desired wavelength. Because the cavity length (and therefore the cavity frequency) is temperature dependent, a thermoelectric cooler (TEC) is placed in close contact with the laser diode. A home-built temperature controller stabilizes the temperature of the diode so that slow drifts in room temperature do not disturb the diode or cavity. Finally, the grating is mounted on a piezo electric transducer (PZT). Applying a voltage to the PZT causes it to change in length, thereby slightly extending or contracting

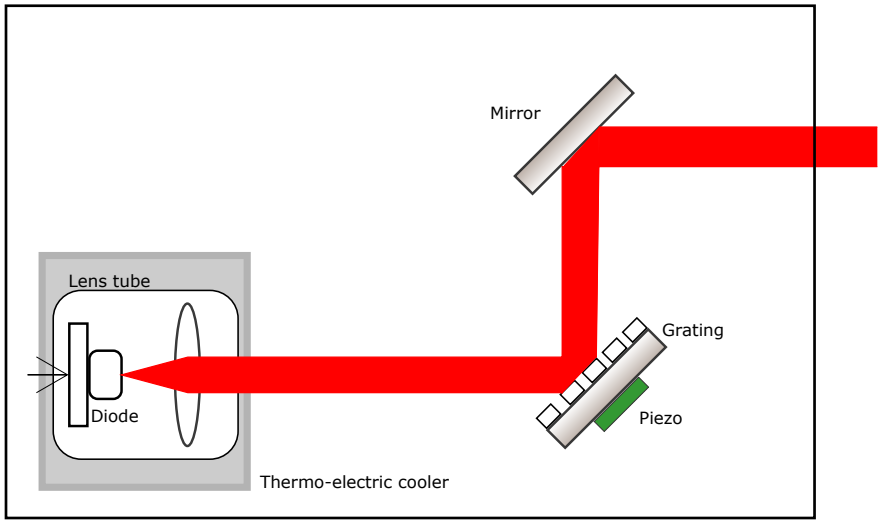

FIG. 8: A schematic of a Littrow configuration ECDL is shown. The light emitted from the diode is collimated using a lens, and then is incident on a diffraction grating. The first order is diffracted back to the diode, while the zeroth order is reflected towards a mirror where it is then directed outside of the laser enclosure.

the length of the cavity. Therefore, the PZT is used to fine-tune the frequency of the ECDL. More details of how the current and PZT are used will follow in a later section.

3.2.2 DISTRIBUTED FEEDBACK LASER (DFB)

Another type of laser used in this experiment is a distributed feedback laser (DFB), purchased from Eagle Yard (part # EYP-DFB-0780-00080-1500-TOC03-0000.) For this laser, a commercial dual current and temperature controller (SRS # LDC501) is used. While the DFB is capable of providing up to 80 mW of power, it is very sensitive to optical feedback from reflections off of various optics. It is important to isolate as many of the reflections as possible. Additionally, noisy current and temperature controllers can easily disturb the DFB. We have observed that both electrical noise and reflections can broaden the spectral width of the DFB from the stated value of 2 MHz up to 6 MHz, so great care must be taken to achieve stated linewidths.

3.2.3 FIBER LASERS

Finally, the last type of laser used in this experiment is a fiber laser. Whereas the ECDL uses a semiconductor as the gain medium, the fiber laser uses a fiber doped with ytterbium

to create gain. At a wavelength of 1.064 μm, the fiber laser (IPG Photonics # YLR-30-1064-LP) is capable of providing up to 30 W of power. Care must be taken while aligning and using this laser, as the power is much greater than that of a diode laser, and it is beyond the spectral range of the human eye. Use of an infrared viewer is required to view the laser beam. If the fiber laser is focused, it is easily capable of catching paper, clothes, and wood on fire.

3.2.4 OPTICAL ARRANGEMENTS

There are two optical tables used in this experiment. The first, named the laser table, includes the ECDLs and DFB, as well as the associated optics and electronics. The laser table is used to condition the frequencies of these lasers to the desired values. The second optical table, known as the experiment table, is used to create the atomic sample. This is also where the fiber laser is held. Laser beams are transferred from the laser table to the experiment table through fiber optic patch cables. In this section, the optical layouts for the laser table are described. The optical elements key is located in the preface on page vi.

For this experiment, there are two major optical transitions of concern, shown in Fig. 9. The trapping transition is the nearly closed $5S_{1/2}, F = 2 \rightarrow 5P_{3/2}, F' = 3$ transition. The ECDL tuned near this transition is colloquially called the MOT laser. The second transition is driven by the ECDL that is called the repumper laser. Due to off resonance Raman transitions, some atoms excited by the MOT laser are actually in the $F' = 2$ state. As such, they have the ability to decay to the $F = 1$ state. The repumper, tuned to the $5S_{1/2}, F = 1 \rightarrow 5P_{3/2}, F' = 2$ transition is used to "repump" those atoms back into the $F = 2$ ground state. The probe laser is picked off from the MOT laser and is tuned about the $F = 2 \rightarrow F' = 3$ transition as well.

Shown in Fig. 10, the repumper laser layout is the least complex on the laser table. The ECDL, which is very close to the surface of the laser table, requires a periscope to make further alignments easier to manage. Directly after the periscope is an optical isolator (OFR # IO-3-780-PSCL), which relies on Faraday rotation to reduce the transmission of reflections back towards the diode. There is then a pick-off that reflects a small percentage of the intensity towards a saturated absorption (SA) setup (described in the next section) to frequency lock the laser. The light that is transmitted through the pick-off goes through an acousto-optic modulator (AOM) (Gooch & Housego # R23080-1-LTD). AOMs are a valuable tool for fine-tuning the frequency of a laser beam. They may also be used as a switch, as their turn-off time is much shorter than that of a mechanical shutter. A transducer

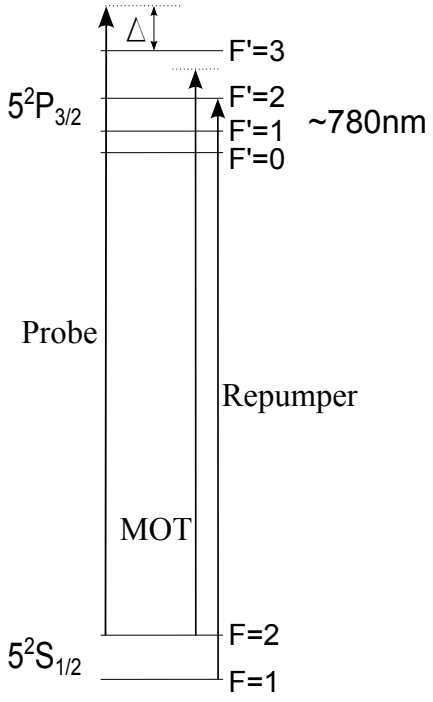

FIG. 9: The probe, MOT, and repumper lasers are tuned to the relevant transitions for this experiment. (Not to scale.)

is attached to a crystal inside the AOM. Modulation of the transducer at a determined frequency causes an acoustic wave to propagate through the crystal. A laser beam traveling nearly perpendicular to the transducer will experience Bragg diffraction, and the optical frequency of the transmitted light is increased (decreased)in the +1 (-1) order by the same amount as the frequency of the acoustic wave [66]. Finally, the +1 order beam from the AOM is launched into a non-polarization preserving fiber to go to the experiment table.

Shown in Fig. 11, the MOT laser layout is more complex than that of the repumper. However, the same basic optics are used. In addition, polarizing beam splitter cubes are used in conjunction with half-wave plates to control the polarization and intensity through different segments of the setup. In the MOT laser setup, two double pass (DP) AOM setups are used. In a DP AOM layout, the frequency of the first transmitted laser beam is shifted by the frequency of the AOM. Taking that same order and reflecting it back through the AOM creates a doubly transmitted laser beam that has a net frequency change of twice the

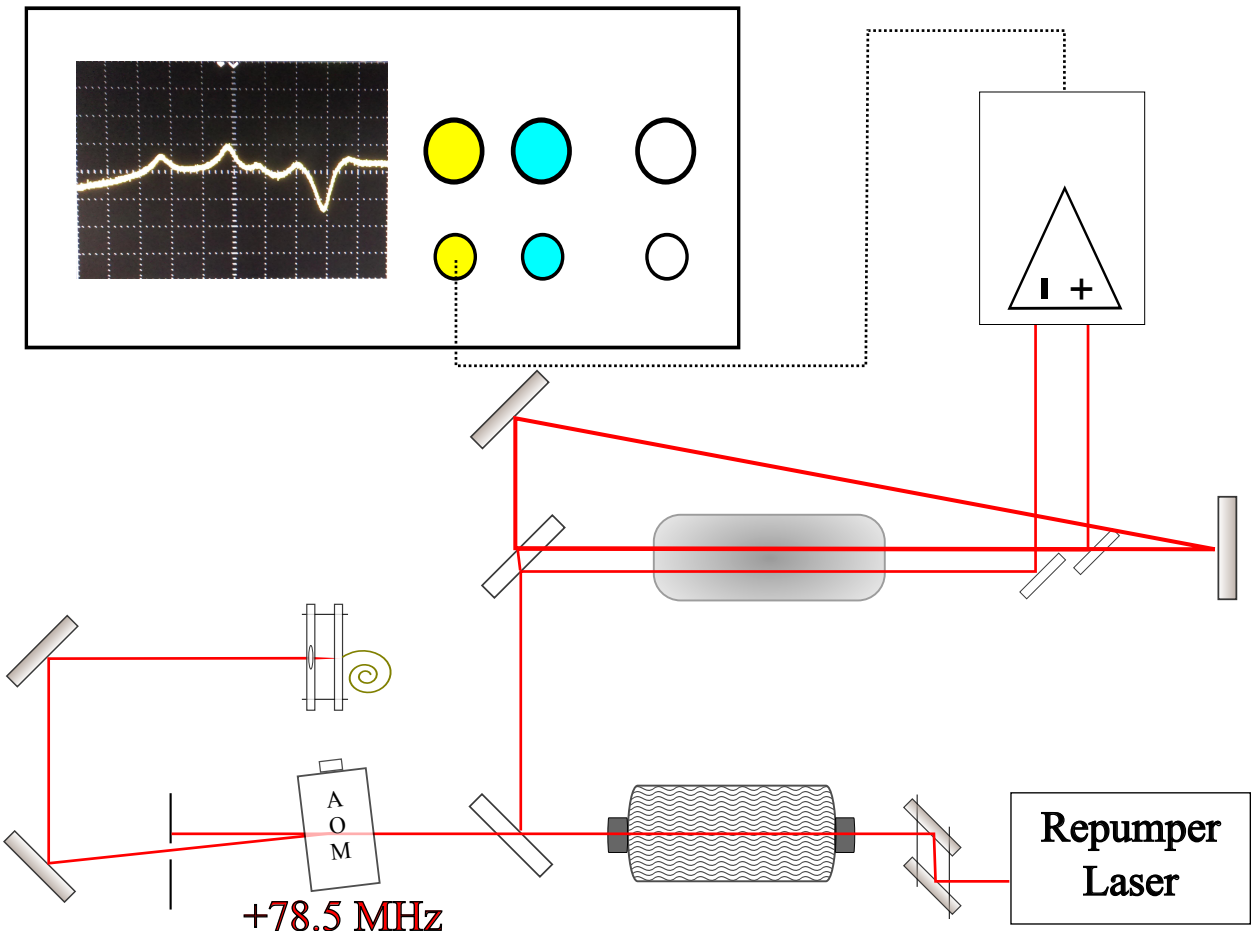

FIG. 10: The optical layout for the repumper laser is shown.

frequency at which the AOM is operated. The first DP AOM (Brimrose # EM200-50-780) setup is located so that only the light going to the saturated absorption is shifted. This AOM is denoted as DP_{SA} AOM, while the other DP AOM (also Brimrose # EM200-50-780) setup shifts the rest of the light that is not picked off to go through the SA.

After passing through a DP AOM, the intensity of the MOT laser is greatly reduced. To increase the power available to trap and probe the atoms, the MOT laser and DFB are set up in a master-slave configuration. The rest of the optical layout for the laser table is shown in Fig. 12. The optical isolator for the DFB (ThorLabs # IO-8-780-PBS) is much stronger than the other two used and has an isolation of 35 dB, which helps with stability of the DFB. After the isolator, a telescope is used to reduce the waist size of the laser. A small portion of the intensity is picked off and used as the probe, while the remaining laser beam passes through another AOM (Gooch & Housego # R23080-1-LTD) and is then fiber

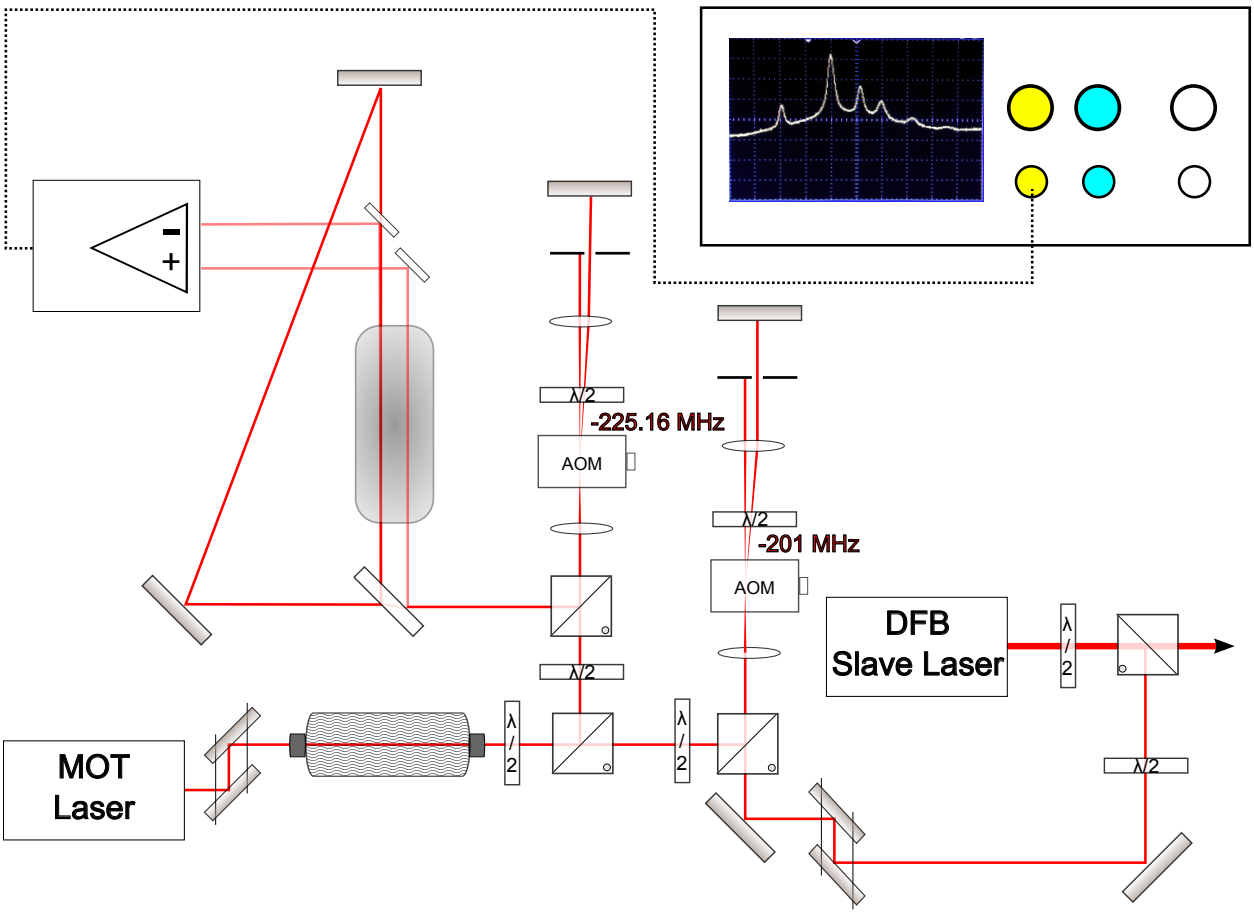

FIG. 11: The optical layout for the MOT laser is shown.

launched through a polarization preserving fiber to the experiment table. The intensity of the trapping laser at the experiment table is about 25 mW. The probe laser beam is sent through a different AOM (NEOS # 23080-1) before being attenuated by neutral density filters. Then, it is fiber launched through a polarization preserving fiber to the experiment table.

3.2.5 FREQUENCY STABILIZATION

In order to trap the ^{87}Rb atoms and selectively probe a single transition, most of the lasers must be frequency locked. Additionally, we require the ability to precisely tune the frequency. Two methods are utilized to frequency stabilize the lasers on the laser table. The primary method of stabilization, known as saturated absorption (SA), is described below. Both ECDLs use a feedback loop provided from their respective SA setups to stay

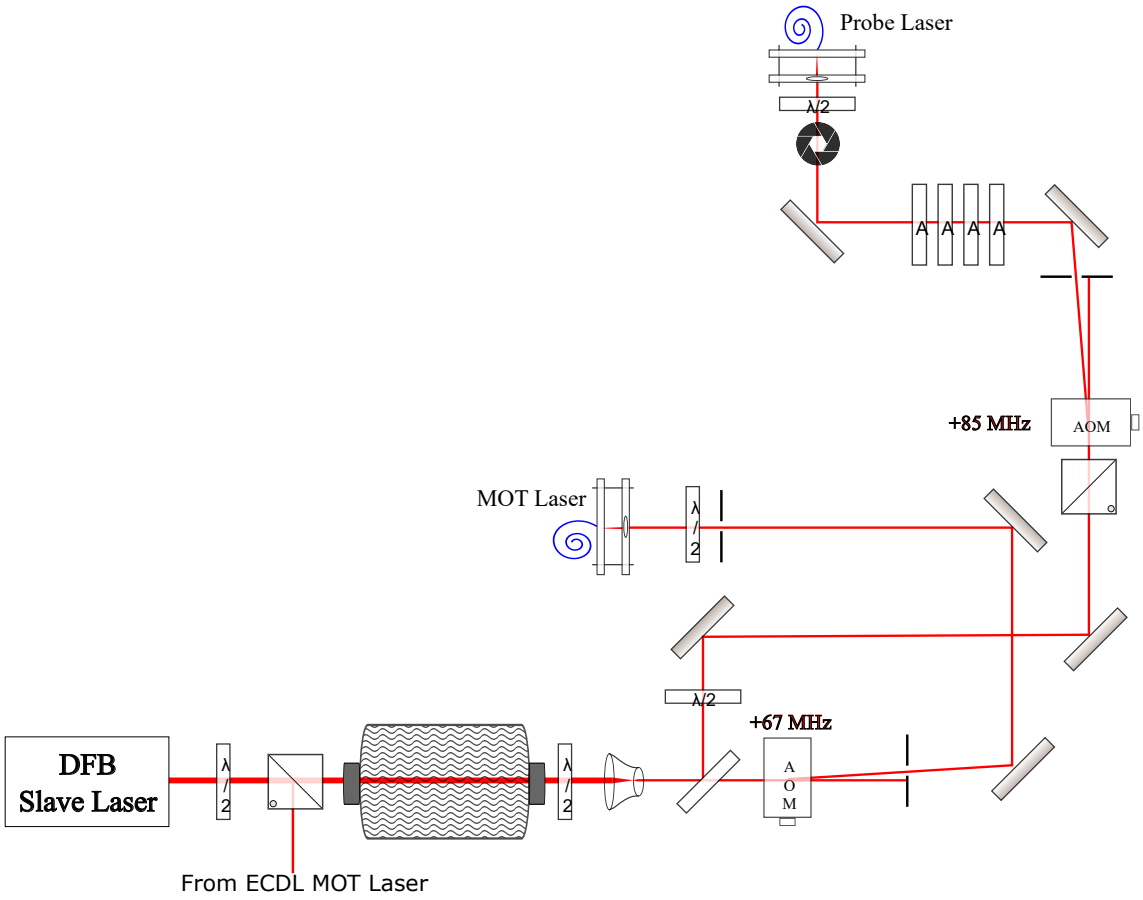

FIG. 12: The optical layout for the DFB laser is shown. The DFB is used to create the MOT trapping laser beam, as well as the probe.

locked at a set frequency. Additionally, the MOT ECDL and the DFB are in a master-slave configuration, in which the laser beam from the ECDL is injected into the DFB. If the DFB is lasing near the same frequency as the ECDL before injection occurs, then the DFB will behave as a slave and follow the ECDL master frequency [67]. Through the use of AOMs, individual laser beams can then have their frequency varied with respect to the locking frequency.

Saturated absorption

There are two key components to a saturated absorption (SA) setup: the optical layout, and the electrical setup used to lock the laser. The optical setup allows for viewing the

frequency of the laser beam and creates an electrical signal that can be used to provide a reference frequency at which to lock the laser. Electrical feedback loops then control the laser system to stabilize the laser frequency.

As shown in Fig. 13, a wedged pick-off creates two low intensity parallel laser beams (called probes) that propagate through a test cell filled with ^{87}Rb and ^{85}Rb atoms. As the near-resonance laser beams pass through the cell, some of the light is absorbed. The transmitted laser beams are directed towards a balanced photodetector, which takes the difference between the two spectroscopic signals. Because the atoms are at room temperature, their resonances undergo Doppler broadening, and subtraction of the two laser beams removes the Doppler-broadened piece of the signal. A critical part of the SA setup is the higher intensity laser beam (called the pump beam) that is reflected such that it is counterpropagating against one of the probe beams. An atom that has a velocity $\overrightarrow{v}$ will observe a laser beam

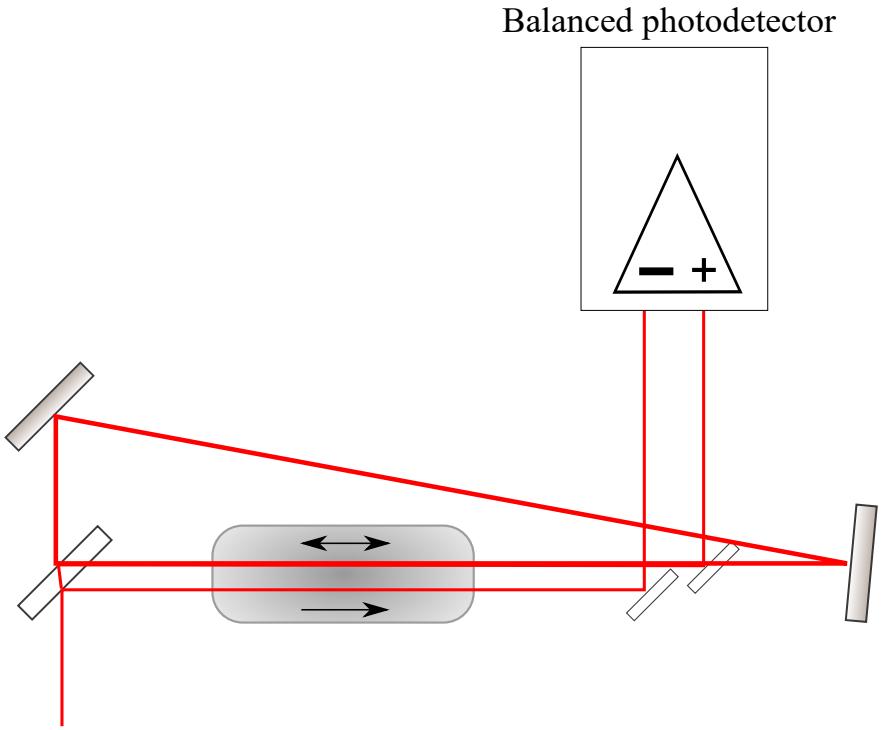

FIG. 13: Doppler-free saturated absorption provides a reference frequency at which to lock the ECDLs.

(propagating in the $\hat{k}$ direction with frequency f_L) at a Doppler-shifted frequency

$$f = f_L \left(1 + \frac{\overrightarrow{v} \cdot \hat{k}}{c}\right). \tag{78}$$

The probe-pump configuration in SA relies on this Doppler effect. Atoms that do not have a velocity component in the same direction as the laser beams will experience no shift, and will absorb light when the laser is at the resonant frequency. Atoms that are traveling towards the probe will observe higher frequencies, while atoms traveling away from the probe will observe lower frequencies, than the probe frequency in the lab reference frame. Because the probe and pump beams have the same frequency, but are counterpropagating, the atoms that are traveling towards the probe will be on resonance with a blue-shifted pump, and those traveling away from the probe will experience resonance with a red-shifted pump beam.

The maximum absorption of the probe for atoms with a non-zero velocity in the $\hat{k}$ direction will occur at what are known as cross-over frequencies, which are halfway between each resonance line. By applying a voltage ramp to the piezo in the ECDL, the frequency of the laser beam can be modulated to show the full SA spectrum. The spectrum will then show absorption lines for the non-shifted resonances and each cross-over resonance. The SA spectrum for the MOT and repumper lasers are shown in Figs. 14 and 15, respectively. The MOT SA shows the resonant transitions $F = 2 \rightarrow F' = 1, 2, 3$, as well as the cross-over resonances $F = 2 \rightarrow F' = 1 - 2, 2 - 3, 1 - 3$. Comparatively, the repumper SA shows the resonant transitions $F = 1 \rightarrow F' = 0, 1, 2$, as well as the cross-over resonances $F = 1 \rightarrow F' = 0 - 1, 1 - 2, 0 - 2$. Using electrical feedback loops, we can lock the lasers to the peaks of these resonances.

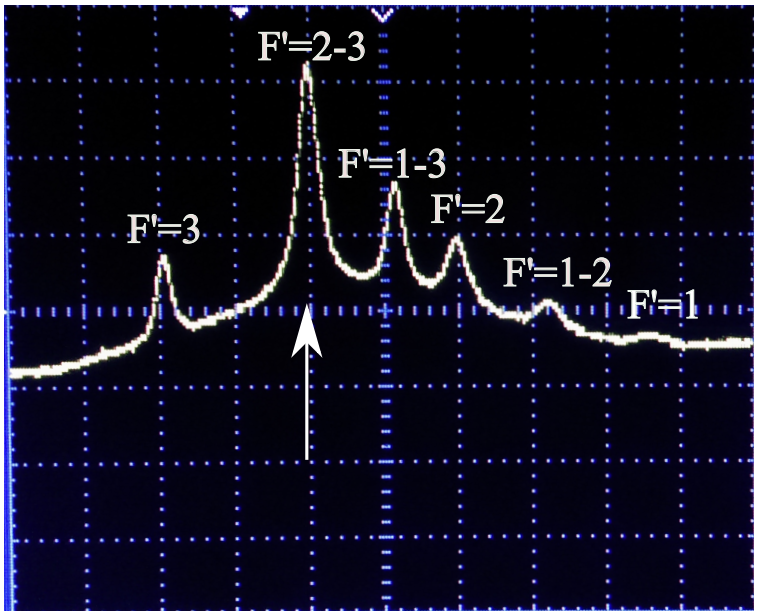

FIG. 14: Doppler-free saturated absorption of the MOT laser provides a reference frequency at which to lock the ECDL. The laser is locked to the $F = 2 \rightarrow F' = 2 - 3$ cross-over transition, as indicated by the arrow.

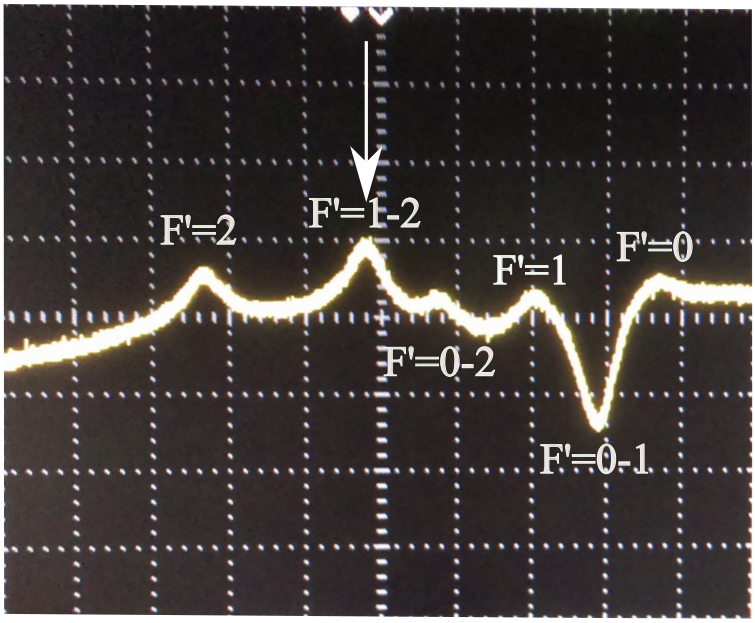

FIG. 15: Doppler-free saturated absorption of the repumper laser provides a reference frequency at which to lock the ECDL. The laser is locked to the $F = 1 \rightarrow F' = 1 - 2$ cross-over transition, as indicated by the arrow.

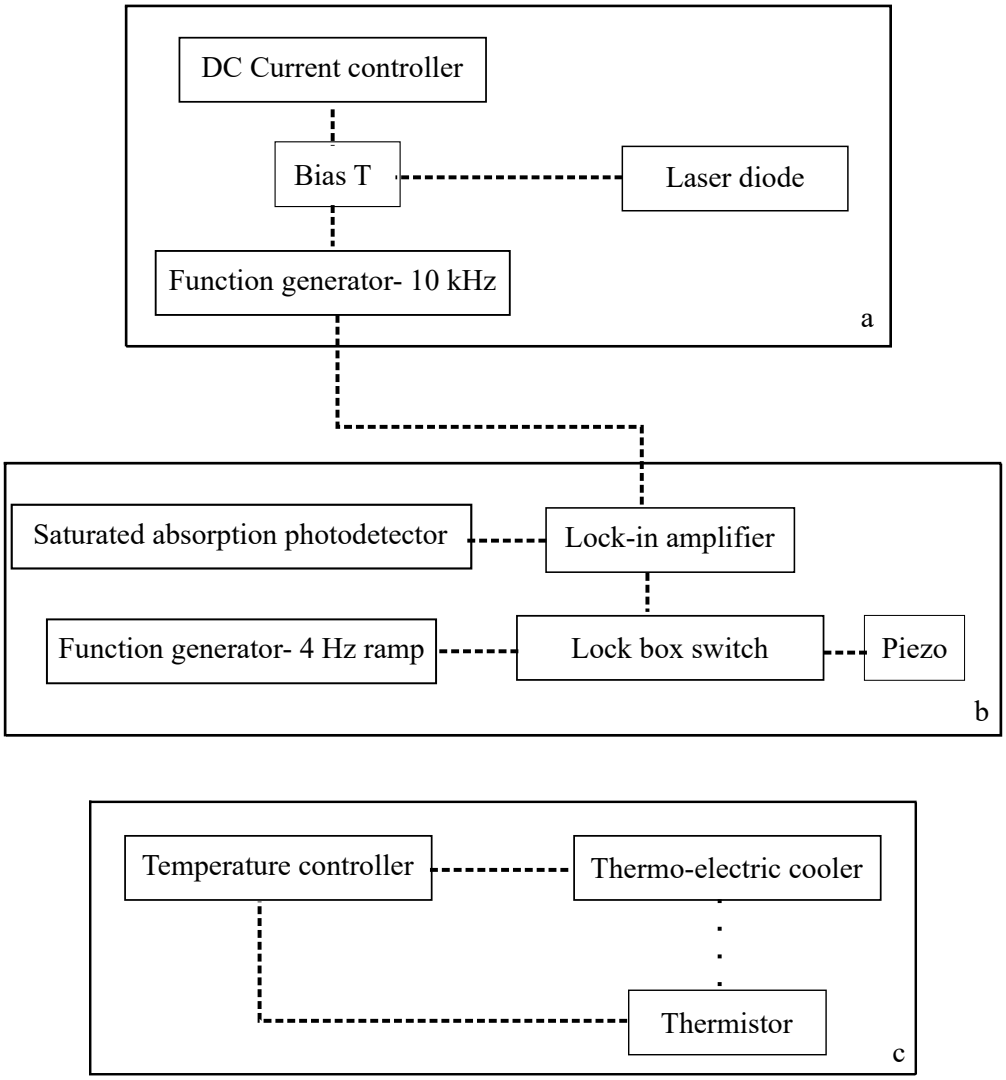

FIG. 16: Several electrical circuits are used to stabilize the ECDLs. a) A constant 10 kHz modulation in the current of the ECDL is used as a reference frequency for the lock-in amplifier. b) The SA photodetector voltage is used as an input to create a feedback loop to drive the piezo of the ECDL and keep it locked to a set frequency. c) The temperature is stabilized with the use of a thermo-electric cooler and thermistor.

Electronic feedback loops

Electronic feedback loops are used to stabilize the ECDLs. The basic setup is shown in Fig. 16. The laser diode is driven by a DC current controller, but a 10 kHz modulation is added to this DC current. By passing the same modulation to the reference input of a lock-in amplifier (SCITEC # 410) and using the SA photodector signal as the input, an output is created that is a derivative of the SA signal. When the laser is exactly on resonance, the lock-in amplifier output will ideally be 0 volts. However, if the laser drifts above or below resonance, the respective output will be a positive or negative voltage. The output of the lock-in amplifier is routed through a home-built lock box. The lock box serves two purposes: the first is to act as a switch between the 4 Hz ramp and the lock-in amplifier output, and the second is to allows fine tuning of the central voltage and gain (amplitude) of the ramp. The output of the lock box goes directly to the piezo of the ECDL.

The lock-in amplifier is used to create a derivative of the SA signal, and is described in Appendix B. The SA signal and the resulting output of the lock-in amplifier is shown in Fig. 17. The lock box is used to reduce the gain of the ramp until a single transition is shown on the oscilloscope. At that point in time, the input of the lock box is switched so that the piezo voltage is controlled by the lock-in amplifier. Given the proper laboratory conditions, this lock loop can be stable for many hours at a time. A temperature feed back loop helps to stabilize the ECDL and extends the period over which the laser can be locked. Having a quiet, vibration free setting and an environment that does not drastically change temperatures is ideal. For this thesis, the MOT laser is locked to the $F = 2 \rightarrow F' = 2-3$ cross-over transition shown in the SA spectrum. The repumper laser is locked to the $F = 2 \rightarrow F' = 1 - 2$ cross-over transition. Through the use of AOMs, the frequency of each laser beam is controlled.

AOMs

Once the ECDLs are locked to a transition using saturated absorption spectroscopy, their frequencies are fine-tuned using accousto-optic modulators (AOMs). By rotating the AOM with respect to an incident laser beam, a $\pm 1^{st}$ order diffracted beam is created, as shown in Fig. 18. The frequency of the n^{th} order diffracted beam is offset from the incident laser beam by nf, where f is the frequency of the sound wave emitted by the transducer in the AOM. In a double pass setup, the diffracted beam is directed back through the AOM and the resulting diffracted beam's frequency shift is twice that of frequency of the AOM.

A combination of electronics from Mouser Electronics are used to drive the AOMs. The

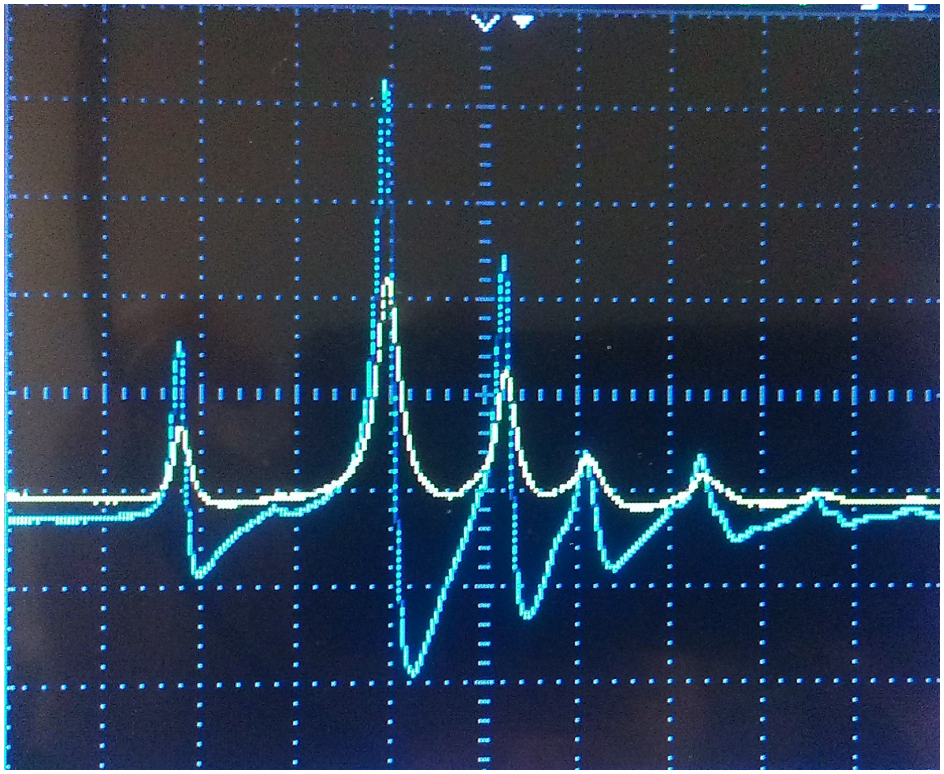

FIG. 17: The lock-in amplifier creates a derivative (blue) of the MOT SA signal (white).

circuitry for each AOM is shown in Fig. 19. Each AOM will run at a modulation frequency determined by a voltage controlled oscillator (VCO) (# ZOS-100 for the MOT, repumper, and probe AOMs, # ZOS-300 for both double pass AOMs). For an AOM that stays at one frequency, a voltage divider supplied with 12 V is used to tune the VCO to the desired frequency as observed on a frequency counter. For AOMs that are required to run at multiple frequencies during an experimental run, a digital level box supplies the voltage to the VCO. The digital level boxes are home-built power supplies that provide low noise TTL switchable voltages [41]. A variable voltage attenuator (# ZX73-2500) powered by a digital level box is attached to the VCO in the MOT and repumper circuits so that the intensity of the diffracted beams can be modified during the experimental procedure as well. Because the MOT, repumper, and probe AOMs also serve as optical switches to effectively turn off the laser beams during the experiment, a TTL triggered switch (# ZYSWA-2-50D) is used. A Shottky diode is used to reduce the ringing associated with the TTL signal reflecting back from the switch. Finally, the electrical signal passes through a radio-frequency (RF) amplifier before being sent to the AOM.

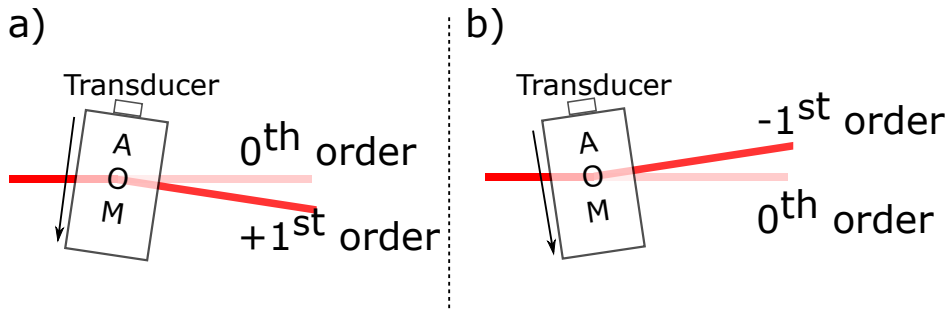

FIG. 18: An acousto-optic modulator (AOM) uses a sound wave emitted by a transducer (direction indicated by the arrow) to cause diffraction of a laser beam traveling through a crystal. a) By rotating the AOM w.r.t. the laser beam, a $+1^{st}$ order beam is created that is diffracted away from the transducer. b) Likewise, by rotating the AOM in the opposite direction, a -1^{st} order beam is created.

Each AOM serves to shift the frequency of the laser beam until it reaches a desired frequency for the experiment. The repumper laser, locked to the $F = 1 \rightarrow F' = 1 - 2$ cross-over transition, is passed through a single AOM (Gooch & Housego # R23080-1-LTD) set to a frequency of 78.5 MHz. Taking the $+1^{st}$ order beam results in the repumper laser beam being tuned directly to the $F = 1 \rightarrow F' = 2$ transition. The MOT laser has a comparatively more complex setup.

A double-pass AOM (Brimrose #EM200-50-780) setup- denoted as SADP AOM- is situated such that the frequency of the portion of the laser used in the SA is lower than that of the actual ECDL laser frequency. Another double-pass AOM (Brimrose #EM200-50-780) setup- denoted as DP AOM- is used so that the frequency of the laser beam after the setup is close to that of the laser beam in the SA. However, the DP AOM frequency can be changed with the use of a digital level box so that multiple frequencies can be achieved. The DFB laser frequency is the same as that of the laser beam after it passes through the DP AOM. A portion of the DFB laser beam is used as the probe and passes through a single AOM (NEOS 23080-1), while the rest of the DFB laser beam is used as the MOT laser beam and passes through its own AOM (Gooch & Housego # R23080-1-LTD). Locking to the $F = 2 \rightarrow F' = 2 - 3$ cross-over transition, which is $\sim$ 133.325 MHz below the desired $F = 2 \rightarrow F' = 3$ transition, the MOT and probe laser frequency detunings (with respect to the $F = 2 \rightarrow F' = 3$ transition) are as follows:

$$\delta_{MOT} = 2|DP| - 2|SADP| + |MOT| - 133.325MHz \tag{79}$$

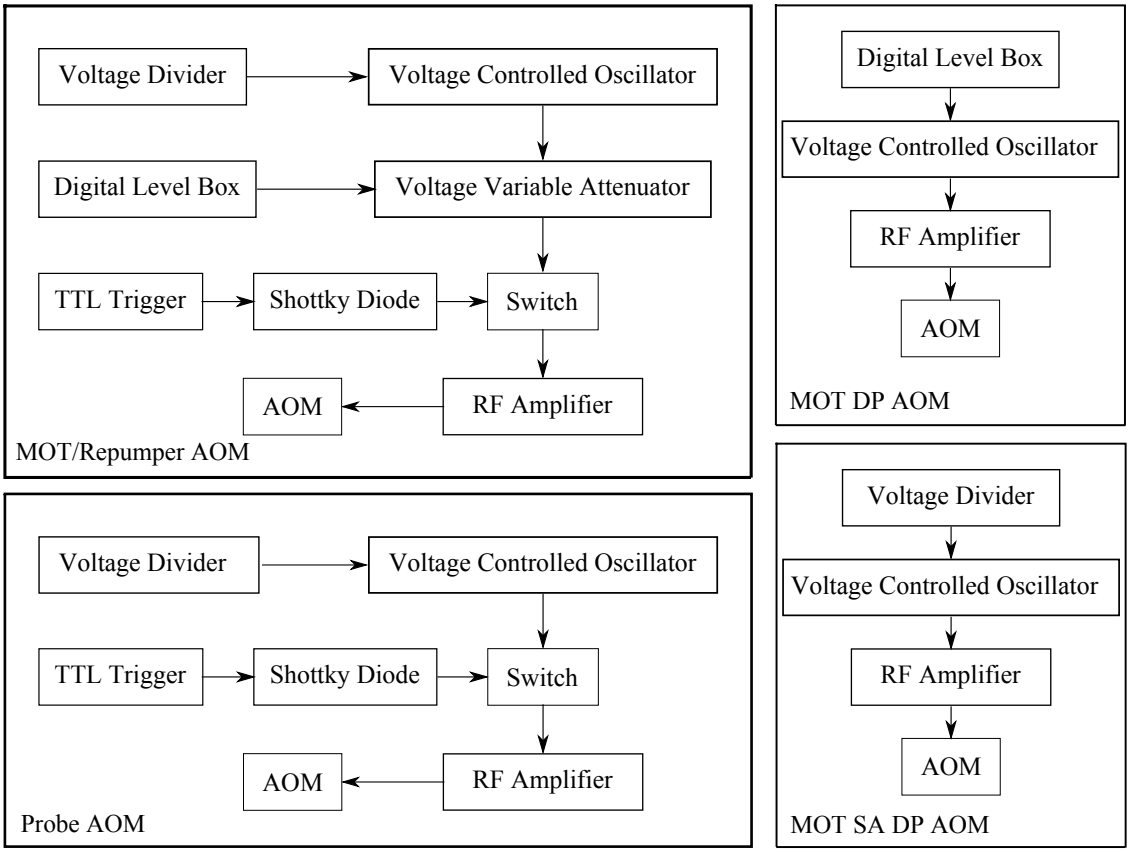

FIG. 19: Home-built AOM drivers are used to control the power and frequency of each AOM. Digital level boxes are used to switch between voltages during the experimental procedure; the frequency and intensity of the diffracted laser beam through each AOM can be changed by using voltage controlled oscillators and variable voltage attenuators.

$$\delta_{probe} = 2|DP| - 2|SADP| + |probe| - 133.325MHz \tag{80}$$

The SADP, MOT, and probe AOMs stay at their set frequencies of 225.16 MHz, 85 MHz, and 67 MHz respectively, while the DP is changed throughout the experimental process and can be tuned around 200 MHz over a range of $\sim$ 50 MHz. The advantage to the DP and SADP AOM setups is that the angular displacement of the laser beam on output does not change with frequency like it does in a single pass setup. Additionally, a larger range of frequencies can be achieved since the frequency of the AOM is effectively doubled. Finally, since both of the DP AOM setups are before the DFB slave laser, there are no intensity fluctuations from the frequency dependent efficiency of the AOM. Thus, the master-slave configuration creates laser beams with stable high intensities and the ability of the DFB to accept feedback allows it to easily follow the frequency changes of the DP AOM.

3.3 VACUUM CHAMBER

An ultrahigh vacuum is required to create and probe the atomic samples without having too much loss over the experimental run time due to background gas collisions. The vacuum chamber assembly used in this experiment, shown in Fig. 20, consists of 12 viewports, a 20 l/s ion pump, an electrical feedthrough attached to SAES rubidium getters, and a valve. A total of 8 viewports are 2-3/4" Del-Seal conflat flanges that have an antireflection (AR) coating for 780 nm. In addition, there is a pair of off-axis 2-1/8" non-AR coated viewports used for probing, and a pair of 4-1/2" windows AR coated for 1.064 μm light used for the fiber laser.

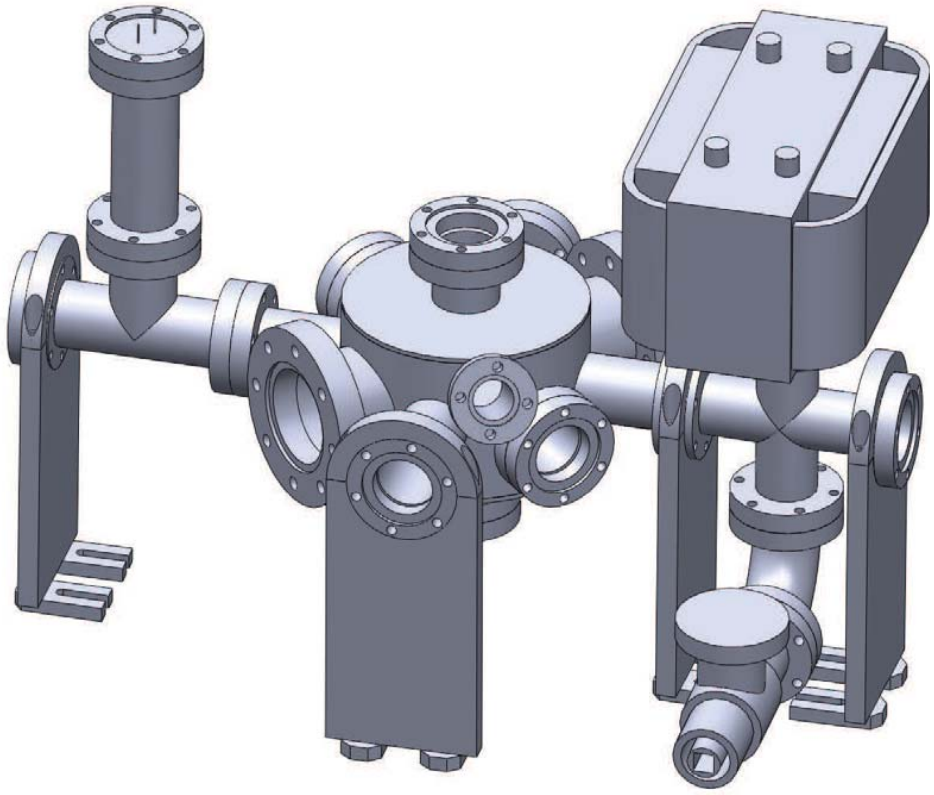

FIG. 20: The full vacuum chamber assembly includes the main chamber, an ion pump, valve, and getters attached to electrical feedthroughs. [41]

The SAES getters are doped with rubidium, which when heated will emit the atoms into the chamber. A total of 10 getters are available to use with the electrical feedthroughs; there are 3 setups that consist of two getters attached in series, and one setup uses 4 getters in series. A power supply is used to send up to 6 A of current through the getters. When they are first placed in the vacuum chamber, 6 A is supplied sequentially to each set of getters,

which bakes off any impurities. Once the vacuum chamber walls are coated with a thin layer of rubidium, the getter current is reduced to approximately 3 A. This creates a slow, steady flow of rubidium.

While the pressure guage on the Varian ion pump controller (# 921-0062) only has a sensitivity of 10^{-8} Torr, the current gauge can be used for calibration purposes. After replacing the SAES getters and running a high current through each set, the pressure inside of the vacuum chamber is relatively high- on the order of 10^{-6} Torr. While both the current and pressure gauges are readable, a pressure calibration curve (Fig. 21 can be made. Then, the current gauge can be used to find pressures below 10^{-8} Torr. For this specific controller, a measured current I (μA) corresponds to a pressure P (Torr)

$$P = 5.6(9) \cdot 10^{-9} e^{0.113(4)I}. \tag{81}$$

After a few months of constant pumping, the pressure in the vacuum chamber is reduced to $\sim 10^{-9}$ Torr.

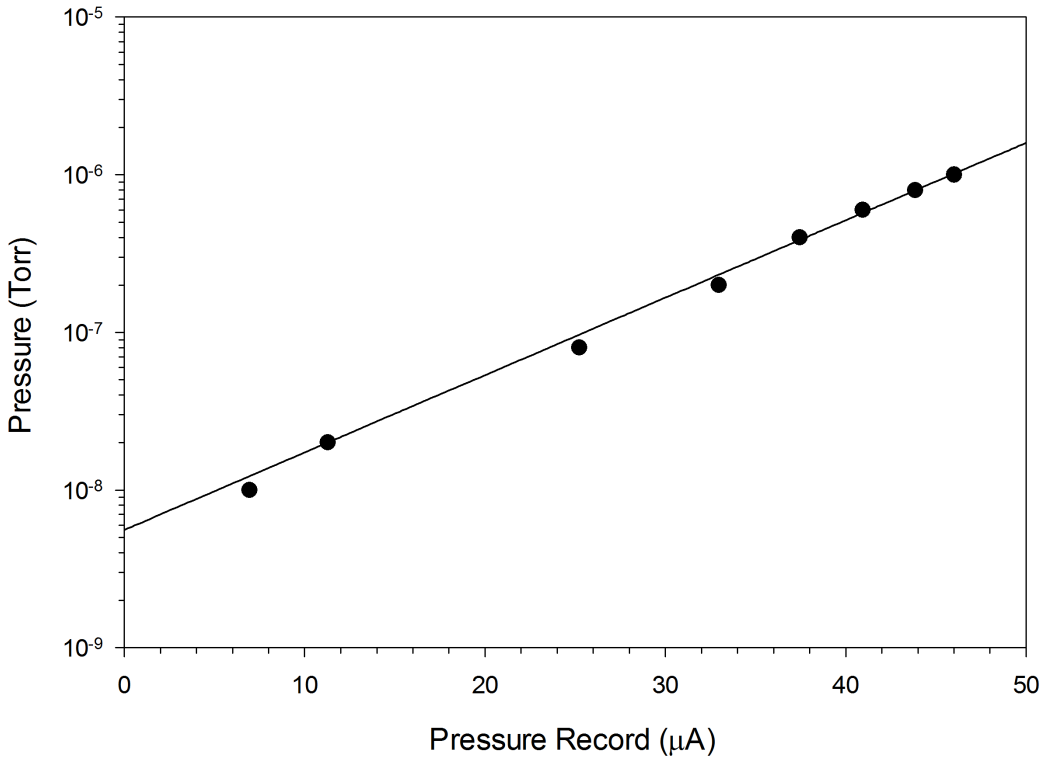

FIG. 21: A calibration curve between the current and pressure gauges on the ion pump controller is used to track pressures below 10^{-8} Torr. An exponential fit (line) is found for the data indicated by circles.

3.4 CONTROL SYSTEM

The sequencing and timing of the experimental process chiefly relies on use of the PCI-DIO-32-HS digital card from National Instruments. This card runs a LabView program that has the ability to output 12 independent TTL pulses to control various devices. A matrix of 0's and 1's determine if a "LOW" or "HIGH" signal is sent. Each column is a different output channel, while the time for each event is included for each row. Due to the available memory in our computer, this program is limited to 10 μs precision. The AOM switches and the digital level boxes used to change VCO frequencies and VVA intensities relies on this program. Additional outputs are used to open and close shutters, turn the fiber laser on and off, and trigger data collection devices. By using one output to trigger another pulse generator (Quantum Composer (QC) #9614), an additional 4 channels can be used. The QC has a resolution of 10 ns, which allows for finer time control.

During fluorescence imaging, a liquid nitrogen (LN_2) cooled charge coupled device (CCD) camera (Princeton Instruments # LN/CCD-TKM512) is used to acquire images. The National Instruments card is used to trigger the camera, and WinView is used to collect the images. Time-dependent measurements use a photomultiplier tube (PMT) (Hamamatsu #R9110) running at its maximum voltage of 1250 V. The output of the PMT is connected to a multichannel scaler (MCS) (SRS # SR430). In both experimental procedures, care must be taken not to saturate the imaging devices. If saturated by room light, the LN_2 CCD requires several exposures to recover, while the PMT can take weeks to fully recover. While this may be cause for concern, the sensitivity to light is advantageous for low-saturation imaging.

3.5 LASER TRAPPING AND COOLING

Cold atomic samples are advantageous when studying fundamental scattering processes; the reduction of the temperature dependent Doppler broadening and the corresponding increase in the decoherence time of the sample allows for collective and cooperative scattering to be observed. In order to have a sample with a relatively high density (on the order of 10^{13} atoms/cm^3), we begin first by creating a magneto optical trap (MOT). One of the most widely used atomic traps, a MOT uses a combination of optical and magnetic fields. Through the exploitation of atomic transition selection rules, photons exchange momentum with a thermal distribution of atoms and effectively cool an ensemble by reducing its mean velocity. Creating a spatial dependence to this scattering process traps the cooled atoms to

create the MOT. A small percentage of the atoms trapped in the spatially larger MOT, with a density on the order of 10^9 atoms/cm^3, are transferred into far off resonance optical dipole trap (FORT.) With temperatures near 100 μK, the atoms within the FORT are practically stationary over the course of the measurements. When the FORT trapping laser is turned off, the atoms are able to be measured in free-space, without the influences of external magnetic or optical fields. The following sections will cover the theory and experimental setup for both the MOT and the FORT.

3.5.1 MAGNETO OPTICAL TRAP (MOT)

Theory

A single atom initially in an excited state that spontaneously emits a photon will experience a radiative force

$$\overrightarrow{F} = \hbar \overrightarrow{k} \gamma \rho_{11}, \tag{82}$$

with $\overrightarrow{k} = \frac{2\pi}{\lambda}\hat{k}$ being the wave number of the photon with wavelength λ initially traveling in a direction $\hat{k}$, γ is the decay rate of the excited state, and ρ_{11} is the excited state amplitude of the atom as given by Eq. 35 [52]. An atom that has a velocity $\overrightarrow{v}$ will observe a Doppler shift of the laser frequency, $\omega_D = -\overrightarrow{k} \cdot \overrightarrow{v}$, and the net force for an atom will thus reduce to

$$\overrightarrow{F} = \frac{\hbar \overrightarrow{k} \gamma}{2} \frac{s_0}{1 + s_0 + (2(\delta - \omega_D)/\gamma)^2}, \tag{83}$$

where δ is the laser's detuning from resonance and s_0 is the on-resonance saturation parameter. By including two counter-propagating laser beams, the sum of the forces results in a velocity-dependent net force of

$$\overrightarrow{F} \cong -\beta \overrightarrow{v}, \tag{84}$$

$$\beta = \frac{8\hbar k^2 \delta s_0}{\gamma \left(1 + s_0 + (2\delta/\gamma)^2\right)^2}. \tag{85}$$

Atoms that travel towards a red-detuned laser beam ($\delta < 0$) will experience a force that causes a deceleration. By counter-propagating two laser beams, an atom's velocity along that axis will be reduced by the radiative force no matter which direction it travels. By aligning three orthogonal pairs of counter-propagating laser beams, an optical molasses can be created. The atoms are cooled, meaning their average velocity has been reduced, but there is no restoring force to spatially confine atoms within the laser beams' paths. This results in an optical molasses, in which the atoms are cooled while within the laser beams'

paths but are free to escape the sample.

When a current I flows through a wire formed into a loop of radius R with N turns, the resulting magnetic field along the axis of symmetry can be found using the Biot-Savart Law. Assuming the magnetic field is directed along the z axis, we have

$$B_z = \frac{\mu_0}{2} \frac{NR^2 I}{\left(z^2 + R^2\right)^{3/2}}, \tag{86}$$

where z is the distance from the center of the loop, and the permeability of free space is μ_0. Orienting another coil a distance h away and directing the current to flow in the opposite direction creates what is known as an anti-Helmholtz configuration. The resulting magnetic field near the middle of the configuration ($h/2$ below the upper coil and $h/2$ above the lower coil) can be well described for small z by

$$B(z) = B_0 z, \tag{87}$$

where z is now the distance from the center of the two coils, and the strength of the magnetic field is

$$B_0 = \frac{\mu_0 N R^2 I}{2}. \tag{88}$$

When this magnetic field is applied, the energy levels of the atoms experience a spatially dependent Zeeman shift. With weak magnetic fields (below the strong-field Paschen-Back limit), the energy splitting for a given magnetic quantum number m_F for an isolated transition is

$$\Delta E = \mu_B g_F m_F B, \tag{89}$$

where the Bohr magneton is $\mu_B = \frac{e\hbar}{2m_e}$ and g_F is the hyperfine Landé g-factor.

$$g_F = \left(1 + \frac{J(J+1) + S(S+1) - L(L+1)}{2J(J+1)}\right)\left(\frac{F(F+1) + J(J+1) - I(I+1)}{2F(F+1)}\right) \tag{90}$$

As shown in Fig. 22, atoms with $m_F < 0$ will have their energies shifted below bare resonance when $z > 0$. In contrast, atoms with $m_F > 0$ will experience a negative Zeeman shift when their position is negative. We can take advantage of these energy splittings to force an atom to selectively interact with only the laser beam with which it is counter-propagating.

A MOT uses a laser with frequency ω_L close to a bare resonant frequency ω_0 such that $\delta = \omega_L - \omega_0$ is negative. Transitions with $\Delta m_F = \pm 1$ are detuned by $\pm\delta_\pm$ from the laser beam. An atom positioned at $z < 0$ would be more likely to scatter light that excites

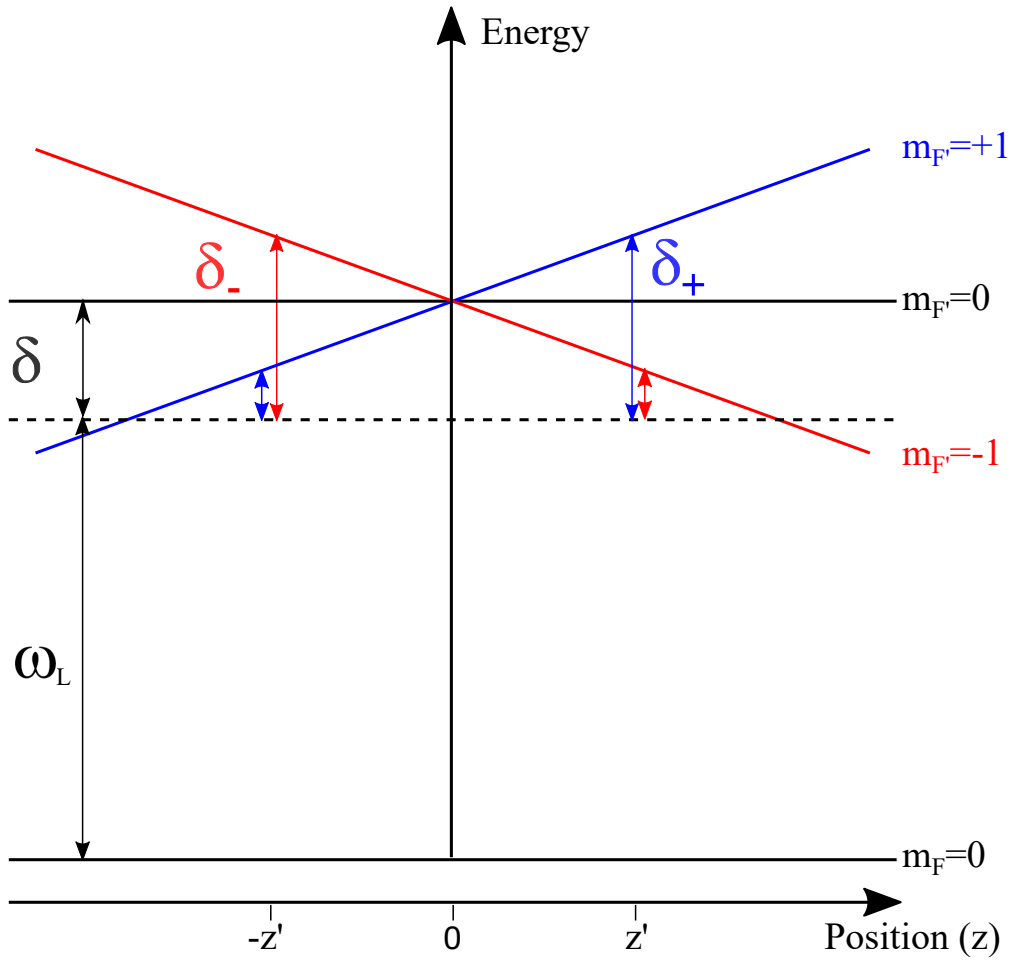

FIG. 22: Applying a magnetic field $B = B_0 z$ creates a position dependent Zeeman shift. A laser with frequency ω_L and detuning δ from the $m_F = 0 \rightarrow m_{F'} = 0$ transition is applied. The detuning δ_+ from the $m_F = 0 \rightarrow m_{F'} = +1$ transition (indicated in blue) is less than the detuning δ_- from the $m_F = 0 \rightarrow m_{F'} = -1$ transition (indicated in red) when atoms are at $z = -z'$. For $z = z'$, $\delta_- < \delta_+$.

transitions of $\Delta m_F = +1$, because $\delta_+ < \delta_-$. Likewise, at atom positioned at $z > 0$ would have a higher probability to scatter light that can excite $\Delta m_F = -1$ transitions. By aligning a σ_+ (right circularly polarized) laser beam that points from $-z$ to $+z$ and a σ_- (left circularly polarized) laser beam that points from $+z$ to $-z$, atoms selectively interact such that they are cooled and trapped around $B = 0$.

MOT Loading

The ^{87}Rb MOT relies on both the MOT and repumper lasers. The MOT laser is detuned -3γ from the $F = 2 \rightarrow F' = 3$ transition, where $\gamma = 6$ MHz is the natural decay rate of ^{87}Rb, and this laser is used to trap the atoms. However, because there is a non-zero probability of being excited to the $F' = 2$ state, some atoms are optically pumped to the $F = 1$ ground state. To combat this loss, the repumper laser, tuned to the $F = 1 \rightarrow F' = 2$ transition, optically pumps atoms back into the $F = 2$ ground state. As shown in Fig. 23, the MOT and repumper lasers are combined using a polarizing beam splitter cube. The polarization of the laser beams is fixed using a half-wave ($\lambda/2$) plate such that 1/3 of the intensity is passed through to one arm of the chamber, while the remaining intensity is split equally into two more arms. Each arm passes through a quarter-wave ($\lambda/4$) plate, which transforms the laser beam from linear polarization to circular polarization. After passing through the vacuum chamber, another $\lambda/4$ plate is present, followed by a mirror. Upon entering the vacuum chamber, the retro-reflected laser beam will have the opposite circular polarization of the incoming beam.

After exiting the polarization preserving fiber, the MOT laser beam has a power of approximately 25 mW. Meanwhile, the repumper only has about 4 mW upon exit from the non-polarization preserving fiber. Each laser beam is focused through a shutter (Uniblitz # LS6Z2) before being collimated to a beam waist of $\sim$1.3 cm. The shutters are necessary for two reasons. First, the AOMs cool off, and thus their efficiency changes, if they are left off for too long. The shutters can then be used to block laser light that is not needed while keeping the AOMs warm. Secondly, even if the AOMs are off, there is still residual leakage due to electrical noise amplified by the RF amplifier being passed to the AOM. After the beam splitter cubes, the laser beams are aligned with the center of the vacuum chamber viewports so that they will intersect at the middle of the chamber. We are able to retroreflect each laser beam all the way back to the optical fiber. However, to avoid standing waves in the MOT, the final arrangement requires a minor misalignment.

The magnetic quadrupole field is created by running 10 A of current through the anti-Helmholtz coils mounted in the z (vertical) direction. This creates a field gradient about the center of the vacuum chamber. However, residual magnetic fields due to external sources must be combatted. Additional trim coils are mounted on the three viewports for the initial inputs of the laser beams. This way, a small magnetic field can be created that cancels out stray fields in all three directions. A Sanyo video camera is used to see the MOT on a TV monitor. When the magnetic field is switched off, an optical molasses is formed. The

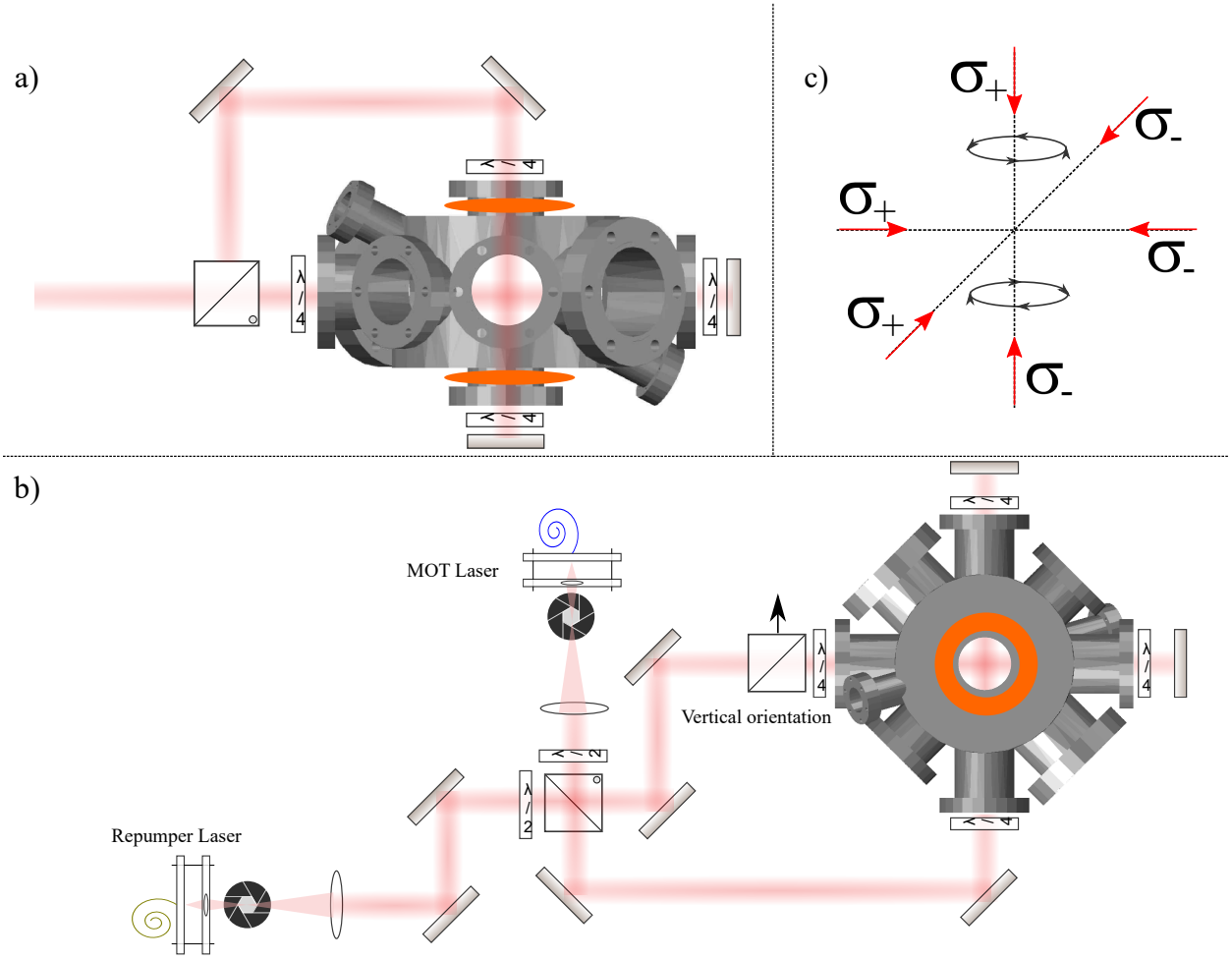

FIG. 23: The a)side and b)top views of the optical setup for creating a MOT are shown. c)The polarization of each laser beam and the direction of the current in the magnetic coils is shown in the schematic. Additional trim coils mounted outside of the vacuum chamber windows with σ_+ laser beam inputs, used to fully cancel out extraneous magnetic fields, are not shown.

trim coils are adjusted until the molasses expands freely and equally in all directions. The molasses can be seen using an infrared (IR) viewer as well, but the video camera is beneficial in being able to magnify the image. The MOT is visible to the naked eye and appears to glow red as it scatters the MOT and repumper laser beams.

3.5.2 FAR OFF RESONANCE OPTICAL DIPOLE TRAP (FORT)

Theory

One of the simplest optical dipole traps consists of one single-mode focused Gaussian laser beam. The intensity profile (in cylindrical units) of a laser beam with wavelength λ that is tightly focused with peak intensity I_0 at $r = z = 0$ is well characterized by

$$I(r,z) = I_0 \frac{\exp\left(-2r^2/(w(z))^2\right)}{1+(z/z_R)^2}, \tag{91}$$

with a beam waist radius of w_*, $w(z) = w_*\sqrt{1+(z/z_R)^2}$, and a Rayleigh range of

$$z_r = \frac{\pi w_*^2}{\lambda}. \tag{92}$$

The spatially dependent trap potential, with depth U_0, is given by

$$U(r,z) = U_0 I(r,z)/I_0. \tag{93}$$

The potential well creates a trap in which atoms are able to be loaded and contained.

For an alkali atom, the depth is determined by the detunings $\delta_{1/2}$ and $\delta_{3/2}$ from the respective D1 and D2 resonances [68]. For a linearly polarized laser beam, the trap depth is

$$U_0 = \frac{\hbar\gamma I_0}{24 I_s}\left(\frac{1}{\delta_{1/2}} + \frac{2}{\delta_{3/2}}\right). \tag{94}$$

For a far off resonance trap, $\delta_{1/2}$ and $\delta_{3/2}$ are on the order of 100 THz. The ground and excited state hyperfine splittings are negligible in this case, as they are smaller by a factor of approximately 6.8×10^{-5} and 5×10^{-6} respectively.

The trap potential can also be defined by the polarizability α of the atoms, which is related to the dipole moment: $\vec{p} = \alpha\vec{E}$. For a laser beam with frequency ω detuned from a

resonant frequency ω_0, the complex dipole polarizability is

$$\alpha = 6\pi\epsilon_0 c^3 \frac{\gamma/\omega_0^2}{\omega_0^2 - \omega^2 - i(\omega^3/\omega_0^2)\gamma}. \tag{95}$$

The potential depth of the trap is then

$$U_0 = \frac{\alpha_0 P}{\pi\epsilon_0 c\omega_0^2}. \tag{96}$$

Here P is the total power of the laser beam related to the intensity $I = \frac{2P}{\pi w_*^2}$ and the static polarizability is α_0. At the wavelength of the laser used in this experiment (1.064 μm), α_0 of ^{87}Rb is

$$\alpha_0 \approx 711 \cdot 4\pi\epsilon_0 a_0^3 \tag{97}$$

where a_0 is the Bohr radius [69].

Atoms are loaded from the MOT into the FORT. Scattering from the MOT trapping beam tuned near the $F = 2 \rightarrow F' = 3$ transition, the ^{87}Rb atoms decay via inelastic Raman and elastic Rayleigh scattering to the $F = 1$ and $F = 2$ ground states respectively. Extinguishing the repumper laser at the end of the loading period ensures that most of the atoms are held in the lower energy potential well of the $F = 1$ ground state.

While the trap depth scales as I_0/δ, the scattering rate γ_s decreases at a faster rate $\propto I_0/\delta^2$,

$$\gamma_s(r,z) = \frac{\pi c^2\gamma^2}{2\hbar\omega_0^3}\left(\frac{1}{\delta_{1/2}^2} + \frac{2}{\delta_{3/2}^2}\right) I(r,z). \tag{98}$$

By increasing the detuning and the intensity of the laser at a linear rate, a constant trap depth can be maintained. However, the scattering rate is greatly reduced. By creating a far off resonance optical dipole trap (FORT) and reducing this heating mechanism, atoms are able to be trapped with lifetimes beyond one second [70–72].

FORT Loading

To create the FORT, a single-mode fiber laser (IPG Photonics # YLR-30-1064-LP) with a wavelength of 1.064 μm is aligned such that the focal point is overlapped near the center of the MOT, as shown in Fig. 24. Atoms within the MOT excited by the MOT laser undergo inelastic Raman scattering to decay into the $F = 1$ ground state. The light shift caused by the focused fiber laser creates a potential well that traps these atoms. The efficiency of this process depends on many factors, which will be explained in further detail below. Through

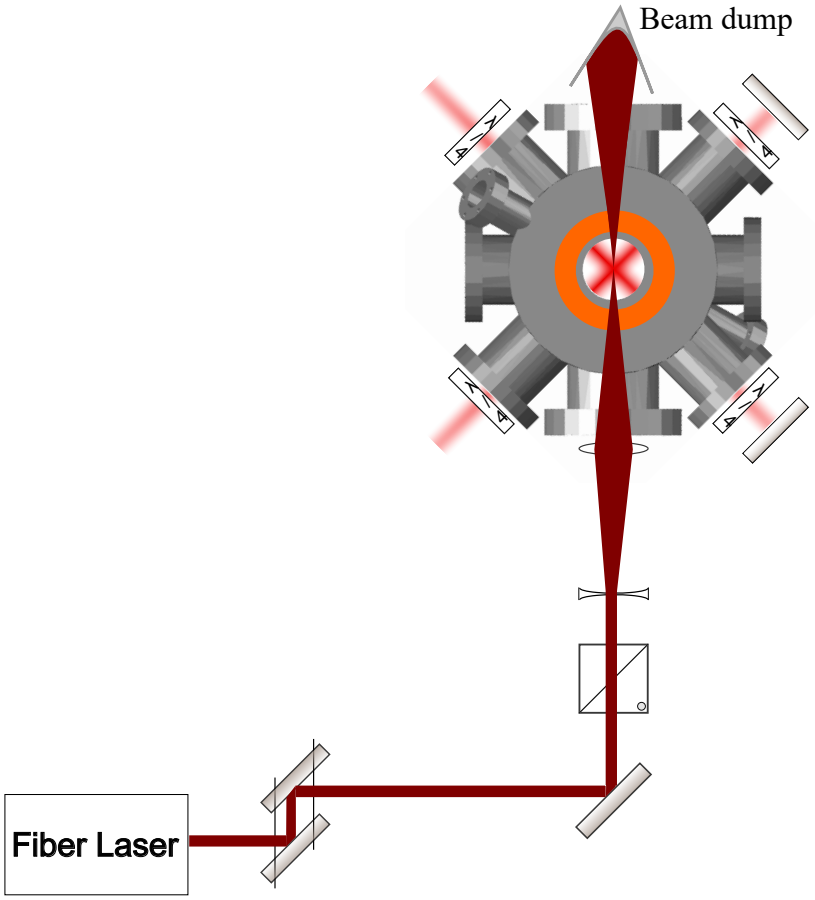

FIG. 24: The optical layout for the fiber laser is shown. Tightly focused, the laser beam is overlapped near the MOT to transfer atoms into the FORT.

several iterations of optimization, we are able to achieve a local maximum in the number of atoms loaded from the MOT into the FORT.

The basic timing for FORT loading is shown in Fig. 25. Before the fiber laser is turned on, the MOT is formed and held until the MOT reaches a plateau in the number of atoms, which takes a few seconds. The fiber laser is turned on, and atoms begin to load into the FORT. The MOT laser intensity is reduced to approximately 20 mW, while the repumper laser intensity is drastically diminished to approximately 10 μW. Additionally, the DP AOM frequency is changed so that the MOT detuning changes from -3γ to $\sim$-6.5γ. Through this process, the radiation pressure on the MOT is reduced; a compressed MOT, shown in Fig. 26, is formed that has better spatial overlap with the fiber laser beam. At the end of the loading process, the repumper laser is fully extinguished to ensure that the atoms are being loaded into the $F = 1$ ground state. After about 5 ms, only the fiber laser is kept on, and

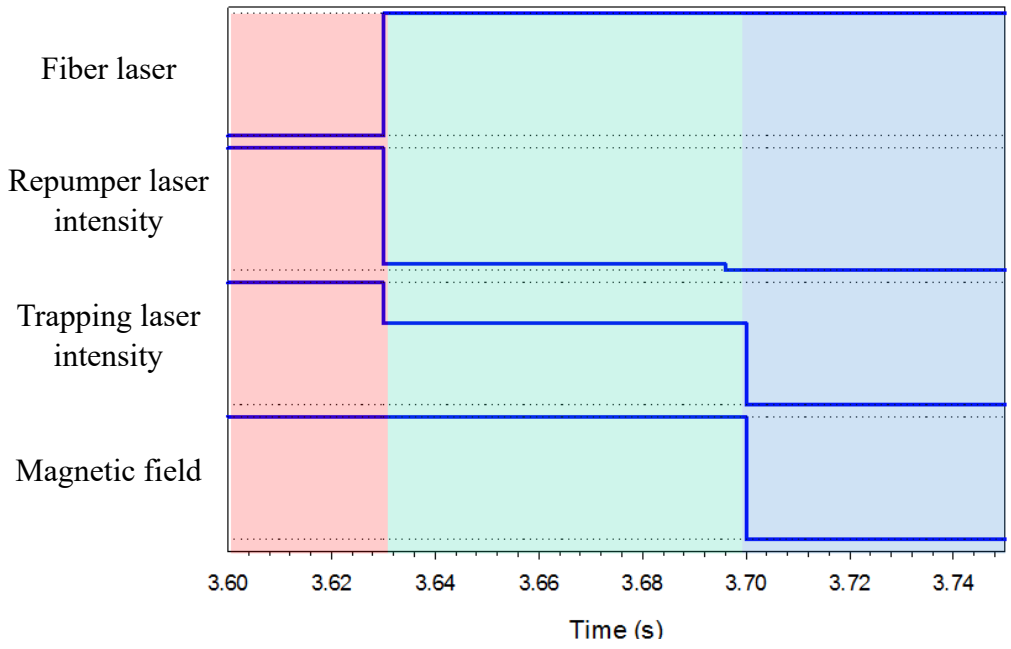

FIG. 25: A timing diagram during the FORT loading process is shown. Before the fiber laser is turned on (red section), the MOT is being held with the trapping and repumper lasers. During loading (green section), the trapping and repumper laser intensities are reduced, and the fiber laser is turned on. The repumper is extinguished to allow the atoms to be trapped in the $F = 1$ ground state, and then everything except the fiber laser is turned off (blue section).

the atoms are held in the FORT.

The initial alignment of the fiber laser is the most difficult task in creating the FORT. The optics for the fiber laser are coated for 1.064 μm, while fluorescence from the MOT is 780 nm. Additionally, the guide beam equipped with the fiber laser is a HeNe laser that lases around 600-700 nm. The guide beam is not easily visible to the naked eye after the mirrors, and is not visible using the IR viewer, whereas the fiber laser is only visible by use of an IR viewer (or by catching paper on fire, which is not recommended.) The following strategy involves translating an image of the MOT from the vacuum chamber to the output of the fiber laser to ensure good overlap between the FORT and MOT.

Begin by roughly aligning the guide beam so that it goes through the middle of the window in the vacuum chamber. Place the positive lens ($f = 10$ cm) near the window and find the image of the MOT formed on the opposite side of the lens. Align the guide beam with this image. Place a temporary lens on the opposite side of the vacuum chamber and repeat the process, so that the guidebeam is now going through both images of the MOT.

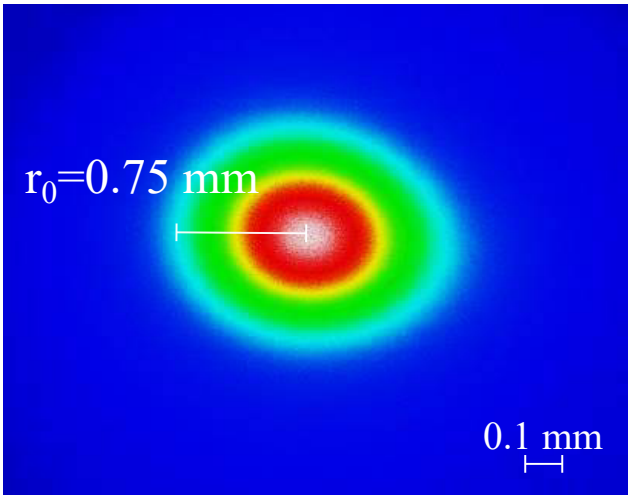

FIG. 26: A false-color image of the compressed MOT from a CCD camera is shown. The 25 μK spherical Gaussian sample has approximately 50 million atoms.

This ensures proper alignment of the fiber laser with the atomic sample. To align the focal point, a negative lens ($f = 10$ cm) is added between the mirror and the positive lens so that the MOT fluorescence appears to be collimated. Vertical and horizontal positioning of the negative lens can be used to guide this fluorescence to the output coupler of the fiber laser. The addition of a polarizing beam splitter cube maintains the linear polarization of the fiber laser. This alignment should be good enough to trap enough atoms in the FORT to begin the optimization process.

The MOT and repumper lasers are flashed at the original intensities and detunings after a hold time of 200 ms, and the fluorescence of the FORT is either captured on a CCD or monitored using a PMT connected to an oscilloscope (see Fig. 27.) During optimization, the goal is to increase the peak number of counts on the CCD or the maximum voltage on the oscilloscope. The advantage is that the adjustments can be made in real time and the effects on the number of atoms are clearly apparent. First, the repumper intensity during MOT compression is adjusted, followed by the MOT DP AOM frequency. While only a minor change is visible, the MOT laser intensity is then adjusted. Finally, the alignment of the fiber laser focal point is adjusted. The associated lenses are mounted in z-translating post holders, on a translation stage atop a rail that allows for focal point adjustments. After the laser alignment is optimized, the power of the fiber laser is adjusted and the process is repeated again. The LabView program timing diagram is also adjusted to change the loading time period and time that then repumper laser is off before loading is complete. The first

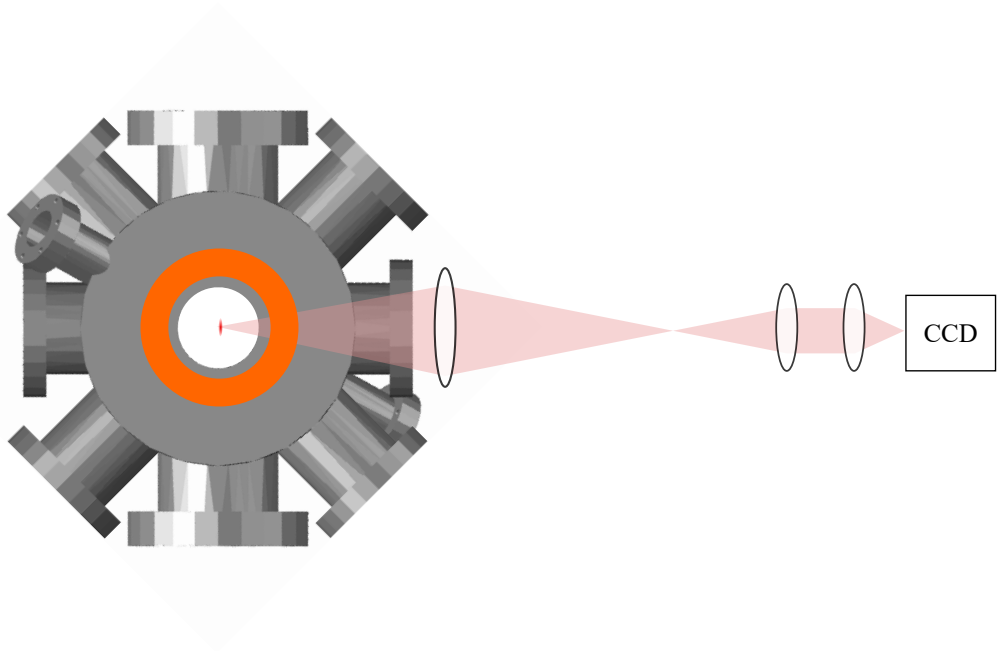

FIG. 27: Fluorescence from the FORT is collected perpendicular to the fiber laser. A collection lens ($f = 75$ mm), in a 2f-2f configuration at the viewport, is used in combination with two $f = 60$ mm lenses to create an image with unit magnification at the CCD. A multi-mode optical fiber can also be placed at the focus to collect light for a PMT.

optimized FORT achieved in this lab is shown in Fig. 28.

After imaging the first FORT, we realized that the sample was too extended to create a high-density sample. To create a sharper focus (and thereby a shorter Rayleigh range), the positive lens is moved as close to the window as possible and the position of the negative lens is adjusted to focus the laser beam to the middle of the chamber. After several more iterations of optimization, the fluorescence signals reach a steady state and the number of atoms reaches a local maximum. The resulting FORT is shown in Fig. 29. After any optimization process, the FORT sample must be fully characterized.

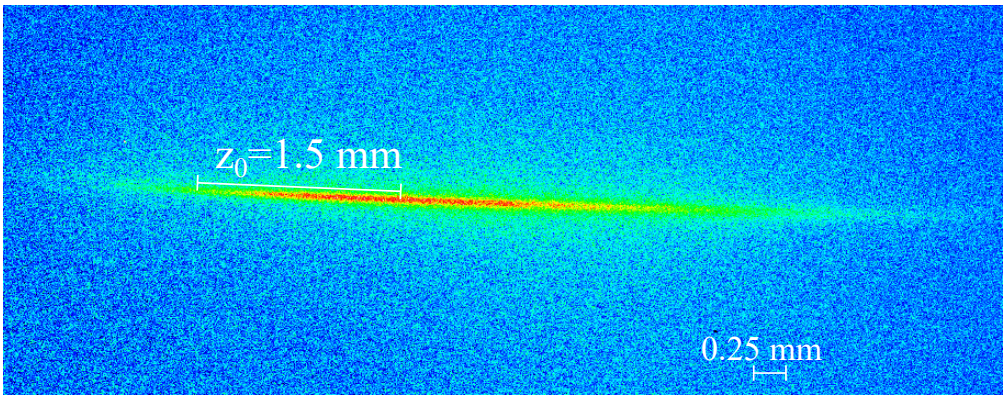

FIG. 28: This is a CCD (13 μm x 13 μm pixels) false-color image of the first FORT created in this lab after a round of optimization. It is tilted because the camera was not level at the time, but was corrected shortly after taking the image. The length of this sample does not suffice for a high density trap. The positive lens must be closer to the chamber, which would result in a tighter focus and shorter Rayleigh range.

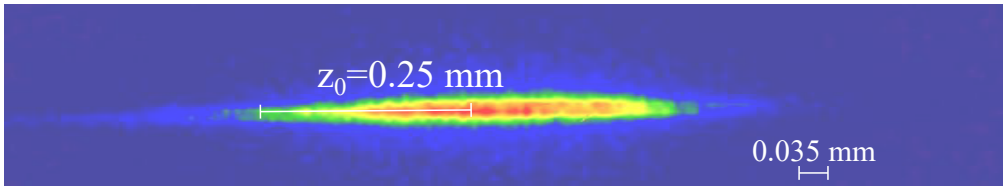

FIG. 29: After reoptimization with a tighter fiber laser beam waist, the FORT axial length is reduced.

3.6 SAMPLE CHARACTERIZATION

In this section, numerous methods utilized to fully characterize the FORT are explained. In order to measure the number of atoms in the FORT, we first measure the number of atoms in the MOT using two separate methods which yield consistent results. Then fluorescence imaging shows the transfer efficiency from the MOT to the FORT. By allowing the FORT to undergo ballistic expansion in free space, the temperature can be measured by tracking the rate of expansion of the radii with time. Finally, in order to ascertain the spatial size of the FORT, parametric resonance measurements are performed. A summary of the samples' characteristics is provided on page 64.

3.6.1 NUMBER OF ATOMS

It is important to know the number of atoms within the FORT with high confidence. However, its reduced spatial size and number of atoms compared to the MOT makes the following methods difficult to implement. Therefore, we perform absorption imaging and observe optical pumping in the time domain to ascertain the number of atoms in the MOT. Then, a fluorescence image of the MOT is taken. The number of atoms is proportional to the number of counts observed on the CCD, which gives a conversion for counts/atom. This ratio can then be applied to a fluorescence image of the FORT to find the number of atoms in the experimental atomic sample. Note that for fluorescence imaging, the atomic samples are allowed to expand so they are not optically thick.

Absorption Imaging

The first method for determining the number of atoms in the MOT is known as absorption imaging. We begin with atoms in a MOT with a density distribution $n(r)$ with a peak density n_0 and radius r_0 described by the equation

$$n(r) = n_0 \exp\left(-\frac{r^2}{2r_0^2}\right) \tag{99}$$

and a near-resonance beam with intensity I_0 is incident on the sample. From Beer's Law, the transmitted light through the sample is simply

$$I_T = I_0 e^{-b}, \tag{100}$$

with b being the optical depth. Substitution of Eq. (99) into Eq. (56) gives the optical depth for the MOT;

$$b(r,\delta) = \sqrt{2\pi} n(r) r_0 \sigma(\delta). \tag{101}$$

As stated previously, the frequency dependent cross section is

$$\sigma(\delta) = \frac{\sigma_0}{1 + \left(\frac{2\delta}{\gamma}\right)^2} \tag{102}$$

with a laser detuning δ from the $F = 2 \rightarrow F' = 3$ resonance and $\gamma = 2\pi \times 6.1 MHz$ is the natural resonance width of the probed transition. The peak scattering cross section for this transition with wavelength $\lambda = 780.24$ nm is

$$\sigma_0 = \frac{2F'+1}{2F+1}\frac{\lambda^2}{2\pi}. \tag{103}$$

As shown in Fig. 30, a CCD camera takes an image of a probe. Then, a transmission image is taken, in which the MOT absorbs some of the light of the probe. The ratio of these two images yields an absorption image,

$$\frac{I_T(r,\delta)}{I_0} = \exp\left(-b(r,\delta)\right). \tag{104}$$

A vertical and horizontal cross section is taken of each absorption image. The on-resonance horizontal cross section for an expanded MOT is shown in Fig. 31. Taking the negative of the natural logarithm of the cross section yields the spatially dependent optical depth of the sample. This can easily be fit to a Gaussian curve, with the amplitude equal to the optical depth $b(0,\delta)$ through the center and the $1/e^2$ radius giving r_0 of the sample. Absorption images are taken over a range of detunings, the results of which are shown in Fig. 32. A fit to the optical depth at each detuning provides the peak optical depth $b_0 = b(0,0)$ and the resonance width γ.

Integrating Eq. (99), we find that the total number of atoms in the MOT is

$$N_{MOT} = (2\pi)^{3/2} n_0 \, r_0^3 \tag{105}$$

Using an on-resonance probe ($\delta = 0$), substitution of Eqs. (101) and (102) into Eq. (105) yields

$$N = \sqrt{4\pi}\frac{r_0^2 \, b_0}{\sigma_0}. \tag{106}$$

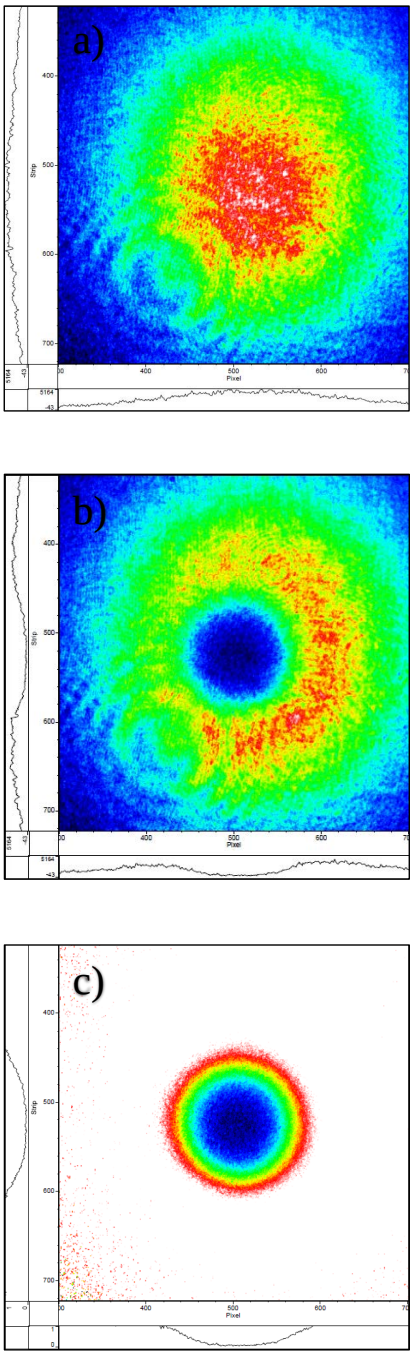

FIG. 30: Absorption imaging of a MOT requires an image of a) the probe by itself and b) the absorption of the probe by the MOT. c) The division of image (b) by image (a) provides the absorption profile of the atomic sample. A fit to the natural log of this image reveals the spatially dependent optical depth of the MOT.

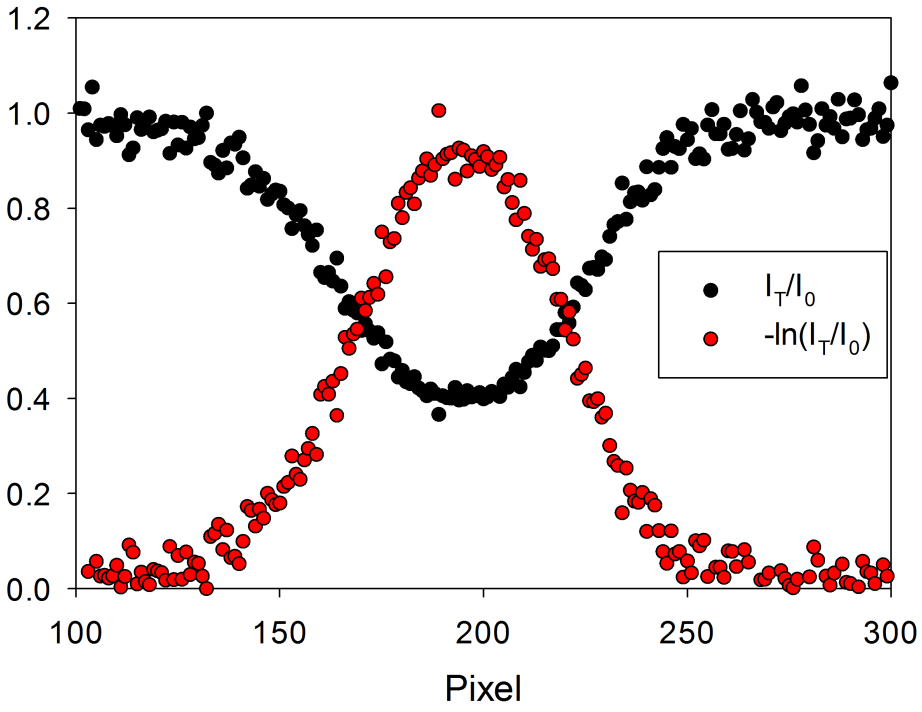

FIG. 31: An absorption image of the MOT is taken after it is allowed to expand. The horizontal cross section is shown in black. The optical depth $b(r, \delta) = -\ln(I_T/I_0)$ across the sample is shown in red. A fit yields $b(0, \delta)$ and the radius of the sample r_0.

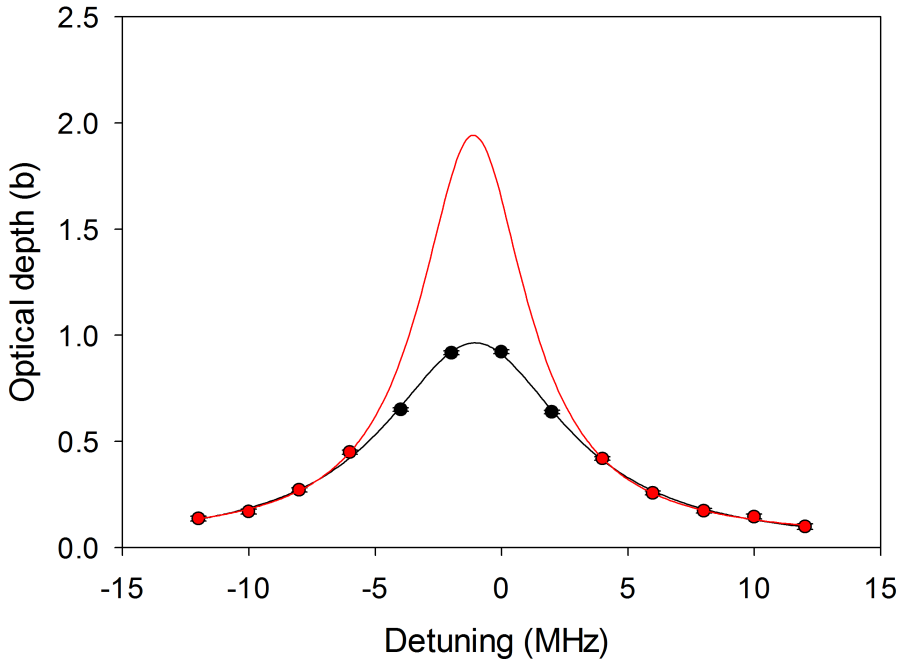

FIG. 32: Experimental results of the optical depth through the center of the expanded MOT are plotted for various detunings. A Lorentzian fit gives b_0 and γ. The fit to all data is in black, while the fit in red omits detunings near resonance.

The main issue with using absorption imaging is that the optical depth spectrum deviates from a Lorentzian line shape when b is greater than 1. Allowing the sample to expand helps alleviate this issue. In addition, one can omit experimental data near $\delta = 0$ where the optical depth is highest. As shown in 32, fits with (black) and without (red) the central points are shown. Including all points results in $b_0 = 0.96(1)$ and $\gamma = 8.7(2)$ MHz. Removal of the central points reduces γ to 5.2 MHz, with a standard error of 1.4 MHz. Using this fit, the peak optical depth is 2.6(7). To combat the uncertainty in the actual value of the optical depth- and hence the number of atoms in the MOT- another method is used in conjunction with absorption imaging.

Optical Pumping

A second method is used for directly measuring the number of atoms in the MOT. Instead of probing the $F = 2 \rightarrow F' = 3$ transition, the probe laser beam is tuned to the $F = 2 \rightarrow F' = 2$ transition. Atoms excited by the probe are no longer on a closed transition, but are able to decay to either $F = 1$ or $F = 2$ with equal probability $p = 1/2$ [52, 73, 74]. The expectation value $\langle N_p \rangle$ for the number of photons an atom absorbs before decaying to

the $F = 1$ ground state is given by the sum

$$\langle N_p \rangle = \sum_{n=1}^{\infty} n(1-p)^{n-1}p = \frac{1}{p}. \tag{107}$$

Thus, for a probe tuned to the $F = 2 \rightarrow F' = 2$ transition, an average of 2 photons will be absorbed per atom. By measuring the reduction in the probe intensity, the number of atoms in the MOT can be measured.

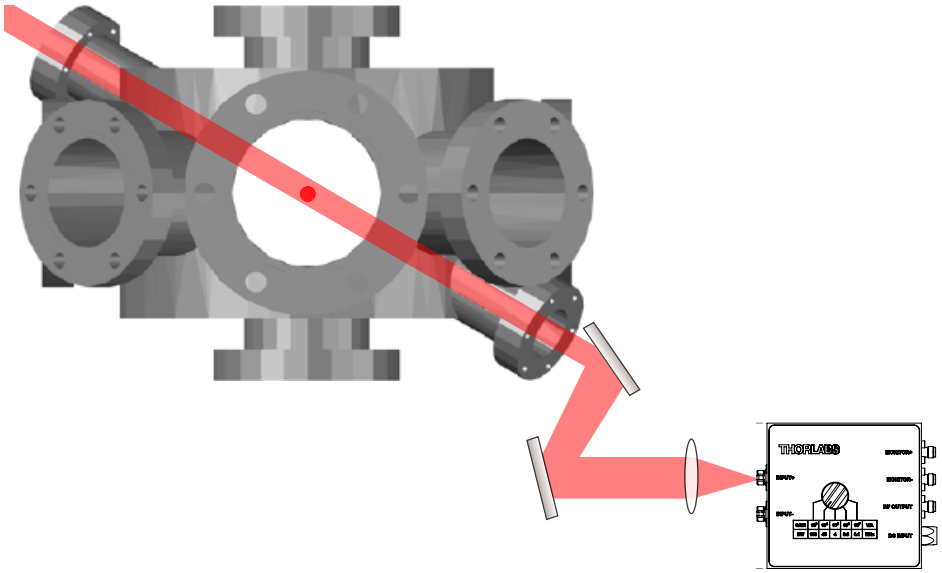

FIG. 33: The transmitted intensity of a probe tuned to the $F = 2 \rightarrow F' = 2$ transition is measured in the time domain using a photodetector. When atoms are present, the light will be absorbed at rate of 2 photons/atom.

The optical layout for measuring the forward transmission of the probe is shown in Fig. 33. First, the power of the probe is measured using a power meter. Then, the probe is pulsed for 0.5 ms and the power as a function of time is measured using a photodetector (Thorlabs # PDB450A) and viewed on an oscilloscope (Tektronix TDS 3034B). With this setup, for 10 μW of power, the corresponding voltage on the oscilloscope is 0.275 V. The probe is pulsed while the MOT is present, and the intensity is measured again. The transmitted signal with and without the MOT present is shown in Fig. 34.

Taking the difference of the two signals and converting to power reveals the probe power lost during the optical pumping process, as shown in Fig. 35. Integration of this curve to a decaying exponential, and subtraction of the offset due to power fluctuations during the experimental process, shows a total loss of $\Delta E = 7.35 \times 10^{-11}$ J. The total number of atoms

N in the MOT is given by

$$N = \frac{1}{2}\frac{\Delta E \lambda}{hc}. \tag{108}$$

For this MOT, $N = 144 \times 10^6$. By taking a fluorescence image immediately after the optical pumping process, a conversion between fluorescence counts and atom number can be made. Using absorption imaging as a calibration a conversion factor of 0.35(1) atoms/count is measured. The optical pumping method reconfirms this measurement with a conversion of 0.358(9) atoms/count. Using this conversion factor, the number of atoms in the FORT can be measured through fluorescence imaging.

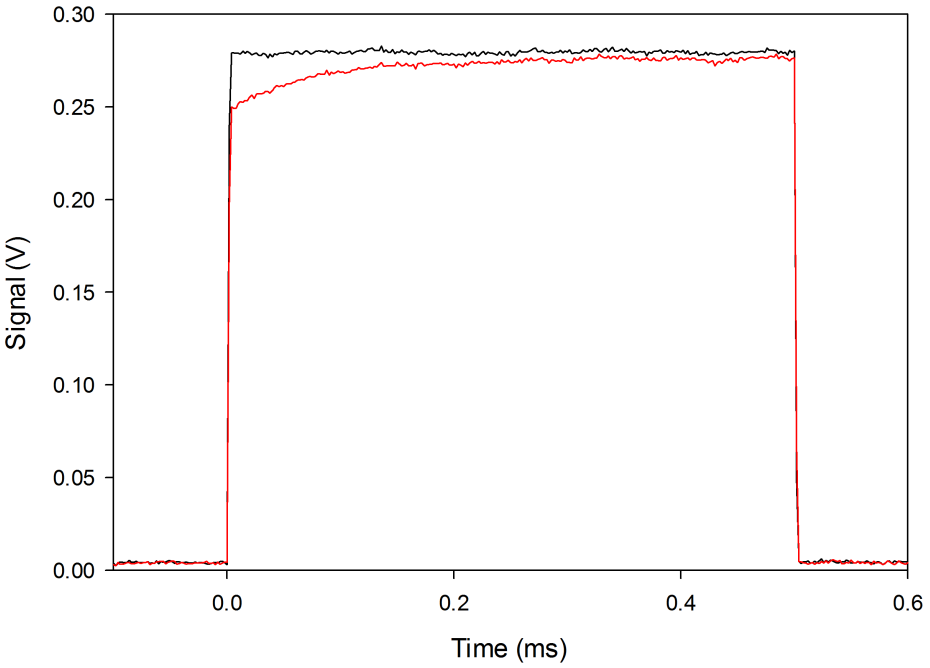

FIG. 34: The probe intensity over time is shown with (red) and without (black) the MOT present. Each atom absorbs on average 2 photons from the probe.

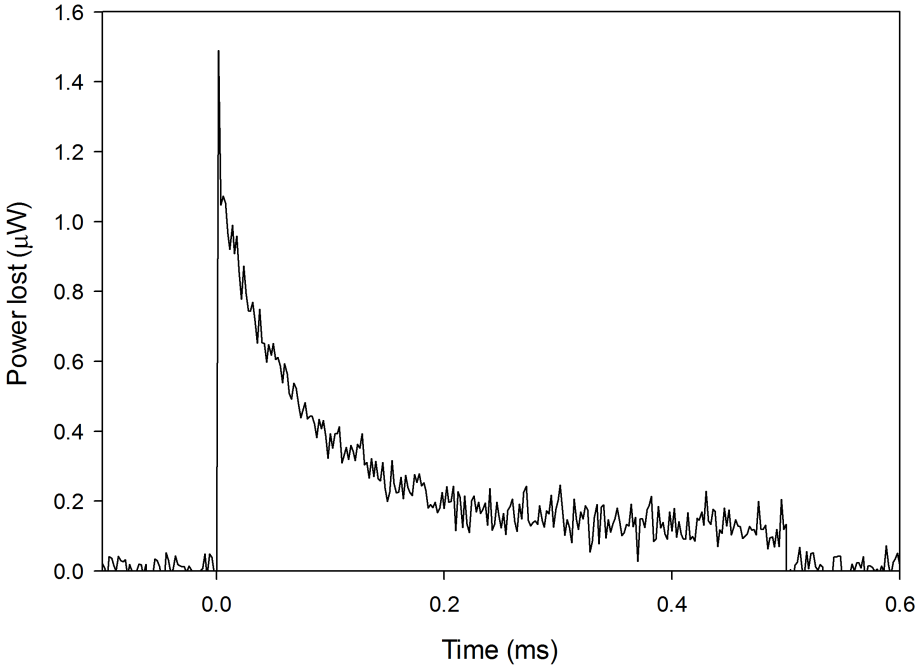

FIG. 35: The power lost over time corresponds to the number of atoms decaying to the $F = 1$ ground state. Once all of the atoms are optically pumped from the $F = 2$ ground state, the probe is fully transmitted through the MOT.

3.6.2 TEMPERATURE

After finding the number of atoms in the FORT, it is necessary to know the temperature of the atom sample. The FORT has a bi-Gaussian distribution of atoms

$$n(r,z) = n_0 \exp\left(-\frac{r^2}{2r_0^2} - \frac{z^2}{2z_0^2}\right) \tag{109}$$

and a Maxwell Boltzmann distribution of velocities [52]

$$f(v) = \left(\frac{2\pi k_B T}{m}\right)^{-3/2} \exp\left(-\frac{mv^2}{2k_B T}\right). \tag{110}$$

Here, m is the mass of an individual atom, k_B is the Boltzmann constant, and T is the average temperature of the sample. When atoms in the FORT are released from the trap, their position will change with time

$$\vec{r} = \vec{r}\,' + \vec{v}\,t. \tag{111}$$

The new distribution of atoms, which is itself a bi-Gaussian distribution, is given by

$$n(\vec{r}) = \iiint_{-\infty}^{\infty} d^3v\ f(v)\ n(\vec{r} - \vec{v}\,t). \tag{112}$$

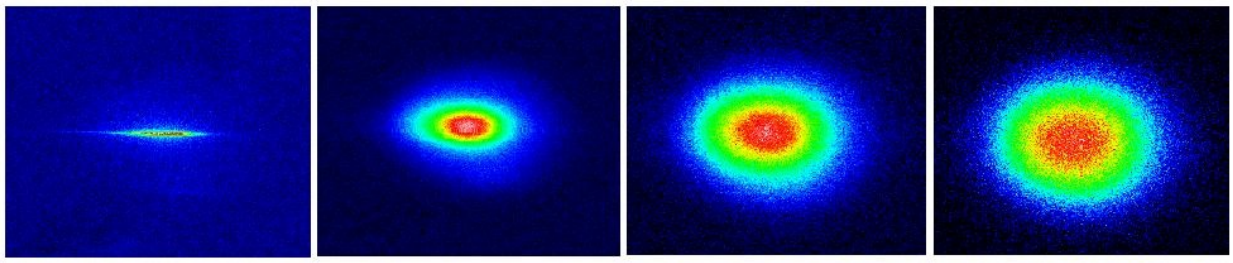

FIG. 36: During ballistic expansion, the trapping laser is extinguished and the FORT expands over time. The rate of expansion depends upon the temperature of the sample.

If we allow the cloud of atoms to ballistically expand, we can find the two radii of the sample as a function of time. Fluorescence images of the FORT are taken, as in Fig. 36, and the vertical and horizontal cross sections are fit to a Guassian distribution. The temperature

of the sample is related to the rate at which the sample expands.

$$\begin{aligned} r^2 &= r_0^2 + \tfrac{k_B T}{m} t^2 \\ z^2 &= z_0^2 + \tfrac{k_B T}{m} t^2 \end{aligned} \tag{113}$$

A fit of r^2 vs. t^2 and z^2 vs. t^2 results in a slope of $k_B T/m$, as shown in Fig. 37. Typical FORT and MOT temperatures are $\sim$100 μK, while the compressed MOT temperature is $\sim$25 μK.

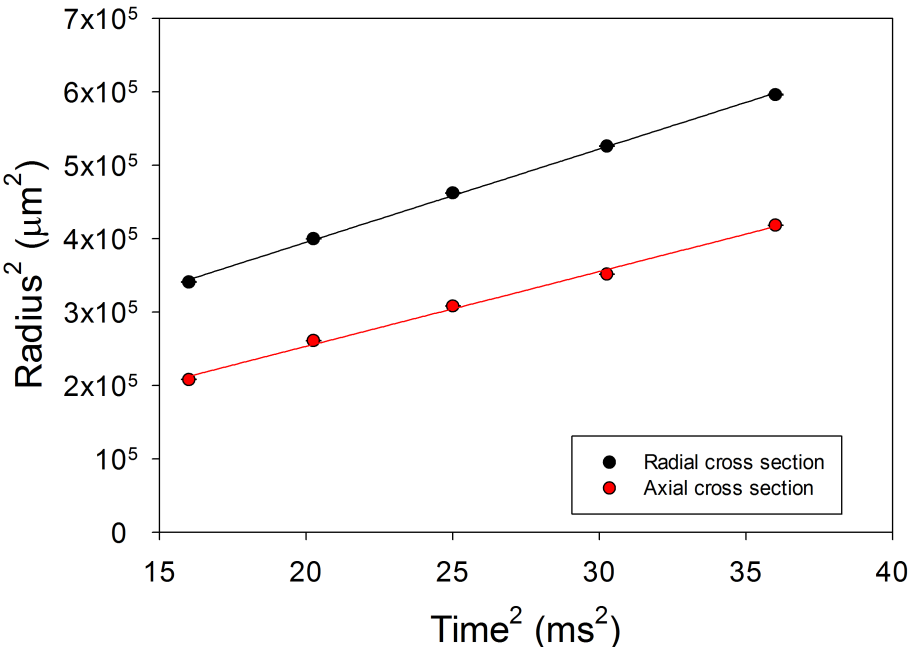

FIG. 37: The radius of the FORT is measured during ballistic expansion after a hold time of 200 ms. The slope of the linear fit for r^2 vs. t^2 gives the radial temperature (black), and z^2 vs. t^2 gives the axial temperature (red).

3.6.3 PARAMETRIC RESONANCE

Finally, to find the initial radii of the FORT potential, and thus the effective volume, we utilize parametric resonance. Because the sample of atoms does not fully fill the trap, the radial and axial radii for the sample are smaller than the beam waist and Rayleigh range. The dipole potential can be approximated as a harmonic oscillator

$$U(r,z) \approx -U_0 \left(1 - \left(\frac{z}{z_r^2}\right)^2 - 2\left(\frac{r}{w_*^2}\right)^2\right). \tag{114}$$

This can be rewritten to include a radial oscillation frequency ω_r and transverse frequency ω_z

$$U(r,z) = -U_0 + \frac{1}{2} m\, \omega_r^2\, r^2 + \frac{1}{2} m\, \omega_z^2\, z^2 \tag{115}$$

with harmonic oscillation frequencies of [70]

$$\begin{aligned} \omega_r &= \sqrt{\tfrac{4U_0}{m w_*^2}} \\ \omega_z &= \sqrt{\tfrac{2U_0}{m z_r^2}}. \end{aligned} \tag{116}$$

We begin with a trapping beam with an intensity given by Eq. (91), and then apply a sinusoidal modulation to this intensity using a pulse generator (BK Precision 4084 20 MHz function generator) for a fixed time while the atoms are held in the potential. The strength of the modulation is h, and the frequency is ω.

$$I(r,z,t) = I(r,z) + I_0\; h \cos(\omega\, t)\,. \tag{117}$$

The one dimensional Mathieu equation describes the motion of atoms within the trap

$$\ddot{r} + \kappa\, \dot{r} + \omega_r^2\, r\,(1 + h\;\cos(\omega\, t)) = 0 \tag{118}$$

with a relaxation rate κ. A resonance occurs when

$$\omega = 2\omega_r/n, \qquad n = 1, 2, \ldots. \tag{119}$$

After undergoing intensity modulation for 200 ms, the atoms remaining in the FORT are allowed to expand before a CCD image of the FORT fluorescence is taken. The central portion of the signal is integrated over a region of 6 pixels $\times$ 6 pixels and plotted over a range of frequencies. On resonance, the atoms are thermally excited out of the FORT and the fluorescence signal is diminished [75], as shown in Fig. 38. Fitting the loss curve to a Guassian gives the first radial resonance of $\omega = 2\omega_r = 2\pi \times 8.34(4)$ kHz. Because $z_R >> w_*$, the transverse resonance ω_z is a much lower frequency that is not easily resolvable.

The sample's thermal and spatial density distribution in the potential well is determined by

$$n(\overrightarrow{r}) = n_0 \exp\left(-\frac{U(\overrightarrow{r})}{k_B T}\right). \tag{120}$$

with a thermalized temperature given by T, and k_B being Boltzmann's constant. Comparison

Radial frequency	ω_r	$2\pi\times$ 4.17(2) kHz
Transverse frequency	ω_z	$2\pi\times$ 0.087(4) kHz
Beam waist	ω_*	17.4(5) μm
Rayleigh range	z_r	897(10) μm
Trap depth	U_0	700(10) μK
Scattering rate	γ_p	$2\pi\times$ 1.1(1) Hz

TABLE 3: The FORT trap characteristics for a sample with a temperature of 96(5) μK and a power of 2 W are found using parametric resonance.

	MOT	Compressed MOT
N ($\times 10^6$)	145(5)	50(1)
T (μK)	100(10)	25(1)
r_0 (μm)	750(30)	500(25)
n_0 (atoms/cm^3)	2.2(3) $\times 10^{10}$	2.5(4) $\times 10^{10}$

TABLE 4: Typical sample characteristics for the MOT and compressed MOT are listed.

with the spatial density of the FORT in Eq. (109) gives the radii of the atomic sample in terms of the temperature and parametric resonance frequencies.

$$r_0 = \sqrt{\frac{k_b\, T}{m\omega_r^2}}; \qquad z_0 = \sqrt{2}\pi\; r_0\; \omega_*/\lambda \tag{121}$$

3.6.4 SAMPLE CHARACTERISTICS

By using the methods previously described, the MOT, compressed MOT, and FORT can be characterized. The physical properties of the uncompressed and compressed MOT are listed in Table 4. These are all typical values, and must be taken as general properties of the samples. Fluctuations in MOT number and density occur depending on how much warm Rb vapor is available in the chamber. The values listed for the FORT in Table 5 are after a 200 ms hold time, which allows time for the atoms to thermalize in the trap.

3.7 CONTROLLING SAMPLE PROPERTIES

In order to study the effects of a broad range of sample parameters, we need a dependable

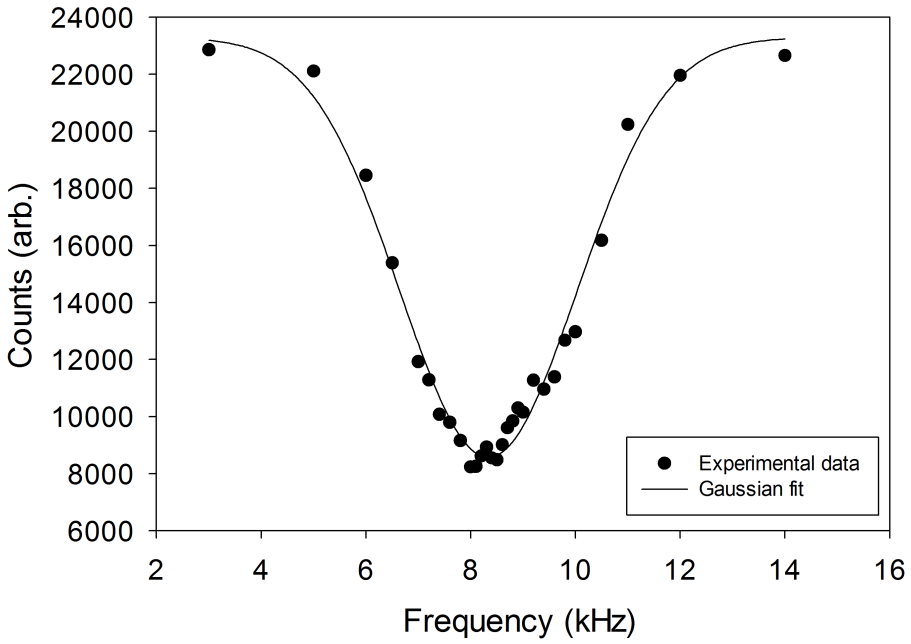

FIG. 38: The first parametric resonance, at $\omega = 2\omega_r$ causes the integrated fluorescence from the center of the FORT to be reduced. This is for a modulation depth of $h = 0.025$.

N ($\times 10^5$)	7.8(1)
T (μK)	100(6)
r_0 (μm)	3.4(1)
z_0 (μm)	250(10)
b_0 (Radial)	20
b_0 (Axial)	1500
n_0 (atoms/cm^3)	2 $\times 10^{13}$

TABLE 5: Typical sample characteristics for the FORT are listed.

and repeatable way to modify the peak density and optical depth of the system.

3.7.1 HOLD TIME

The first method to reduce the density is to change the number of atoms within the FORT. The change in the number of atoms in the FORT can be described by

$$\frac{dN}{dt} = -\Gamma N - \beta N^2, \tag{122}$$

where Γ in an exponential loss rate due to background gas collisions, and β is a collisional loss coefficient that derives from atom-atom collisions within the FORT [68]. Initially, the FORT has a large distribution of temperatures. Atoms within the sample collide and become thermalized at a rate of β.

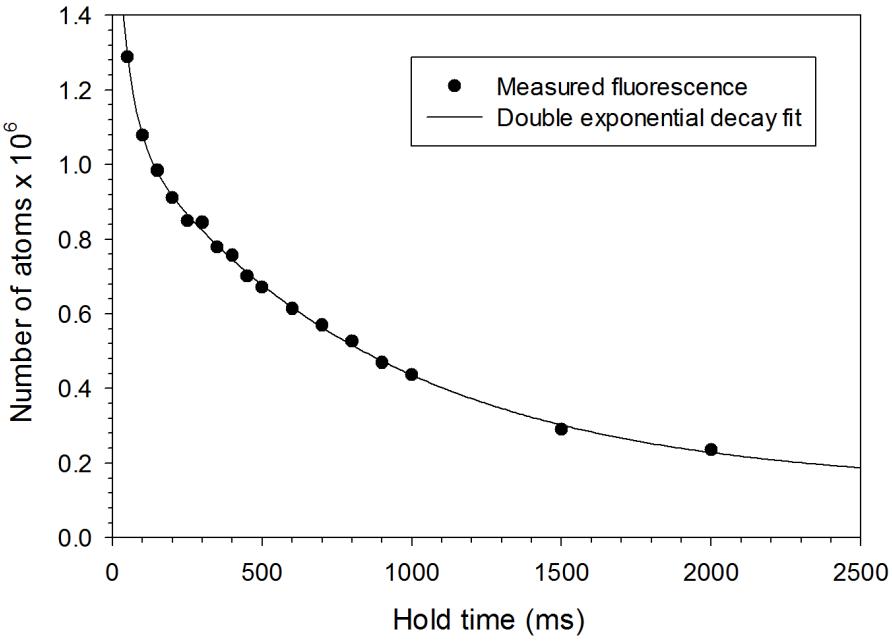

FIG. 39: The decay of the number of atoms in the FORT follows a double exponential curve.

By holding the atoms for a longer time in the FORT before probing, the number of atoms is reduced, as shown in Fig. 39. The decay is fit to a double exponential

$$N = ae^{-t/\tau_1} + be^{-t/\tau_2} + c \tag{123}$$

where $\tau_1 = 67(12)$ ms is the fast decay time due to collisions within the sample, and $\tau_2 = 1.25(5)$ s is the lifetime of the trap. After the initial fast decay, the FORT is near thermal

equilibrium. There is still residual cooling ($\sim 10\%$) from 200 ms to 5 seconds, which resorts in the sample having smaller Gaussian radii with extended hold times.

3.7.2 EXPANSION

The second method to modify sample parameters is to allow the sample to expand. After turning off the fiber laser, the atoms are allowed to expand before probing. The radii are then given by Eq. 113. For each FORT hold time, the number of atoms N and the temperature T is measured, while the parametric resonance frequencies are not changed. Thus, the Gaussian radii of the sample after some expansion time t are given by

$$r^2 = \frac{k_b T}{m}\left(\frac{1}{\omega_r^2} + t^2\right) \tag{124}$$

$$z^2 = \frac{k_b T}{m}\left(\frac{1}{\omega_z^2} + t^2\right). \tag{125}$$

The peak density of the FORT is

$$n_0 = N\left(\left(\frac{2\pi k_b T}{m}\right)^{3/2}\left(1/\omega_r^2 + +t^2\right)\left(1/\omega_z^2 + t^2\right)^{1/2}\right)^{-1} \tag{126}$$

and the optical depth in the radial direction is

$$b_0 = n_0\sigma_0\sqrt{\frac{2\pi k_b T}{m}\left(\frac{1}{\omega_r^2} + t^2\right)}. \tag{127}$$

CHAPTER 4

DIFFUSE SCATTERING

4.1 DATA ACQUISITION

To observe diffuse scattering from the FORT, a linearly polarized probe laser beam tuned in the vicinity of the $F = 2 \rightarrow F' = 3$ transition is used. Because the atoms are trapped in the $F = 1$ ground state, the repumper laser is used to optically pump the atoms into the $F = 2$ ground state before data acquisition begins. This process occurs after the fiber laser is turned off and takes 8 μs. The probe laser beam, with a power of 40 μW and $1/e^2$ radius of 4.4 mm, is then directed through the pair of off-axis windows in the vacuum chamber, and the fluorescence from the FORT is collected through a window perpendicular to the fiber laser, as shown in Fig. 40. The collected light is transmitted through a multimode optical fiber to a photomultiplier tube (PMT) (Hamamatsu # R9110) supplied with 1250 V, which is connected directly to a multichannel scalar (MCS) with 40 ns time bin resolution.

To reduce the total time required to take data, a sequence of 10 1 μs probe pulses occur while the sample is expanding, with each pulse being separated in time by 40 μs. Because the intensity of the probe is 0.08 s_0, optical pumping to the $F = 1$ ground state is not a concern. We are able to acquire data for a constant number of atoms in 10 different spatial volumes V. Here, $V = (2\pi)^{3/2} r^2 z^2$ is the Gaussian volume such that the peak density for a sample of N atoms is $n_0 = N/V$. With N being held constant, the effects of the probe detuning are studied along with V.

Additional measurements are performed in which the probe laser is tuned directly to resonance. The hold time of the FORT is extended, leading to a reduction in N. For each designated hold time, N is measured using fluorescence imaging. Additionally, the temperature of the sample is found. The peak density during expansion for each hold time is shown in Fig. 41. The number of accumulations for each N is varied to maintain the same signal to noise throughout the experimental process and to reduce the total run time. A single accumulation at the shortest hold time, from forming the MOT to collecting scattered probe light from the FORT, takes 6.1 seconds. Increasing the hold time also increases the time for each accumulation. As such, a single data point can take up to nearly 5 hours.

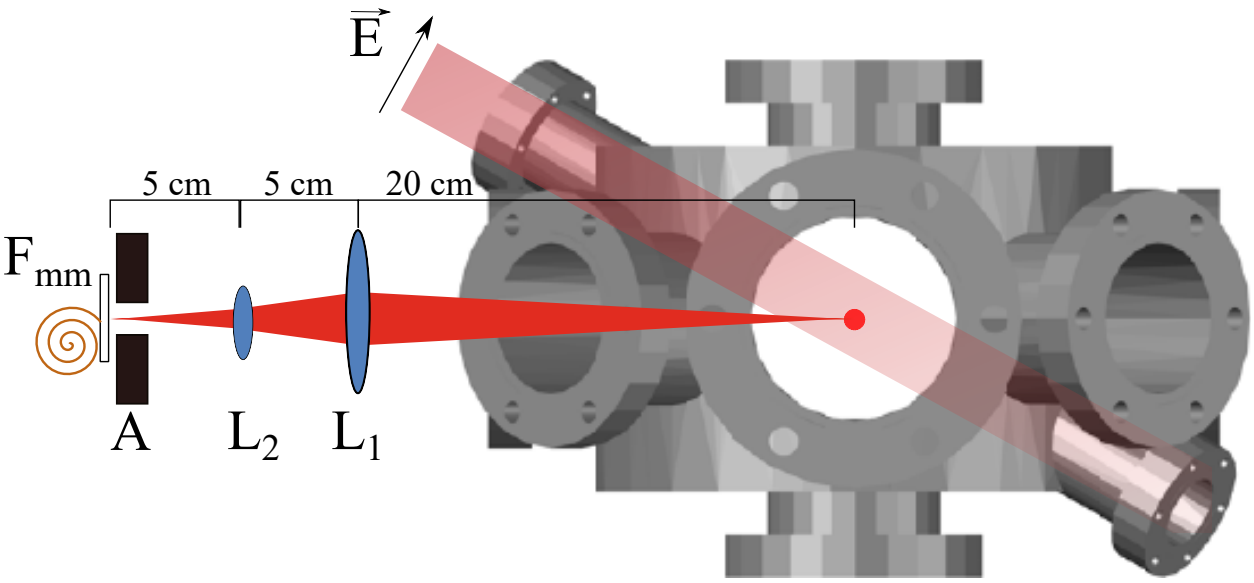

FIG. 40: Fluorescence due to scattering from the probe is collected off-axis. The linear polarization of the electric field of the probe $\vec{E}$ is indicated by the arrow. A pair of lenses L_1 and L_2 with respective focal lengths $f_1 = 10$ cm and $f_2 = 7.5$ cm are used to collect and focus the light into a multimode non-polarization preserving fiber F_{mm}. An aperture A in front of the fiber is used to block residual background light.

Therefore, as the number of atoms is reduced, the total number of accumulations is increased proportionally, as shown in Table 6. The final data is scaled accordingly.

The signal from the MCS after a 200 ms FORT hold time with an on-resonance probe is shown in Fig. 42. Because of the limits of our pulse generator, the repumper is also flashed before each probe flash. The fluorescence due to hot atoms in the chamber is visible in the timing sequence, but is easily subtracted by performing a background run when no FORT is present. For better visibility, all 10 probe pulses are shown together in Fig. 43.

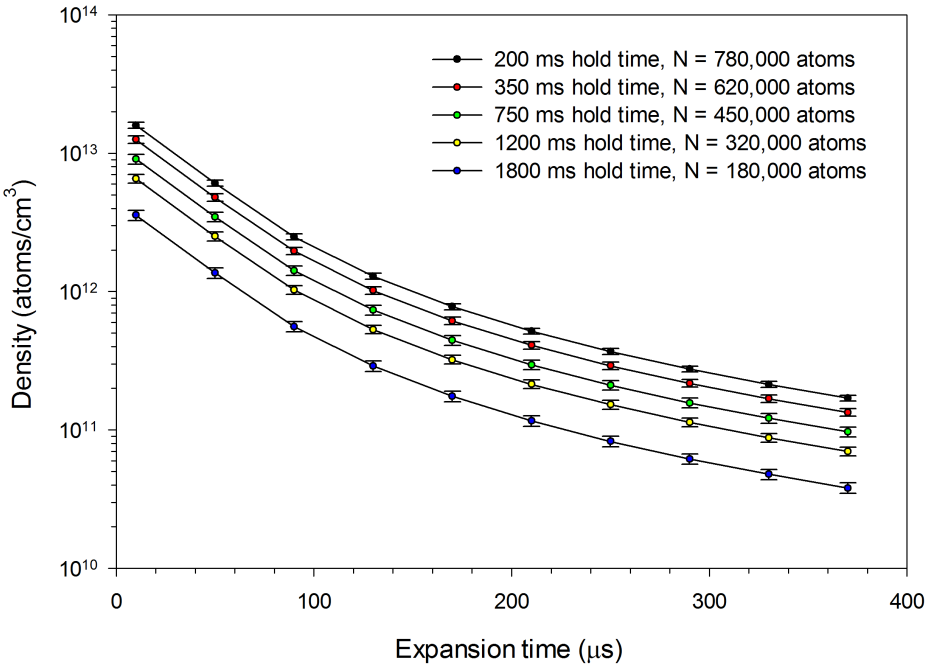

FIG. 41: By increasing the hold time and expansion time, the density of the FORT can be modified by reducing the number of atoms and increasing the spatial size of the sample. Data is taken for a set hold time and corresponding number of atoms. The fluorescence from each probe pulse is recorded for the sample as it expands.

Hold time (ms)	Number of accumulations
250	480
350	600
750	830
1200	1160
1800	2172

TABLE 6: For the on-resonance measurements, the number of accumulations for each hold time increases due to the reduction in the signal. The final data is scaled by the ratio of the number of accumulations to that of the 1800 ms hold time. The spectral response was measured using 2400 accumulations.

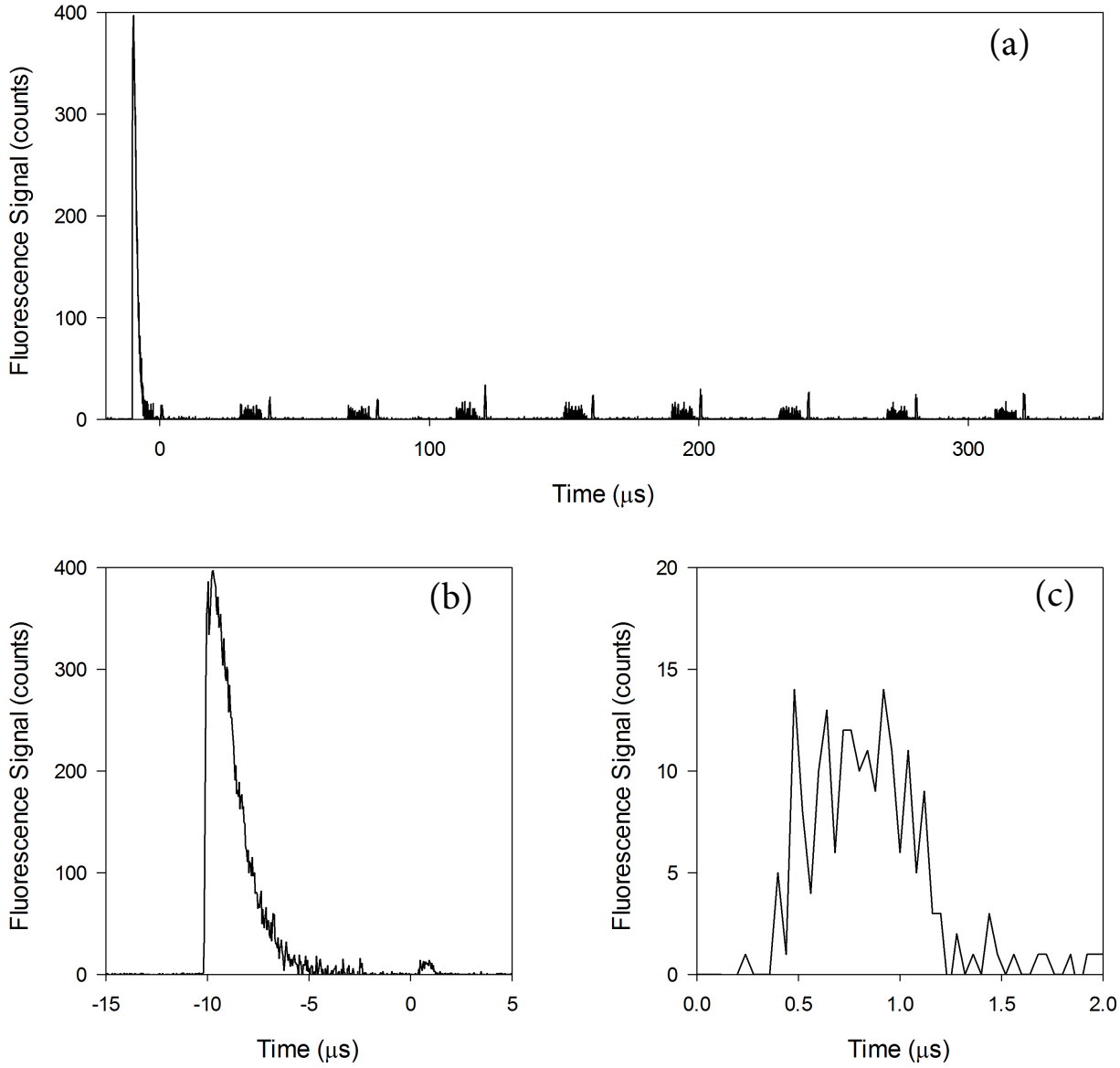

FIG. 42: The signal output from the multichannel scalar (MCS) during the probing process is accumulated into time bins. a) FORT fluorescence due to light scattering from the repumper and probe over a sequence of 10 pulses is shown. b) The atoms fluoresce as they are optically pumped by the repumper laser from the $F = 1$ to the $F = 2$ ground state, and then scatter light from the probe. c) The fluorescence from the probe during the first of 10 1 μs pulses is shown.

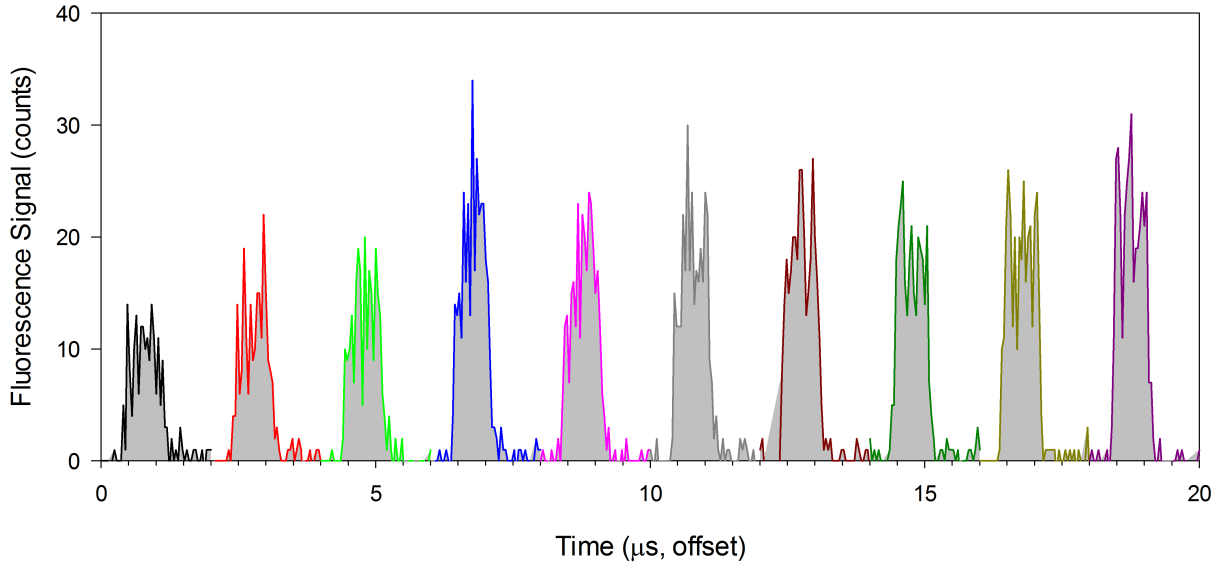

FIG. 43: From left to right, all 10 probe pulses for an expanding sample are shown in sequential order, with the time scale adjusted to clearly see the dynamics for each pulse. Each pulse is integrated over 1 μs to find the total fluorescence scattered for the corresponding volume.

4.2 RESULTS

4.2.1 SPECTRAL DEPENDENCE

For a hold time of 200 ms, the probe laser frequency ω is set to a detuning $\delta = \omega - \omega_0$ from the $F = 2 \rightarrow F' = 3$ transition frequency ω_0. As the sample expands, the probe is flashed for 1 μs in 40 μs increments. After 2400 cycles, the probe detuning is changed and the experiment is repeated. The measured fluorescence as a function of optical depth b_0 with constant detuning is shown in Fig. 44. On resonance, the sample scatters collectively with increased optical depth. With N being constant, the total fluorescence increases as the sample expands. The effective optical depth $b = b_0/(1 + (2\delta/\gamma)^2)$ is greatly reduced when the probe is detuned from resonance; this results in the fluorescence returning to a constant intensity regardless of sample size. The same effects are seen using the random walk (RW) model.

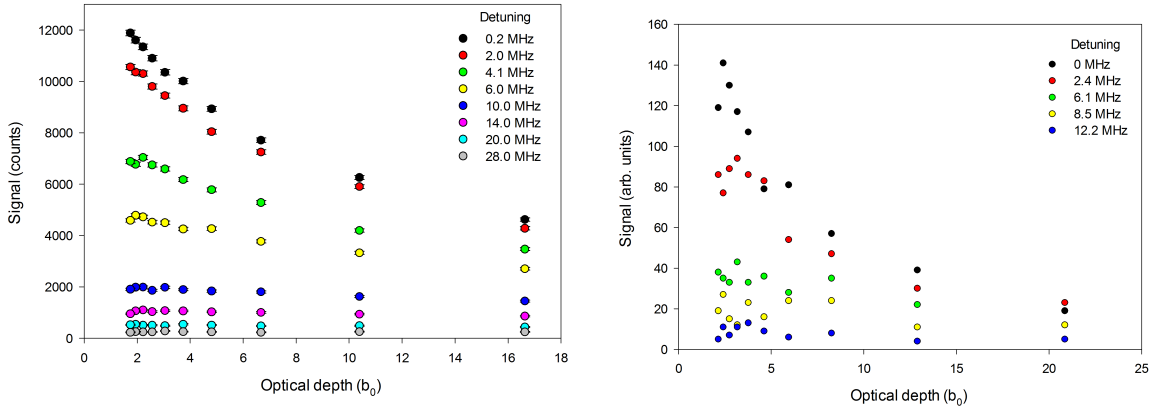

(a) (b)

FIG. 44: a) For a set probe detuning, the detected fluorescence decreases with increasing optical depth. Detuning well from resonance reduces the effective optical depth of the system and the fluorescence appears to remain constant with volume. b) The RW model shows a decrease in light scattered in the $\phi = \pi/2$ direction with increasing on resonance optical depth. Detuning of the excitation and the reduction in the optical depth shows a nearly constant scattering intensity.

A plot of the spectral dependence of the scattered light at each sample expansion time is shown in Fig. 45. Each curve is fit to a Lorentzian with a resonance width γ,

$$I = \frac{I_0}{1 + (2\delta/\gamma^2)}. \tag{128}$$

While the natural resonance width of ^{87}Rb is 6.1 MHz, there is a pronounced broadening with increased optical depth in both the experiment and RW model, as shown in Fig. 46. A fit to the experimental results reveals the broadening scales as $\sqrt{b_0}$. For $b < 1$, the light is able to penetrate the sample and classical scattering takes place. The detuning of the probe for this process scales as

$$\delta = \frac{\gamma}{2}\sqrt{b_0}. \tag{129}$$

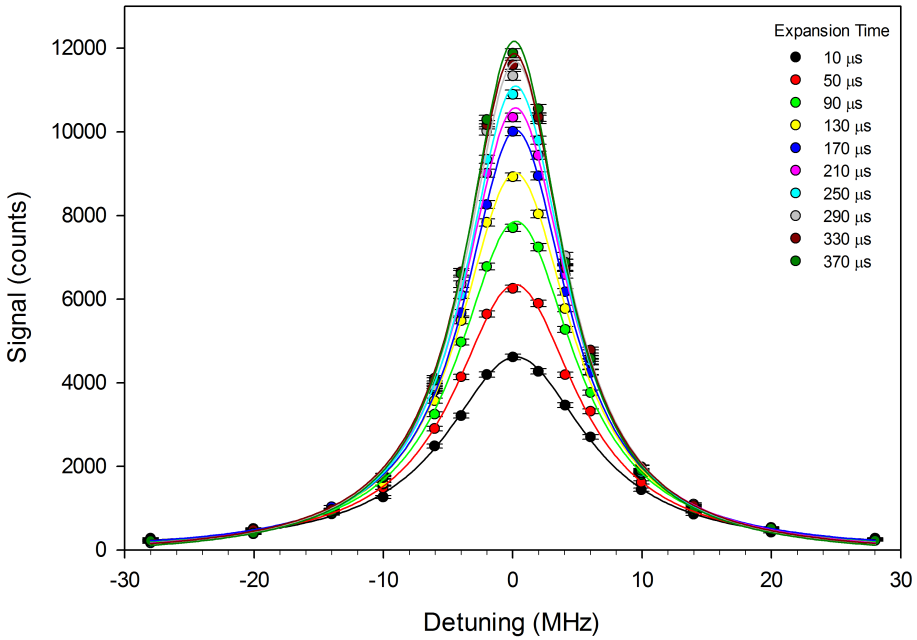

FIG. 45: The experimentally measured spectral response of the atomic system for an expanding sample with a constant number of atoms is shown. As the sample expands, the peak fluorescence increases until it approaches a steady-state value. Each curve is fit to a Lorentzian line shape.

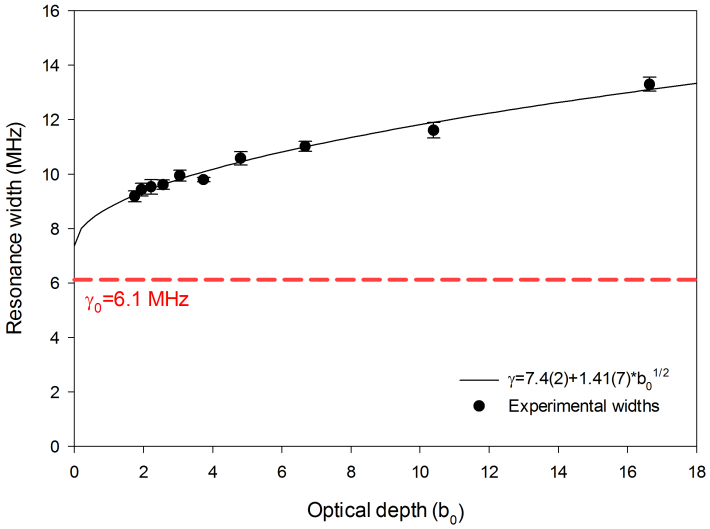

(a)

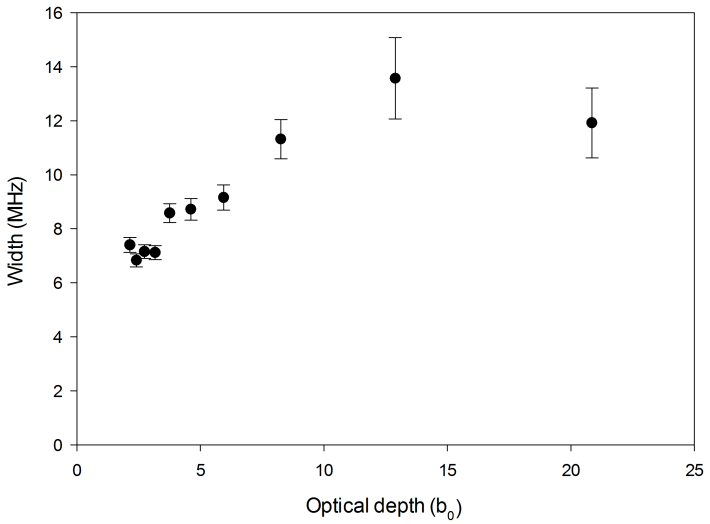

(b)

FIG. 46: a)The experimentally measured width γ increases with optical depth. The natural resonance width $\gamma_0 = 6.1$ MHz is indicated by the red dashed line. b)The RW model predicts a spectral broadening with increased optical depth.

4.2.2 ON RESONANCE

The spectral response of the sample is only measured for a sample with constant N and increasing V. To observe the effects of both N and V together, the probe is tuned directly to resonance. In Fig. 47, the volume dependence of the scattered light at constant N is shown. For the samples with a shorter hold time, corresponding to increased N, density n_0, and optical depth b_0, we see that the scattering rate is reduced for smaller volumes. As the samples expand, the scattering becomes constant for each N. As the number of atoms reduces, the scattered light remains constant with volume.

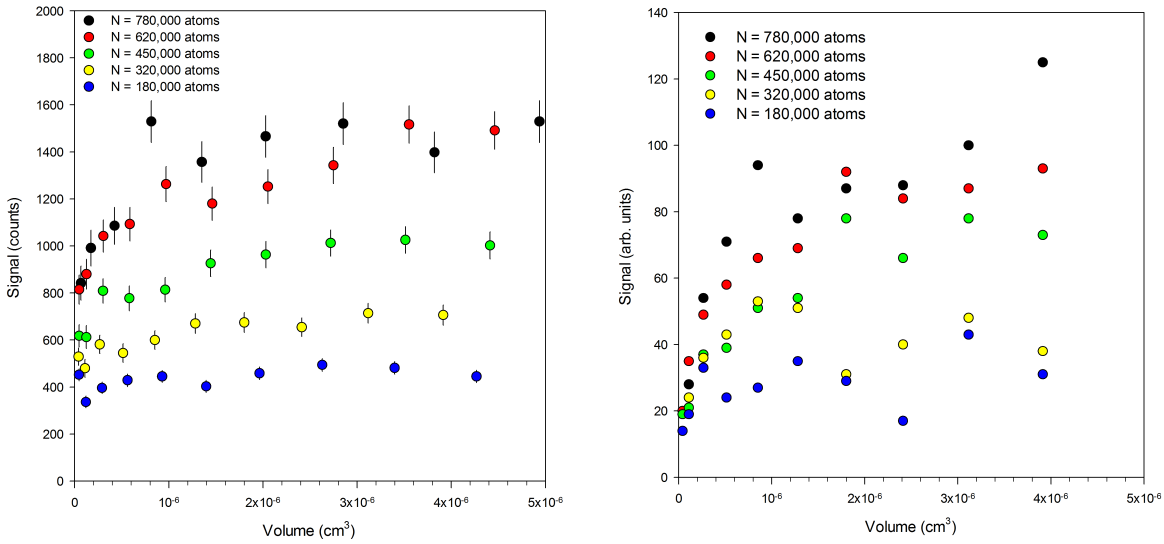

(a)

FIG. 47: For a constant number of atoms N, the on-resonance scattered light decreases as the sample becomes more compact in both a) experiment and b) the RW model.

Similarly, we can study the effects of increasing N at constant volumes V. In the steady state regime, the total scattered light should be proportional to N. However, as shown in Fig. 48, the FORT exhibits collective scattering in which the total scattered field does not scale linearly with N for small volumes. As the sample expands, the volume increases and we see a return to a linear scaling. According to Beer's Law, the scattered light intensity should scale as $1 - e^{-b}$, which is equal to the optical depth for small b. With V being constant, the number of atoms is proportional to b. In samples with $b >> 1$, the total scattered light no longer scales linearly with the optical depth, but asymptotically approaches a constant value. This appears as a reduction in the scattering rate of the sample.

In classical scattering, the total scattered light intensity should be proportional to the

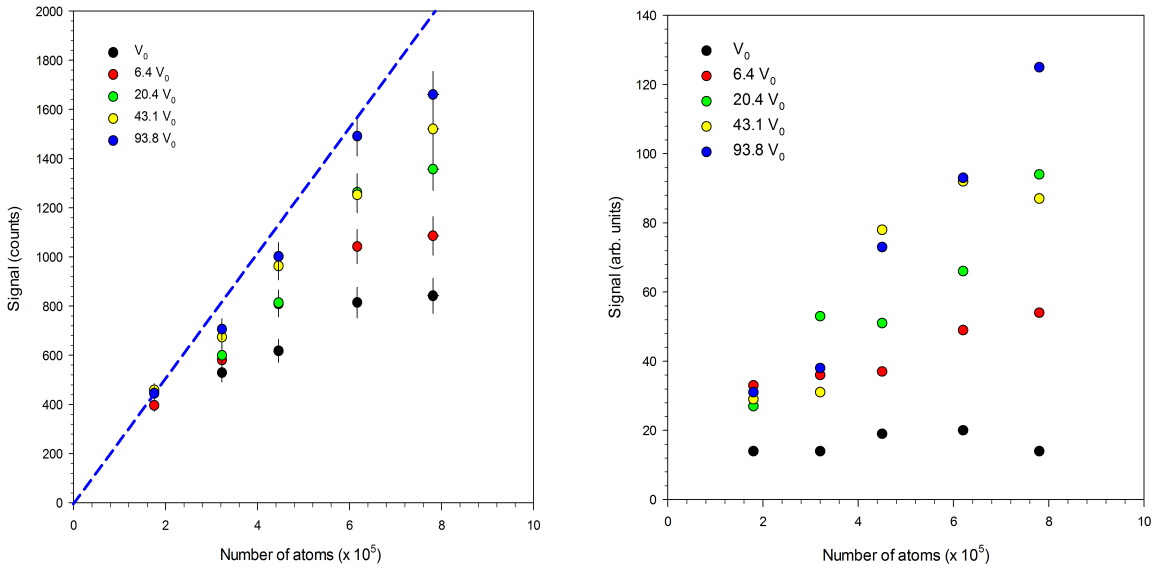

(a) (b)

FIG. 48: a) For a constant Gaussian volume V, the experimentally measured on-resonance scattered light decreases with increasing N. Here, $V_0 = 6.6(3) \times 10^{-8}$ cm^3 is the volume of the FORT with a 200 ms hold time and 10 μs expansion time. Allowing the sample to expand will return a linear relationship between the scattered field and N, as indicated by the blue dashed line. b) A similar reduction in signal is observed in the RW model.

number of scatterers. We clearly see that is not the case, and is largely dependent on global sample parameters. A plot of the scattered light as compared to the optical depth of the system is shown in Fig. 49. Here we can see the increase in scattered light with increasing N. By normalizing the measured scattered fluorescence by N for each sample, we can see a clear reduction in the scattering cross section per atom that scales as $1/\sqrt{b_0}$, as shown in Fig. 50. As the resonance width γ increases as $\sim \sqrt{b_0}$, the scattering rate is inversely proportional. The spectral integral should remain constant to conserve probability.

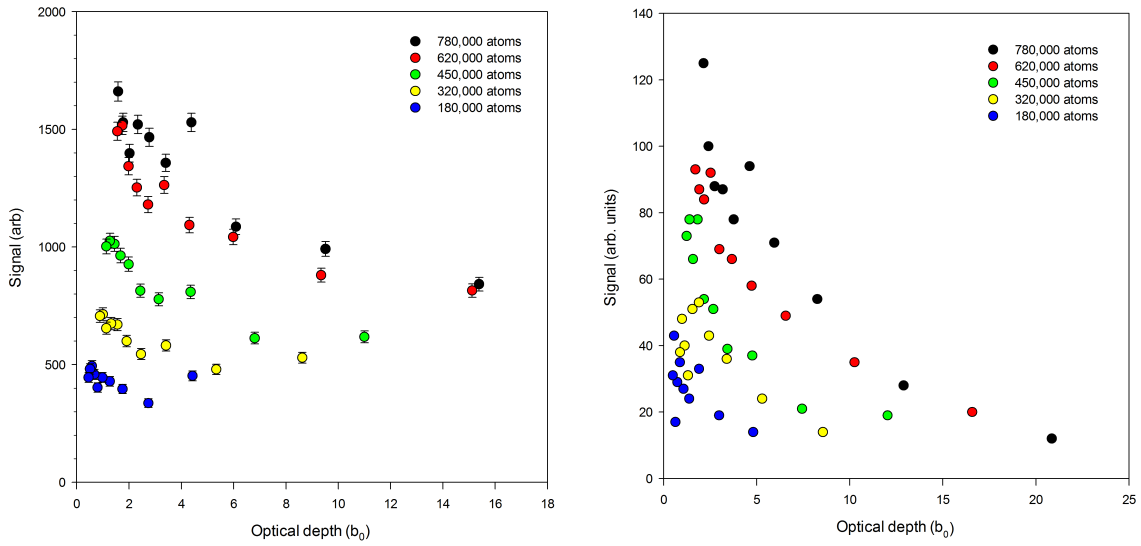

(a) (b)

FIG. 49: For a constant number of atoms N, both a) experiment and b) the RW model show that the collected scattered light decreases with increasing optical depth b_0.

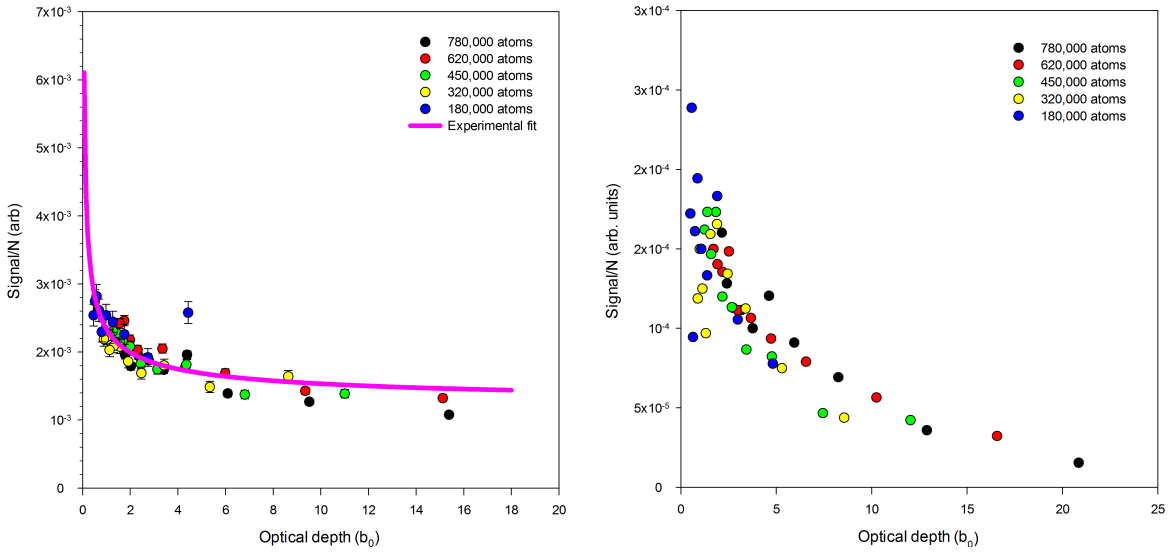

(a) (b)

FIG. 50: The signal from Fig. 49 is normalized to the number of atoms N in the atomic sample. Both a) experiment and b) the RW model show that the collected signal per atom (S/A) falls along a single curve. The fit to the experimental data results in $S/A = 1.2(1)\left(1 + 1/\sqrt{b_0}\right)$

CHAPTER 5

CONCLUSIONS

The atomic samples studied in this thesis have a range of physical characteristics. The number of atoms ranges from 180,000 to ∼1 million, while the Gaussian volumes are $(10^5 \to 10^7)\,\lambda^3$, where $\lambda = 780.24$ nm is the wavelength of the probe. With peak densities n_0 in the range of $4 \times 10^{10} \to 2 \times 10^{13}$ atoms/cm^3, we are able to investigate samples with radial on-resonance optical depths b_0 in the range of $0.5 \to 20$. The probe frequency can be offset from the $5s^2S_{1/2}, F = 2 \to 5s^2P_{3/2}, F' = 3$ transition by an amount δ. The optical depth b is then reduced,

$$b = \frac{b_0}{1 + (2\delta/\gamma)^2}, \tag{130}$$

where γ is the resonance width for the sample.

By studying such a large range of parameters, the emergence of collective scattering has been observed in the mesoscopic regime, between the microscopic and macroscopic regimes. For atomic samples with $b \sim 1$, the scattered light intensity is well described as the sum of N independent atoms. As N increases, or V decreases, there is an increase in b_0. This results in the scattering rate being determined by the sample parameters, rather than the individual atomic responses. When the probe is detuned from resonance, the effective optical depth is reduced, and the atomic sample once again scatters classically. It is important to note that collective scattering is present even though the atomic separation r is large. Only the $1/kr$ component could contribute significantly in the dipole-dipole interaction, yet the suppression of scattering is still observed, similar to that of atoms in a microtrap [26].

The experimental results have been compared to a random walk (RW) simulation. For similar sample parameters and excitation geometries, qualitatively similar results have been observed. Resonance width broadening and the associated reduction in the scattering cross section show a clear scaling with the on-resonance optical depth of the system. Using the RW model, we can see a clear transition from single to multiple scattering. Larger samples scatter more light due to the increase in the flux of photons traversing the sample, and the photons statistically scatter fewer times within the sample before escaping. More compact samples have a lower probability of initially scattering a photon, but photons that are scattered undergo multiple scattering. Additionally, as the optical depth increases, surface scattering occurs, in which the light is not able to initially fully penetrate the sample.

For $b_0 << 1$, the light should be able to fully penetrate the sample. As b_0 increases, the incident probe is unable to penetrate the sample, which would result in more light being scattered in the backwards direction. As such, future investigations into this process should include observing the spatial distribution of the scattered light. Probing along the long axis of the FORT would provide an optical depth 75 times as that of the radial direction, arguably greater than that of similar experiments. Measuring the forward transmission of light parallel and perpendicular to the FORT's long axis can reveal more information about the collective and cooperating scattering properties of the ensemble.

Experimentally, the largest constraint in collecting more data is the duty cycle for trapping atoms and probing the FORT. Improvements have already been implemented to probe and retrap the atomic sample up to 300 times before repeating the loading process from the MOT. This can drastically reduce the total running time for an experiment and allow future investigations to take considerably less time.

The emergence of collective scattering can have a large effect on atomic quantum sensors and devices. Resonance broadening and a reduction in the scattering cross section may reduce the effectiveness of increasing atomic densities and/or optical depths for purposes of increasing signal-to-noise. As the ensemble behaves more like a macroscopic object, a microscopic description of the individual scatterers is no longer an accurate model for the system. Rather, the spectroscopic properties must scale with the large-scale physical parameters.

BIBLIOGRAPHY

[1] Andrew D. Ludlow, Martin M. Boyd, Jun Ye, E. Peik, and P. O. Schmidt. Optical atomic clocks. *Reviews of Modern Physics*, **87**:637–701, 2015.

[2] S. A. Diddams, Th. Udem, J. C. Bergquist, E. A. Curtis, R. E. Drullinger, L. Hollberg, W. M. Itano, W. D. Lee, C. W. Oates, K. R. Vogel, and D. J. Wineland. An optical clock based on a single trapped 199Hg+ ion. *Science*, **293**(5531):825–828, 2001.

[3] Z. W. Barber, J. E. Stalnaker, N. D. Lemke, N. Poli, C. W. Oates, T. M. Fortier, S. A. Diddams, L. Hollberg, C. W. Hoyt, A. V. Taichenachev, and V. I. Yudin. Optical lattice induced light shifts in an Yb atomic clock. *Physical Review Letters*, **100**(10):103002, 2008.

[4] John Kitching, Svenja Knappe, and Elizabeth A. Donley. Atomic sensors - a review. *IEEE Sensors Journal*, **11**:1749–1758, 2011.

[5] M. Kasevich and S. Chu. Measurement of the gravitational acceleration of an atom with a light-pulse atom interferometer. *Applied Physics B*, **54**(5):321–332, 1992.

[6] K. F. Woodman, P. W. Franks, and M. D. Richards. The nuclear magnetic resonance gyroscope: a review. *The Journal of Navigation*, **40**:366–384, 1987.

[7] W. Wasilewski, K. Jensen, H. Krauter, J. J. Renema, M. V. Balabas, and E. S. Polzik. Quantum noise limited and entanglement-assisted magnetometry. *Physical Review Letters*, **104**:133601, 2010.

[8] H. Xia, A. Ben-Amar Baranga, D. Hoffman, and M. V. Romalis. Magnetoencephalography with an atomic magnetometer. *Applied Physics Letters*, **89**(21), 2006.

[9] S. Kolkowitz, I. Pikovski, N. Langellier, M. D. Lukin, R. L. Walsworth, and J. Ye. Gravitational wave detection with optical lattice atomic clocks. *ArXiv e-prints*, 2016.

[10] P. W. Graham, J. M. Hogan, M. A. Kasevich, and S. Rajendran. A Resonant Mode for Gravitational Wave Detectors based on Atom Interferometry. *ArXiv e-prints*, 2016.

[11] A. I. Lvovsky, B. C. Sanders, and W. Tittel. Optical quantum memory. *Nature Photonics*, **3**:706–714, 2009.

[12] E. Vetsch, D. Reitz, G. Sagué, R. Schmidt, S. T. Dawkins, and A. Rauschenbeutel. Optical interface created by laser-cooled atoms trapped in the evanescent field surrounding an optical nanofiber. *Physical Review Letters*, **104**:203603, 2010.

[13] I. Novikova, E. E. Mikhailov, and Y. Xiao. Excess optical quantum noise in atomic sensors. *Physical Review A*, **91**(5):051804, 2015.

[14] Stephan Wildermuth, Sebastian Hofferberth, Igo Lesanovsky, Elmar Haller, L. Mauritz Andersson, Sonke Groth, Israel Bar-Joseph, Peter Kruger, and Jorg Schmiedmayer. Bose-Einstein condensates: Microscopic magnetic-field imaging. *Nature*, **435**:440, 2005.

[15] D. Reitz, C. Sayrin, B. Albrecht, I. Mazets, R. Mitsch, P. Schneeweiss, and A. Rauschenbeutel. Backscattering properties of a waveguide-coupled array of atoms in the strongly nonparaxial regime. *Physical Review A*, **89**(3):031804, 2014.

[16] V. Leong, M. A. Seidler, M. Steiner, A. Cerè, and C. Kurtsiefer. Time-resolved scattering of a single photon by a single atom. *ArXiv e-prints*, 2016.

[17] T. Bienaimé, G. Barontini, L. M. de Lépinay, L. Bellando, J. Chabé, and R. Kaiser. Fast compression of a cold atomic cloud using a blue-detuned crossed dipole trap. *Physical Review A*, **86**(5):053412, 2012.

[18] T. Bienaimé, R. Bachelard, N. Piovella, and R. Kaiser. Cooperativity in light scattering by cold atoms. *Fortschritte der Physik*, **61**:377–392, 2013.

[19] T. Bienaimé, N. Piovella, and R. Kaiser. Controlled Dicke subradiance from a large cloud of two-level systems. *Physical Review Letters*, **108**(12):123602, 2012.

[20] T. Bienaime, M. Petruzzo, D. Bigerni, N. Piovella, and R. Kaiser. Atom and photon measurement in cooperative scattering by cold atoms. *ArXiv e-prints*, 2012.

[21] I. M. Sokolov, A. S. Kuraptsev, D. V. Kupriyanov, M. D. Havey, and S. Balik. A scaling law for light scattering from dense and cold atomic ensembles. *Journal of Modern Optics*, **60**:50–56, 2013.

[22] R. Friedberg, S. R. Hartmann, and J. T. Manassah. Frequency shifts in emission and absorption by resonant systems of two-level atoms. *Physics Reports*, **7**(3):101–179, 1973.

[23] Richard Friedberg and Jamal T. Manassah. Analytic expressions for the initial Cooperative Decay Rate and Cooperative Lamb Shift for a spherical sample of two-level atoms. *Physics Letters A*, **374**:1648–1659, 2010.

[24] Jamal T. Manassah. Cooperative radiation from atoms in different geometries: decay rate and frequency shift. *Advances in Optics and Photonics*, **4**(2):108–156, 2012.

[25] Daniel Adam Steck. Quantum and Atom Optics. http://steck.us/teaching.

[26] J. Pellegrino, R. Bourgain, S. Jennewein, Y. R. P. Sortais, A. Browaeys, S. D. Jenkins, and J. Ruostekoski. Observation of suppression of light scattering induced by dipole-dipole interactions in a cold-atom ensemble. *Physical Review Letters*, **113**(13):133602, 2014.

[27] R. H. Dicke. Coherence in spontaneous radiation processes. *Physical Review*, **93**:99–110, 1954.

[28] A. Biella. From Dicke to Anderson: Interplay of superradiance and disorder. *ArXiv e-prints*, 2014.

[29] Barry M. Garraway. The dicke model in quantum optics: Dicke model revisited. *Philosophical Transactions of the Royal Society of London A: Mathematical, Physical and Engineering Sciences*, **369**(1939):1137–1155, 2011.

[30] Marlan O. Scully and Anatoly A. Svidzinsky. The Lamb shift yesterday, today, and tomorrow. *Science*, **328**(5983):1239–1241, 2010.

[31] Marlan O. Scully. Collective lamb shift in single photon dicke superradiance. *Physical Review Letters*, **102**:143601, 2009.

[32] Anatoly A. Svidzinsky, Jun-Tao Chang, and Marlan O. Scully. Cooperative spontaneous emission of n atoms: Many-body eigenstates, the effect of virtual lamb shift processes, and analogy with radiation of n classical oscillators. *Physical Review A*, **81**:053821, 2010.

[33] Marlan O. Scully and Anatoly A. Svidzinsky. The effects of the N atom collective Lamb shift on single photon superradiance. *Physics Letters A*, **373**:1283–1286, 2009.

[34] Ya. A. Fofanov, A. S. Kuraptsev, I. M. Sokolov, and M. D. Havey. Dispersion of the dielectric permittivity of dense and cold atomic gases. *Physical Review A*, **84**:053811, 2011.

[35] S. Balik, R. Olave, C. I. Sukenik, M. D. Havey, V. M. Datsyuk, D. V. Kupriyanov, and I. M. Sokolov. Spectral dependence of diffuse light dynamics in ultracold atomic ^{85}Rb. *Journal of Modern Optics*, **53**:2495–2505, 2006.

[36] A. S. Kuraptsev and I. M. Sokolov. Spontaneous decay of an atom excited in a dense and disordered atomic ensemble: Quantum microscopic approach. *Physical Review A*, **90**:012511, 2014.

[37] Ph. W. Courteille, S. Bux, I. Lucioni, K. Lauber, T. Bienaimé, R. Kasier, and N. Piovella. Modification of radiation pressure due to cooperative scattering of light. *European Physical Journal D*, **58**:69–73, 2010.

[38] Ralf Röhlsberger, Kai Schlage, Balaram Sahoo, Sebastien Couet, and Rudolf Rüffer. Collective Lamb shift in single-photon superradiance. *Science*, **328**:1248–1251, 2010.

[39] G. Labeyrie, D. Delande, C. A. Müller, C. Miniatura, and R. Kaiser. Multiple scattering of light in a resonant medium. *Optics Communications*, **243**:157–164, 2004.

[40] K. Kemp, S. J. Roof, M. D. Havey, I. M. Sokolov, and D. V. Kupriyanov. Cooperatively enhanced light transmission in cold atomic matter. *ArXiv e-prints*, 2014.

[41] Salim Balik. *Light Scattering in Ultracold High Density 87Rb Vapor*. PhD thesis, Old Dominion University, 2008.

[42] J. Keaveney, A. Sargsyan, U. Krohn, I. G. Hughes, D. Sarkisyan, and C. S. Adams. Cooperative lamb shift in an atomic vapor layer of nanometer thickness. *Physical Review Letters*, **108**:173601, 2012.

[43] Tetsuya Ido, Thomas H. Loftus, Martin M. Boyd, Andrew D. Ludlow, Kevin W. Holman, and Jun Ye. Precision spectroscopy and density-dependent frequency shifts in ultracold sr. *Physical Review Letters*, **94**:153001, 2005.

[44] Z. Meir, O. Schwartz, E. Shahmoon, D. Oron, and R. Ozeri. Cooperative Lamb shift in a quantum emitter array. *ArXiv e-prints*, 2013.

[45] Juha Javanainen, Janne Ruostekoski, Yi Li, and Sung-Mi Yoo. Shifts of a resonance line in a dense atomic sample. *Physical Review Letters*, **112**:113603, 2014.

[46] M. Chalony, R. Pierrat, D. Delande, and D. Wilkowski. Coherent flash of light emitted by a cold atomic cloud. *Physical Review A*, **84**:011401, 2011.

[47] M. O. Araújo, I. Kresic, R. Kaiser, and W. Guerin. Superradiance in a large cloud of cold atoms in the linear-optics regime. *ArXiv e-prints*, 2016.

[48] P. W. Anderson. More is different. *Science*, **177**:393–396, 1972.

[49] L. Goehring, S. W. Morris, and Z. Lin. Experimental investigation of the scaling of columnar joints. *Physical Review E*, **74**(3):036115, 2006.

[50] Xiao-Liang Qi and Shou-Cheng Zhang. Topological insulators and superconductors. *Rev. Mod. Phys.*, **83**:1057–1110, 2011.

[51] Rodney Loudon. *The Quantum Theory of Light*. Oxford University Press, 3 edition, 2000.

[52] Harold J. Metcalf and Peter van der Straten. *Laser Cooling and Trapping*. Springer, 1999.

[53] Christopher J. Foot. *Atomic Physics*. Oxford University Press, 2005.

[54] David J. Griffiths. *Introduction to Electrodynamics*. Prentice Hall, 1999.

[55] John David Jackson. *Classical Electrodynamics*. Wiley, New York, NY, 3rd edition, 1999.

[56] Heidi Fearn, Daniel F. V. James, and Peter W. Milonni. Microscopic approach to reflection, transmission, and the ewaldoseen extinction theorem. *American Journal of Physics*, **64**(8):986–995, 1996.

[57] Julien Chabé, Mohamed-Taha Rouabah, Louis Bellando, Tom Bienaimé, Nicola Piovella, Romain Bachelard, and Robin Kaiser. Coherent and incoherent multiple scattering. *Physical Review A*, **89**:043833, 2014.

[58] M. Weissbluth. *Photon-Atom Interactions*. Academic Press, Inc., 1989.

[59] S. Chandrasekhar. Stochastic problems in physics and astronomy. *Revews of Modern Physics*, **15**:1–89, 1943.

[60] J. E. Sansonetti. Wavelengths, transition probabilities, and energy levels for the spectra of rubidium (RbI through RbXXXVII). *Journal of Physical and Chemical Reference Data*, **35**(1):301–421, 2006.

[61] Daniel Adam Steck. Rubidium 87 D Line Data. http://steck.us/alkalidata.

[62] Carl E. Wieman and Leo Hollberg. Using diode lasers for atomic physics. *Review of Scientific Instruments*, **62**(1):1, 1991.

[63] Steven Chu, L. Hollberg, J. E. Bjorkholm, Alex Cable, and A. Ashkin. Three-dimensional viscous confinement and cooling of atoms by resonance radiation pressure. *Physical Review Letters*, **55**:48–51, 1985.

[64] Paul D. Lett, Richard N. Watts, Christoph I. Westbrook, William D. Phillips, Phillip L. Gould, and Harold J. Metcalf. Observation of atoms laser cooled below the doppler limit. *Physical Review Letters*, **61**:169–172, 1988.

[65] J. Dalibard and C. Cohen-Tannoudji. Laser cooling below the doppler limit by polarization gradients: simple theoretical models. *Journal of the Optical Society of Americ a B*, **6**(11):2023–2045, 1989.

[66] W. J. Schwenger and J. M. Higbie. High-speed acousto-optic shutter with no optical frequency shift. *Review of Scientific Instruments*, **83**:083110, 2012.

[67] G. Ronald Hadley. Injection locking of diode lasers. *IEEE Journal of Quantum Electronics*, **QB-22**(3):419–426, 1986.

[68] S. J. M. Kuppens, K. L. Corwin, K. W. Miller, T. E. Chupp, and C. E. Wieman. Loading an optical dipole trap. *Physical Review A*, **62**:013406, 2000.

[69] M. Marinescu, H. R. Sadeghpour, and A. Dalgarno. Dynamic dipole polarizabilities of rubidium. *Physical Review A*, **49**:5103–5104, 1994.

[70] Rudolf Grimm, Matthias Weidemüller, and Yurri B. Ovchinnikov. Optical dipole traps for neutral atoms. *Advances in Atomic Molecular and Optical Physics*, **42**:95–170, 2000.

[71] C. S. Adams and E. Riis. Laser cooling and trapping of neutral atoms. *Progress in Quantum Electronics*, **21**(1):1–79, 1997.

[72] M. E. Gehm, K. M. O'Hara, T. A. Savard, and J. E. Thomas. Dynamics of noise-induced heating in atom traps. *Physical Review A*, **58**:3914–3921, 1998.

[73] Ying-Cheng Chen, Yean-An Liao, Long Hsu, and Ite A. Yu. Simple technique for directly and accurately measuring the number of atoms in a magneto-optical trap. *Physical Review A*, **64**:031401, 2001.

[74] Hung-Wen Cho, Yan-Cheng He, Thorsten Peters, Yi-Hsin Chen, Han-Chang Chen, Sheng-Chiun Lin, Yi-Chi Lee, and Ite A. Yu. Direct measurement of the atom number in a bose condensate. *Optics Express*, **15**(19):12114–12122, 2007.

[75] S. Balik, A. L. Win, and M. D. Havey. Imaging-based parametric resonance in an optical dipole-atom trap. *Physical Review A*, **80**:023404, 2009.

[76] Wolfram Research Inc. *Mathematica 10.3*, 2015.

[77] M Weel and A Kumarakrishnan. Laser-frequency stabilization using a lock-in amplifier. *Canadian Journal of Physics*, **80**(12):1449–1458, 2002.

APPENDIX A

RANDOM WALK CODE

The following Mathematica code [76] is a sample of the simulations used to comprehensively study diffusion of light and random walks. A large parameter space is studied; the number of atoms, sample radii, and probe detuning from resonance are all dynamically changed to observe their effects on the spatial distribution of the scattered light. For each simulation, a total of 10,000 atoms are used. In order to keep the same densities as those in the experiments, the length scales must be reduced by a factor of $(NNormal/10^5)^{1/3}$, where $NNormal$ is the number of atoms in the experimental atomic sample.

After the sample properties are defined, the atomic positions are set in a three-dimensional bi-Gaussian distribution. A single atom is placed outside of the sample and its position is a random uniform distribution to simulate the creation of a probe with constant intensity. The first atom is forced to decay in the same direction as the probe propagates in the experiment; the photon's decay vector is propagated, and if the distance between the vector and an atom is less than the cross-section, the photon will scatter from the atom. The decay direction from the second atom is selected from a uniform random distribution over all space, simulating a random walk. This process is continued until the photon's decay path no longer coincides with an atom. The final position of the photon is recorded once the photon's distance is $10z0(10)$ from the center of the sample, where $z0(10)$ is the largest radius of the sample. Another random sample is created, and the process is repeated for a total of 1000 samples. The parameter NA is set at the beginning of the code and determines the number of atoms in the experimental sample. Through nested Do loops, the sample size and detuning of the probe are incrementally changed. By changing NA, the code can be ran again for a different number of atoms.

```
NNormal = {78, 62, 45, 32,
    18}*10^4; (*Number of atoms in experimental sample*)
NAtoms = 10000; (*Number of atoms in simulation*)
DG = {0, .2, .4, .6, .8, 1.0, 1.2, 1.4, 1.6, 1.8,
  2.0} (*Detuning, in units of gamma*)
NA = 1;
```

```
r0 = {3.2834, 5.3090, 8.2942, 11.5156, 14.8199, 18.1619, 21.5241,
    24.8982, 28.2801,
    31.6672}/(NNormal[[NA]]/NAtoms)^(1/
      3); (*Radius of samples. The scaling factor reduces the radius \
in this simulation so that the density is the same in experiment and \
theory.*)
z0 = {245.7915, 245.8269, 245.9095, 246.0392, 246.2160, 246.4397,
    246.7103, 247.0275, 247.3912,
    247.8013}/(NNormal[[NA]]/NAtoms)^(1/
      3); (*Radius of samples along long axis. Make equal to r0 to \
have a spherical sample.*)

Do[jj = 1;
  \[Lambda] =
   N[.78*Sqrt[(NNormal[[NA]]/NAtoms)^(1/3)*(7/
          10)/(1 + (2*DG[[jjj]])^2)]/
      Pi]; (*This determines the physical size of the atom.
  It is the square root of the cross section divided by pi.*)
  CloseD = {};
  ResultsCoords = {};

  Do[SeedRandom[];
   (*The following creates a bi-Gaussian sample of atoms.
   Positions with x1, y1,
   and z1 are for the location of the first photon.*)
   Positionsx =
    RandomVariate[NormalDistribution[0, r0[[jj]]], NAtoms - 1];
   Positionsy =
    RandomVariate[NormalDistribution[0, r0[[jj]]], NAtoms - 1];
   Positionsz =
    RandomVariate[NormalDistribution[0, z0[[jj]]], NAtoms - 1];
   Positionsx1 =
    RandomVariate[
     UniformDistribution[{-2 r0[[10]] + 0.41074*z0[[10]],
```

```
      2 r0[[10]] + 0.41074*z0[[10]]}], 1];
   Positionsy1 =
    RandomVariate[
     UniformDistribution[{-2 r0[[10]] + 1.73205*z0[[10]],
       2 r0[[10]] + 1.73205*z0[[10]]}], 1];
   Positionsz1 = {z0[[10]]};
   Atom =
    Prepend[Table[{Positionsx[[i]], Positionsy[[i]],
       Positionsz[[i]]}, {i, 1, NAtoms - 1}], {Positionsx1[[1]],
      Positionsy1[[1]], Positionsz1[[1]]}];
   ClosestAtom := 1;
   Do[SeedRandom[];
    (*This is where the random walk happens.
    After the first photon decays in the direction of the laser beam,
    the rest are allowed to decay into 4pi.*)
    If[k == 1, Decayx = {-0.41074*z0[[10]]},
     Decayx =
      RandomVariate[UniformDistribution[{-r0[[jj]], r0[[jj]]}], 1]];
    If[k == 1, Decayy = {-1.73205*z0[[10]]},
     Decayy =
      RandomVariate[UniformDistribution[{-r0[[jj]], r0[[jj]]}], 1]];
    If[k == 1, Decayz = {-z0[[10]]},
     Decayz =
      RandomVariate[UniformDistribution[{-r0[[jj]], r0[[jj]]}], 1]];
    DecayHat =
     Flatten[{Decayx, Decayy, Decayz}]/Norm[{Decayx, Decayy, Decayz}];

    r1 = Atom[[ClosestAtom]];
    Decay =
     r1 + DecayHat; (*This creates a vector that begins at the \
location of the atom and points in the direction of the decay.*)
    (*PhotonD is the distance from the decay path to the center of \
each atom.*)
    PhotonD =
```

```
    Table[{i,
      If[i != ClosestAtom && Dot[Decay, Atom[[i]]] >= 0,
       Norm[
         Cross[Atom[[i]] - Atom[[ClosestAtom]], Atom[[i]] - Decay]]/
        Norm[Decay - Atom[[ClosestAtom]]], {}]}, {i, 1, NAtoms}];
   (*Now we choose those atoms that are within one cross section of \
the decay path.*)
   Do[If[PhotonD[[i, 2]] < \[Lambda],
     AppendTo[CloseD, PhotonD[[i]]], ## &[]], {i, 1,
     Length[PhotonD]}];
   If[Length[CloseD] == 0, Break[]]; (*If no atoms are close enough,
   we are done with this loop.*)
   (*We will choose the next atom to be that which is closest to the \
decaying atom and within the cross section of the decay path.*)
   ClosestAtom =
    First[SortBy[
      Table[{CloseD[[i, 1]],
        Norm[Atom[[1]] - Atom[[CloseD[[i, 1]]]]]}, {i, 1,
        Length[CloseD]}], {#[[2]] &}]][[1]];
   CloseD = {};
   Clear[Decayx, Decayy, Decayz]
   , {k, 1,
    100}]; (*The 100 here has been set to ensure we give multiply \
scattered photons enough events to escape the sample.
  If you increase the density of the sample,
  you may want to check the number of scatterers to make sure the \
photons are able to escape.*)

  t1pos =
   NSolve[Rationalize[
     Norm[r1]^2 + t^2 + 2 t*r1.DecayHat == 100 z0[[jj]]^2] && t > 0,
     t]; (*Propagate the last decay so that it is incident on a \
sphere of radius 10z0.
  This will give a position vector in cartesian coordinates.*)
```

```
    rfpos = Flatten[Evaluate[r1 + DecayHat*t /. t1pos]];
    AppendTo[ResultsCoords, rfpos];
    Clear[Positionsx, Positionsy, Positionsz, Positionsx1, Positionsy1,
      Positionsz1]
    , {j, 1, 1000}];  (*Determines the number of samples/
   iterations for the simulation.*)

   ResultsAngs =
    CoordinateTransform["Cartesian" -> "Spherical",
     ResultsCoords]; (*Transforms cartesian coordinates to spherical.*)
\


   Export["\\Detuning with V\\" <> ToString[DG[[jjj]]] <>
     "gammaCartesianResults" <>
     ToString[N[NAtoms/((2*Pi)^(3/2)*(r0[[jj]])^2*z0[[jj]])]] <>
     ".txt", ResultsCoords, "Table"];
   Export["\\Detuning with V\\" <> ToString[DG[[jjj]]] <>
     "gammaSphericalResults" <>
     ToString[N[NAtoms/((2*Pi)^(3/2)*(r0[[jj]])^2*z0[[jj]])]] <>
     ".txt", ResultsAngs, "Table"];
   , {jjj, 1, Length[DG]}];
```

APPENDIX B

LOCK-IN AMPLIFIERS

Lock-in amplifiers are used in electronic feedback loops to frequency stabilize the MOT and repumper ECDLs. As described below, by creating a derivative signal from a photodiode in the saturated absorption (SA) setup, the output of a lock-in amplifier can be used to lock the lasers to the desired frequency. For transitions that are fairly separated in frequency space, the voltage signal $V_{PD}(t)$ from the balanced homodyne photodiode detector for a single transition can be well described as a Lorentzian [77]

$$V_{PD}(t) = \frac{V_0}{\gamma^2 + \Delta(t)^2}, \tag{131}$$

with a peak voltage V_0, width γ, and the detuning $\Delta(t)$ of the laser from the transition of frequency ω_0 is $(\omega(t) - \omega_0)$.

The frequency of the laser $\omega(t)$ has a constant AC frequency modulation f_{mod} of 10 kHz applied through the current controller. Additionally, the length of the cavity is changed with the use of a triangle wave ramp applied to the piezo mounted behind the grating in the ECDL. Applying these two modulations to the laser that is initially lasing at a frequency ω_L, we have

$$\omega(t) = \omega_L + at + b\sin(f_{mod}t), \tag{132}$$

where a and b are the amplitudes of the ramp and AC modulation, respectively.

V_{PD} is applied to the input of the lock-in. The output of the function generator supplying the AC frequency modulation is also connected to the mixer input of the lock-in. The lock-in multiplies the two inputs and is capable of shifting the mixer input by a phase ϕ. The output of the lock-in V_{output} is then this signal integrated over a time τ:

$$V_{output}(T) = \int_T^{T+\tau} \frac{V_0 b\sin(f_{mod}t + \phi)dt}{\gamma^2 + (\omega_L + at + b\sin(f_{mod}t) - \omega_0)^2}. \tag{133}$$

With $\phi = 0$ and $\tau = 3$ ms, the output of the lock-in is a derivative of the SA signal. The lock box is used to reduce the amplitude a of the linear ramp until a single transition is being swept over. Then, a switch is used to turn off the ramp and allow the output of

the lock-in to control the piezo. As the laser frequency drifts, the lock-in signal provides feedback to keep the laser locked near the center of the desired transition.

VITA

Kasie Jean Kemp
Department of Physics
Old Dominion University
Norfolk, VA 23529

EDUCATION

Ph.D. in Physics, Old Dominion University, Norfolk, VA, August 2016
M.S. in Physics, Old Dominion University, Norfolk, VA, May 2012
B.S. in Physics, Bridgewater College, Bridgewater, VA, May 2010

PROFESSIONAL EXPERIENCE

Graduate teaching assistant, Old Dominion University, 2010-2016
Graduate research assistant, Old Dominion University, 2011-2016

PUBLICATIONS

- Stetson Roof, Kasie Kemp, Mark Havey, I.M. Sokolov, and D.V. Kupriyanov, *Microscopic lensing by a dense, cold atomic sample*, Optics Letters 40, 1137-1140 (2015).
- R.G. Olave, A.L. Win, Kasie Kemp, S.J. Roof, S. Balik, M.D. Havey, 'Optical manipulation of light scattering in cold atomic rubidium', *In* Svetlana A. Malinovskaya and Irinia Novikova (eds.), *From Atomic to Mesoscale: The Role of Quantum Coherence in Systems of Various Complexities*, World Scientific (2015).
- Kasie Kemp, S.J. Roof, M.D. Havey, *Cooperatively enhanced light transmission in cold atomic matter*, eprint arXiv:1410.2497 (2014).
- K.J. Kemp, S. Barker, J. Guthrie, B. Hagood, and M.D. Havey, *One dimensional light localization with classical scatterers; an advanced undergraduate laboratory experiment*, (To be published by American Journal of Physics).
- S.J. Roof, K.J. Kemp, I.M. Sokolov, and M.D. Havey, *Observation of single-photon superradiance and the cooperative Lamb shift in an extended sample of cold atoms*, (Submitted to Physical Review Letters).

Typeset using LaTeX.